12-17-2020 1:00 PM

Characterization Of The Mechanical Performance Of The AE44-2 And AE44-4 High Pressure Die Cast Mg-Rare Earth Alloys

Bolin Fu, *The University of Western Ontario*

Supervisor: Klassen, Robert J., *The University of Western Ontario*

A thesis submitted in partial fulfillment of the requirements for the Master of Engineering Science degree in Mechanical and Materials Engineering

Abstract

This thesis aims to study the local mechanical properties of high pressure die cast (HPDC) AE44-2 and AE44-4 alloys at 25˚C and 200˚C and their microstructures. The chemical composition of the precipitates and grain size, the effect of cooling rate on the grains, the relationship between the grain size and mechanical properties, and the creep resistance of these two HPDC alloys were studied and discussed.

In this thesis, the spherical micro-indentation, constant Berkovich indentation tests, and tensile tests were performed on the specimens at 25˚C and 200˚C to probe their stress-strain response and creep behavior. This study used a new analytical technique to deduce the stress-strain curves from the spherical indentation tests.

This thesis suggests that the mechanical properties of these two alloys have a complicated dependence on the grain size. Although, with different RE additions, these two alloys have a similar indentation creep resistance at 25˚C and 200˚C.

Keywords: Mg-Al-RE alloys, Spherical indentation testing, Elevated temperature mechanical properties.

Summary for Lay Audience

Magnesium (Mg) is one of the most abundant elements on earth. It was firstly discovered in 1808. Mg is located in the second group of the periodic table. It has a shiny silver-grey color. The density of Mg is only 1.728 g/cm^3 making it be one of the lightest structure metals in the world. Relative to its low density, the strength of Mg is high. The properties of Mg can also be optimized by different alloying elements for various applications. Because of its light-weighted properties, Mg is essential for industry, especially for the transportation industry. For example, by applying the Mg alloys in a car, the weight of the car would be reduced, and the performance and fuel economy of the car would be improved.

However, the melting temperature of Mg is low, so some Mg alloys cannot be used at high temperatures. One solution for this problem is adding a certain amount of rare-earth (RE) elements (usually 2~4 wt%). The Mg-Al-RE alloys can maintain a good strength at high temperatures (125˚C~175˚C). This study aims to evaluate the mechanical strength of two types of Mg-Al-RE alloys named AE44-2 and AE44-4, respectively. The main difference between these two alloys is the RE addition. For AE44-2, the RE addition is cheaper than that of AE44-4.

The result of this study shows that these two alloys have a similar behavior at room temperature and 200˚C. This result proves that the AE44-2 is an economical replacement of the expensive AE44-4 alloys. This study contributes to the application of light-weighted Mg alloy components in the automobile industry and promotes the development of fuel-efficient cars.

Acknowledgment

I gratefully acknowledge every group and person who provides me with generous help and support. Without their help, this thesis would never have completed. Firstly, Meridian Lightweight Technologies Inc. for providing the alloys used in this study, Canmet laboratories for casting the pyramidal specimens, and NSERC CRD for funding my research.

Secondly, I would like to thank Ariful Islam, who helps me with the spherical indentation tests. I also would like to thank Aria Khalili for analyzing the microstructure and hardness of the specimens and guiding me on how to polish the specimens. I hope to thank Aria Khalili and Himmatpal Matharoo for the measurement of grain size. Meanwhile, I would like to thank Giancarlo Jones for the constant load indentation creep tests. Meanwhile, I would like to thank Prof. M. Medraj for computing the phase diagrams of AE44-2 and AE44-4 alloys.

Thirdly, I would like to thank my family and friends, Zeng Nan, Zuoming Chen, who support me whenever I meet difficulties.

Finally, I would like to express my sincere gratitude to my supervisor, Prof. Robert Klassen, for his selfless help, support, and academic guidance during the past two years.

Table of Contents

List of Tables

List of Figures

List of Appendices

Chapter 1

1 Introduction

Magnesium and its alloys have very low density, less than 20%, and 70% steel and aluminum, respectively, and possess excellent specific strength. This property provides magnesium alloys with a wide range of application in weight-sensitive components, particularly in the automobile industry. Die-cast magnesium alloys, which are ideal materials for producing thin-wall structural components used in vehicles, are the essential branch of magnesium alloys. A good understanding of the relationship among the cooling rate during the die-cast process, microstructure, and die-cast magnesium's mechanical properties are essential.

Previous studies about die-cast magnesium alloys have found that although die-cast magnesium alloys have such good strength-to-weight properties, their creep resistance at temperatures above 100˚C is poor.[1][2][3] Several techniques have developed to improve the creep resistance of die-cast magnesium alloys. The AE (Mg-Al-RE) series of magnesium alloys is one of the creep-resistant cast alloys with superior creep resistance at temperatures up to about 200ºC. This alloy series contains 1~ 4 wt.% Rare Earth (RE) elements that react with the Al to form thermally stable Al-RE precipitates. Thus, AE alloys demonstrate improved mechanical properties at elevated temperature. Among AE series alloys, the AE44-4 (Mg-4Al-4RE) alloy containing Ce-rich mischmetal[1] demonstrates a good balance between the elevated temperature mechanical properties and die cast-ability. Therefore, AE44-4 attracts industry and academia's attention. However, the high cost of Ce-rich RE additions (Ce, La, Pr, and Nd) impedes its application in the market. A new variant of AE44 alloy named AE44-2 has been developed, which still contains about 4 wt%

[1] Mischmetal is a mixture of rare earths (Ce, La, Pr…).

Aluminum and 4wt% RE additions. However, the RE additions comprise only two, less expensive elements, namely Ce and La.

This study compares the local hardness, local stress-strain response, and creep resistance at both 25˚C and 200˚C to study the effects of different RE additions on the mechanical properties of AE44 alloys. Two forms of die-cast Mg - RE material are studied in this study. One is a high pressure die-cast (HPDC) panel provided by Meridian Lightweight Technologies Inc., while the other one is an HPDC pyramidal casting fabricated at Canmet laboratories (Hamilton, ON). The chemical composition and grain size are measured across the surface and core region of die-cast specimens. The measurement of chemical composition and microstructure was completed by Mr. Aria Khalili and Mr. Himmatpal Matharoo. The hardness of the panels was measured by Buehler Microhardness Machine. The microscale mechanical properties of both AE44-4 and AE44-2 HPDC specimens were studied using spherical micro-indentation tests at 25˚C and 200˚C. The load-depth data obtained from spherical micro-indentation tests were converted to stress-strain curves through a newly developed mathematical analysis. These results were compared with the stress-strain curves obtained from the uniaxial tensile test to evaluate the reliability of this analytical technique. The micro indentation tests were performed at different locations of pyramidal castings and panels to study the dependence of stress-strain response on the grain size. The constant-load Berkovich indentation creep tests were performed at 25˚C and 200˚C to compare the steady-state creep rate of every specimen. From these data, we can assess the suitability of using the less expensive AE44-2 alloy variant for load-bearing applications at temperature up to 200˚C.

Chapter 2

2 Literature Review

The purpose of this study is to probe the mechanical properties of AE44-4 and AE44-2 Mg-Al-RE alloys HPDC specimens by indentation technology and relate these properties with local microstructure. In this section, the necessary information on magnesium alloys and the relationship between microstructure and the mechanical properties of magnesium alloys will be introduced. Secondly, the development of the AE series of Mg-Al die-casting alloys will be presented with particular emphasis on the mechanical properties and microstructure of the AE42 and AE44 alloys. Thirdly, the method of spherical micro indentation and its application in assessing the local stress-strain response of material will be introduced and discussed. Finally, the creep behavior of magnesium alloys, especially AE alloys, will be addressed.

2.1 Magnesium and its properties.

Magnesium is one of the most abundant elements on earth. It was found by Humphrey Davy in 1808 and was isolated by Antoine Alexander Bussy in 1828.[4] Magnesium is the alkaline earth metal (group 2 metal) with shiny silver-grey color. The atomic number and atomic weight of magnesium are 12 and 24.32 g/mole, respectively. The density of pure magnesium is only 1.738 g/cm^3 at 20˚C, making it the lightest structural metal.[4] The crystal structure of magnesium is HCP (hexagonal close-packed), which has less active dislocation slip systems than face-centered cubic (FCC). This crystal structure has potentially harmful effects on the ductility of magnesium and leads to its directionally anisotropic mechanical response.

The mechanical properties of pure magnesium are relatively poor. For example, sand-cast Mg samples display a tensile strength of only about 90 MPa at 20˚C.[4] Adding alloying

elements can dramatically improve the mechanical properties and cast-ability of magnesium. The most common alloying elements are Aluminum, Zinc, and Manganese, Silicon, and, more recently, Rare Earth (RE) elements.[5][4][6]

2.2 Magnesium-Aluminum based alloys

Most commercial magnesium alloys are based on the Mg-Al alloy system and contain between about 1 and 10 wt% Al.[5] The beneficial effect of aluminum on the tensile strength, hardness, and cast-ability of magnesium was first reported in the early 1920s [6]. These benefits arise from the precipitation of the Mg_xAl_y intermetallic β phase, as indicated in the Mg-Al binary equilibrium phase diagram Fig.2.2.1.[7] Solid, HCP α-phase magnesium has a relatively high solubility for Al at elevated temperature. The maximum solubility of Al in α-Mg is about 11.8 at.% at 705K. (Fig.2.2.1) [7] The typical microstructure of an equilibrium cooled Mg- (1-10%) Al alloy is shown in Fig 2.2.2.a[8]. It should note that these alloys will form 100% HCP α-phase when they are annealed at 800-500K. Although the most die-cast Mg alloys contain only about 4% Al, their microstructure will have the $Mg_{17}Al_{12}$ β-phase, probably at α-phase grain boundaries, due to the high cooling rate during the die casting process. Fig. 2.2.2.b shows the nonequilibrium microstructure of a typical as -cast Mg-Al-Mn alloy [9]

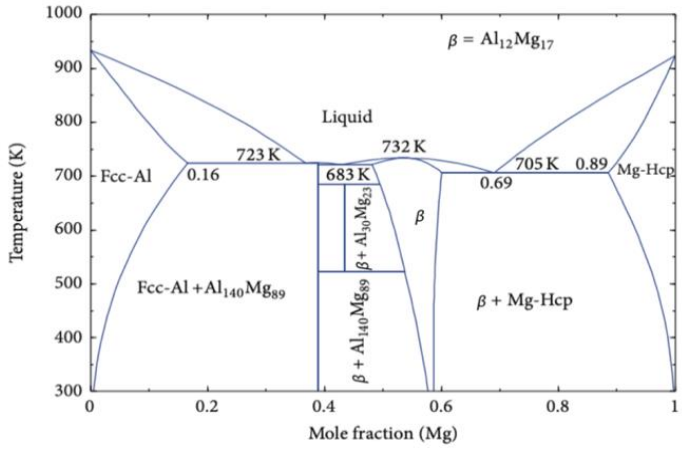

Figure 2.2.1 The Magnesium - Aluminum equilibrium binary phase diagram. (copy from [7])

(a)

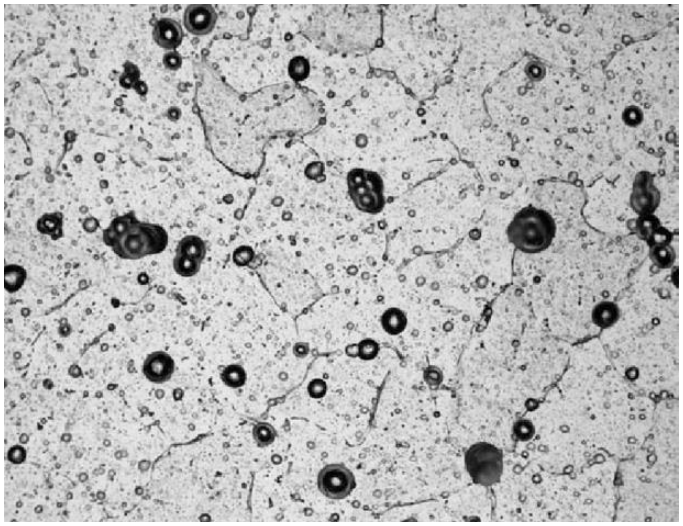

(b)

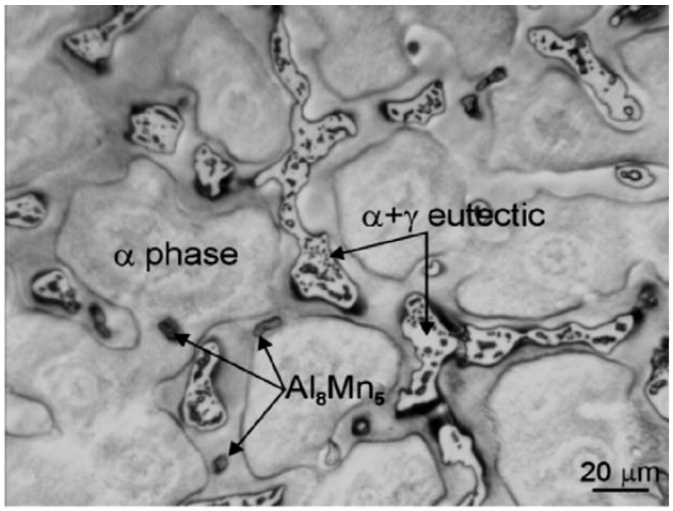

Figure 2.2.2 The microstructure of (a) an annealed Mg-Al alloy, (b) a typical as-cast Mg-Al-Mn alloy (nonequilibrium). (copy from [9])

As introduced previously, aluminum is the most common alloy addition of Mg alloys due to the beneficial effect on mechanical properties. The function of aluminum in magnesium alloys has been studied.[10] Firstly, The precipitation of β-phase particles effectively pins the α-phase grains and results in reduced α-phase grain size. The small grain size can strengthen the alloy by the Hall-Petch law (see Section 2.6 of this chapter).[10][11] Secondly, the dissolved Al in the α-Mg matrix introduces significant solid solution strengthening to the alloy.[11][12][13][14] Thirdly, the $Mg_{17}Al_{12}$ β-phase precipitates act as physical barriers to the motion of dislocations through the α-Mg matrix phase, increasing

its yield strength.[10]

During normal casting, particularly during high pressure die casting of Mg-Al alloys, the cooling rate is fast, and thus solidification conditions are far from "equilibrium." Under these conditions, the equilibrium Mg-Al binary phase diagram may not accurately predict the actual microstructure of the casting. Besides, commercial Mg-Al alloys invariably contain small amounts of other alloying elements such as Mn or Zn. These tertiary or quaternary alloy additions alter the shape of the phase regions in the phase diagram. As a result, it is often observed that the as-cast microstructure of commercial Mg-Al alloys have some degree of eutectic morphology present even though the alloy does not cross a eutectic-containing region in the equilibrium Mg-Al phase diagram. Also, the composition of the β-phase precipitates is often different than the expected $Mg_{17}Al_{12}$. Both these features can affect the mechanical strength and toughness of as-cast Mg-Al alloys. Figure 2.2.2 depicts the microstructure of a typical as-cast Mg-Al-Mn alloy. The properties of common commercial Mg-Al based alloys are listed in Table 2.2.1.

High-pressure die casting is a common method used for the manufacture of Mg-Al alloy components. During this process, the local cooling rate within the casting is quite variable and depends upon the location within the particular casting. The effect of cooling rate on the microstructure and mechanical properties of a series of Mg-Al castings has been studied by several researchers.[15][16] These findings are presented in more detail in section 2.6 of this chapter. The important point to note from these studies is that the local microstructure and mechanical properties of die-cast Mg alloys are highly variable. Thus, the subsequent chapters of this thesis focus on local properties of the AE44-4 and AE44-2 Mg-Al-RE alloys. We performed actual die-casting of the test material and then perform mechanical tests and microstructural characterizations of various regions throughout the castings to assess the degree of variability.

Table 2.2.1 Mechanical properties and die cast-ability of common magnesium alloys

Mechanical properties				Die cast-ability[17]	Reference
Yield Stress, MPa	**Ultimate Tensile Stress, MPa**	**Elongation to fracture,%**	**Creep strain %***	**0-5: (bad-good)**	
AZ series (Mg- Al- Zn): AZ91D				3.4	[6]
139 (RT)	204 (RT)	3.1 (RT)	0.08 (100˚C, 50MPa) 1.2 (150˚C, 50MPa)		
105 (150˚C)	169 (150˚C)	16 (150˚C)			
AM series (Mg-Al-Mn): AM60				2.5	[6][18][2]
115 (RT)	205(RT)	6 (RT)	0.97 (100˚C, 100MPa)		
87 (150˚C)	140 (150˚C)	24 (150˚C)	1.25 (150˚C, 50MPa)		
AE series (Mg-Al-RE): AE42				NA	[6][18][19]
139 (RT)	226 (RT)	11(RT)	0.41 (150˚C, 70MPa)		
118 (121˚C)	177 (121˚C)	23 (121˚C)			
106 (177˚C)	135 (177˚C)	28 (177˚C)			
AE44				2.8	[20][21]
135.1 (RT)	251.7 (RT)	8.2 (RT)	0.11 (175˚C, 60MPa) 0.13 (200˚C, 60MPa)		
110 (120˚C)	163 (120˚C)	35 (120˚C)	0.3 (250, 60MPa) 0.17 (175˚C, 75MPa)		

* Creep strain listed in Table 2.2.1 were obtained by virous papers, so the parameters of creep test vary.

2.3 Magnesium alloys for elevated temperature application.

Although the magnesium alloys have excellent specific strength, the poor performance of magnesium alloys at elevated temperature remains a barrier to further application in the automobile industry.[1][22] As shown in the Table2.2.1, The tensile strength of AZ91D at 150˚C is only 82% of that at room temperature. Besides, the creep resistance of Mg-Al alloys, especially the AZ91 and AM60B alloys, suffers a dramatic drop at the temperature higher than 125˚C [23] G. Foerster defined the temperature, at which the creep strain reaches 0.1% within 100 hours under a constant load (load=34.5 MPa), as the creep resistant temperature. G. Foerster compared the creep resistant temperature of different magnesium alloys (Table 2.3.1.[2]) and found that the AZ91 and AM60 have the poorest creep resistance. In contrast, the AE 42 (Mg-Al-RE) has the best creep resistance, almost double that of AZ91 and AM60. This drawback of magnesium-aluminum alloys is attributed to the poor thermostability of the $Mg_{17}Al_{12}$ β phase, which tends to degrade at a temperature above 125˚C. Additionally, diffusion of aluminum atoms, which are released from the β phase, also accelerates the creep of these alloys.[22][24][25][26]

Table 2.3.1 The creep resistant temperature of magnesium-aluminum alloys (creep strain=0.1%, time < 100h, load=34.5 MPa) [2]

Alloy	AZ91	AM60	AZ102	AS41	AS21	AE42
Creep resistance temperature ˚C	121	121	177	149	177	260

Some techniques have been developed to improve the elevated temperature mechanical properties of magnesium alloys. Firstly, introducing new alloying elements, which preferentially react with Al and forming a stable intermetallic phase.[27] The second method is forming coherent networking by a coherent phase to impede the grain boundary

sliding.[28][29] The third effective solution is removing aluminum element entirely from the magnesium alloys (i.e., the MEZ alloys [30][27]) to eliminate the negative effect associated with thermal decomposition of the β phase. The magnesium alloying system for elevated temperature application can be classified into three groups: the first group is the modified Mg-Al-based alloys such as the AE series (Mg-Al-RE), AX series (Mg-Al-Ca), and ACM series (Mg-Al-Ca-RE). The second group consists of Mg-Zn and Mg-Sn-based alloys, which are cheap but have little creep resistance improvement. The third group is the non-aluminum magnesium-rare earth alloys, which have a good creep resistance but relatively low die cast-ability and high cost. Among these three general groups of Mg alloys, the Mg-Al-RE alloys with good creep resistance and die-castability have seen the most industrial application. This class of alloy will be studied and discussed in this thesis.

2.4 Magnesium-aluminum-rare earth alloys

The AE series alloys have significantly enhanced creep resistance. The effects of RE on the microstructure and mechanical properties of magnesium alloys have been studied. The rare earth elements react with aluminum forming the $Al_{11}RE_3$ and Al_2RE intermetallic phases, which are more stable at elevated temperature than $Mg_{17}Al_{12}$. The $Al_{11}RE_3$ and Al_2RE intermetallic phases can impede grain boundary sliding.[27][22][31][32] Dow Chemical Company developed AE42 (Mg-4 Al-2 RE) alloy, which has a good balance between elevated temperature mechanical properties and die-castability.[33] Fig. 2.4.1 shows the microstructure of the as-cast AE 42 alloy. In this microstructure, the $Al_{11}RE_3$ are present as lamellar shaped precipitates, while the Al_2RE are present as fine globular shaped particles distributed throughout the α-Mg matrix phase.[34] Moreno et al. confirmed the good creep resistance of AE42 alloy and reported the creep strain of AE42 alloy remains under $\varepsilon = 0.005$ for 400 hours at 150 ˚C and 70 MPa.[35] Due to its good creep resistance, AE42 alloy has been recognized as the benchmark of creep resistance of magnesium alloys.[36] However, AE42 alloy loses its creep resistance when the temperature rises to 175˚C.[37][38] Powell et al. attribute this phenomenon to the decomposition reaction (shown below) of

$Al_{11}RE_3$ at the temperature above 150˚C.[33]

$$Al_{11}RE_3 \rightarrow 3\,Al_2RE + 5\,Al \quad [33]$$

This opinion is supported by Moreno et al., who reported that the morphology of AE42 alloy near the grain boundary changed after the creep test.[35] However, Zhu et al. propose a different opinion. they studied the thermostability of $Al_{11}RE_3$ and Al_2RE and found that the intermetallic phase ($Al_{11}RE_3$ and Al_2RE) did not change after aging at 200˚C for two weeks.[39] They concluded that the Al supersaturated α-Mg phase would release aluminum atoms at elevated temperature and result in the continuous precipitation of the $Mg_{17}Al_{12}$ phase, causing the degradation of creep resistance of the AE42 alloy.[39]

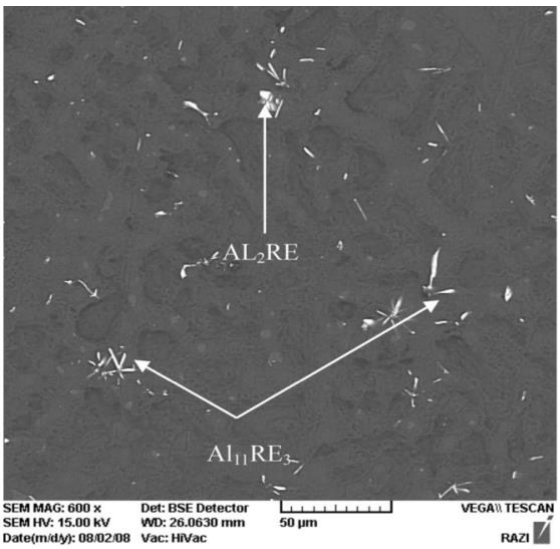

Figure 2.4.1 Microstructure of AE42. (copy from[34])

2.5 AE44 (Mg-4Al-4RE) alloy

In order to further improve the creep resistance of AE alloys, the AE44 alloy was developed.[40][20] Rzychoń et al. studied the microstructure of AE44 alloy and found that the weight fraction of both $Al_{11}RE_3$ and Al_2RE in AE44 alloy is 5.0 wt.%, almost twice of that in AE42 alloy (2.6 wt.%).[41] Rzychoń et al. also found that the creep strain of AE44 alloy is below ε = 0.0015 at 200˚C at 60 MPa for 120 hours. (Fig. 2.5.1)[41] Rzychoń et

al.'s work suggests that the increase of these intermetallic phases could account for the improved creep resistance of the AE44 alloy.[41] Zhu et al. found that the minimum creep rate of AE44 alloy is much lower than that of AE42 alloy at the 175˚C, under the same stress. (Fig.2.5.2)[42] By adding more RE elements, the content of aluminum in the α-Mg matrix decreases and results in less the $Mg_{17}Al_{12}$, which impairs the creep resistance, forming in the AE44 alloys.[42]

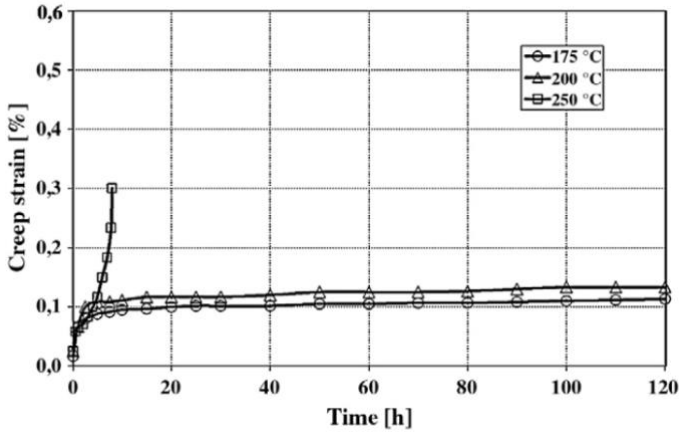

Figure 2.5.1 Creep curves of AE44 at different temperature (applied stress: 60 MPa)(copy from [41])

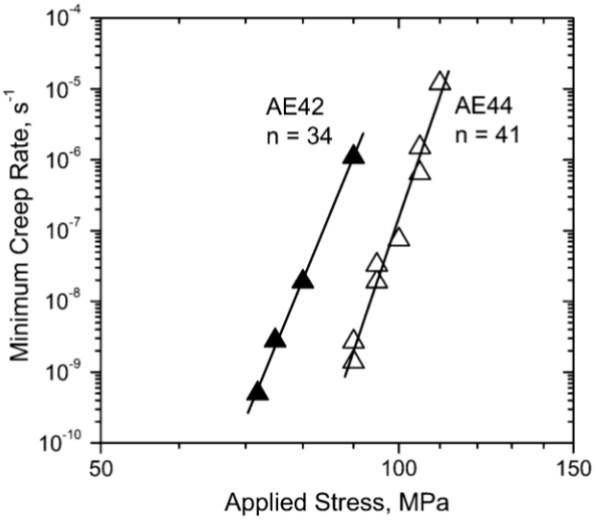

Figure 2.5.2 Comparison of minimum creep rate of AE44 and AE42 at 175˚C. (copy from [42])

However, the high cost of rare earth elements hinders the wider commercial application of the AE (Mg-Al-RE) alloys. The chemical composition of AE44 is listed in Table. 2.5.1. The rare earth elements are added in the form of Ce-rich mischmetal, which contains four rare earth elements: Cerium, Lanthanum, Neodymium, and Praseodymium.[40][43] Due to the development of permanent-magnets, a high volume of neodymium and praseodymium are consumed, causing a high cost of Ce-rich mischmetal.[31][44] In order to reduce the cost of Ce-rich mischmetal, a cheaper version, which contains only cerium and lanthanum, has been developed.[31][37] To distinguish them, the AE44 alloy, which contains the mixture of only cerium and lanthanum RE elements, is referred to here as AE44-2, while the traditional AE44 alloy contains four RE elements will be referred to as AE44-4. Zhang et al. compared the mechanical properties and creep resistance of AE44-4 alloy and AE44-2 alloys. They found that the AE44-2 alloy exhibits good creep resistance at temperature up to 200˚C, as shown in Fig. 2.5.3. They claimed that the creep resistance of the AE44-2 alloy is better than that of the AE44-4 alloy due to the better thermostability of the $Al_{11}(Ce, La)_3$ precipitates.[31][45][46] The effects of individual rare earth elements have been studied, and it is reported that the lanthanum has the best effect on improving the creep resistance of AE44 alloy and the cerium has the second-best effect. Some studies indicates that the lanthanum and cerium have the best effect on improving the creep resistance of AE44 alloy because the thermostability of the $Al_{11}La_3$ and $Al_{11}Ce_3$ are more stable at elevated temperature, have higher decomposition energy than $Al_{11}Pr_3$ and $Al_{11}Nd_3$. [47][48][49]

Table 2.5.1 Chemical composition (wt.%) of the AE44-4 and AE44-2 alloys

Alloy	Metallic additions			Rare-Earth additions			
	Al	Zn	Mn	Ce	La	Nd	Pr
AE44 (AE44-4)	3.69	0.03	0.37	2.24	1.32	0.64	0.24
AE44-2	4.03	0.02	0.27	2.51	1.56	0	0

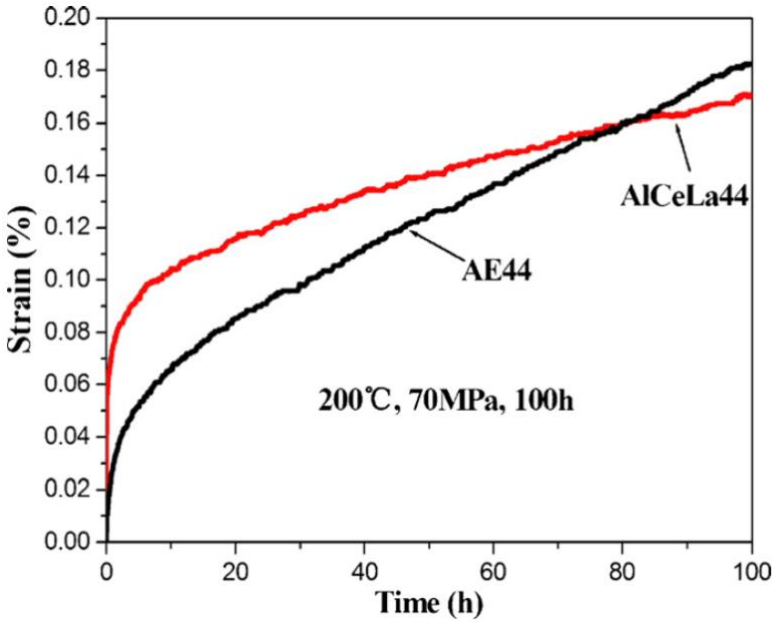

Figure 2.5.3 Tensile creep strain as a function of time of AE44-4 and AE44-2 alloys at 200˚C and 70MPa. (copy from [31])

2.6 Grain size effects

During the high pressure die casting process, the grain size varies by the thickness of the casting.[50] Therefore, it is essential to understand the effects of grain size on the mechanical porperties of polycrystalline magnesium alloys.

According to the Hall-Petch law (equation 2.6.1), the yield strength σ_y has a negative correlation with the square root of the grain size d [51][52]

$$\sigma_y = \sigma_0 + kd^{-\frac{1}{2}} \tag{2.6.1}$$

Where σ_0 and k are material dependent parameters determined by experimentation, for example, Jonathan Weiler has developed an equation to calculate the initial indentation stress at various regions of an AM60B casting following the Hall-Petch law, where $k = 274\ MPa \cdot \mu m^{1/2}$ and $\sigma_0 = 10\ MPa$.[15]

Bettles et al. studied the creep behavior of Mg-RE based alloys with different grain size

and found that the grain size has some effect on the creep rate. Usually, the steady-state creep rate has a negative correlation with the grain size. However, as shown in Fig. 2.6.1, the relationship between steady-state creep rate and grain size is close to a parabola.[53] In Fig. 2.6.1, the steady-state creep rate peaks when the grain size is around 235 μm. At larger grain size (d > 235 μm), the steady-state creep rate decreases as the grain size increases.[53] At the smaller grain size (< 235 μm), the steady-state creep rate decrease with the grain size.[53] Bettles et al. assumed that the grain size of the grain-refined specimens is too small to affect the total creep behavior observably, so the internal grain structure might control the creep mechanism.[53]

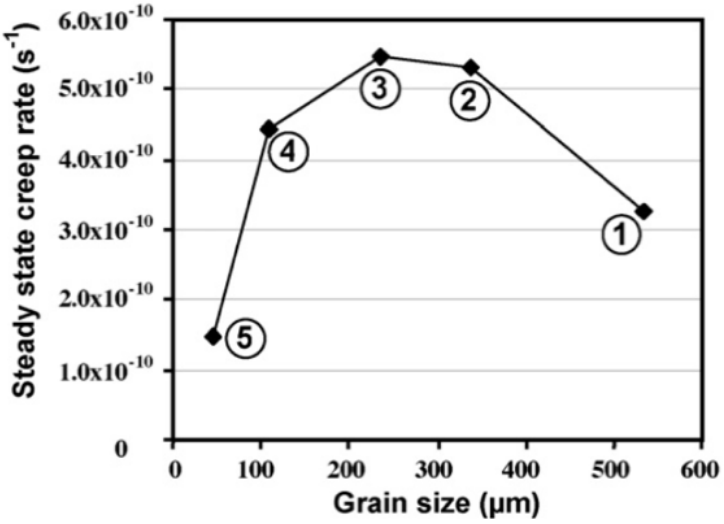

Figure 2.6.1 Effect of grain size on the steady-state creep rate of AE-SC1 alloys at 90 MPa and 450 K. (copy from [53])

2.7 Creep behavior of magnesium alloys

Generally, the creep deformation of the metals can be defined as three stages: primary creep, secondary creep, and tertiary creep.[54][55] The primary creep only occurs for a short time and does not show a steady creep rate. In the secondary creep stage, the creep rate becomes steady, and this "steady-state creep rate" is an important parameter for the creep behavior. In the last stage, the creep rate accelerates and the test specimen fails.[56] The steady-state

creep rate is used to study the creep resistance of different materials because this parameter is easy to measure and study during the whole creep process. Three parameters: time, stress, and temperature can greatly affect the creep rate. Researchers have developed the equations to reveal the relationship between steady-state creep rate and other parameters. Equation 2.7.1 is one of the most important equations to study the creep behavior of materials.

$$\dot{\varepsilon} = A\,\sigma^{n} \exp\left(-\frac{Q}{RT}\right) \tag{2.7.1}$$

Where A is a constant related to the material, which can be determined by experimentation. R is the gas constant, T is temperature, and σ is stress. Q is the activation energy of creep, n is the stress exponent, both Q and n can indicate which kind of creep mechanism is dominating the creep behavior of test specimens.[56][55] There are various creep mechanisms during the creep of material. (i) the dislocation slip, the creep caused by the motion of dislocations, is a creep mechanism occurring entire temperature range.[56] (ii) the dislocation climb, unlike dislocation slip, this mechanism involves the vacancy-atom exchange. This process is greatly affected by temperature because the dislocations need more energy to climb over the hindrance via vacancy diffusion.[56] (iii) grain boundary sliding. During this process, grains slide along the grain boundaries. This process depends on the grain size or grain boundary density in the material. Although an interesting parabolic relationship between grain size and steady-state creep rate was introduced in the previous section, it should note that usually, the steady-state creep rate increases as the grain size decreases because the reduction of grain size means the number of grain boundaries increases. As a result, there are more obstacles to stop the motion of dislocation.[56] (iv) diffusion-assisted creep, usually, materials are more likely to creep at elevated temperature, and therefore various diffusion models is thermally activated[56]

2.8 Spherical indentation

Spherical indentation is an ideal technique to study the mechanical properties, such as the

elastic modulus and hardness, of the materials. This technique involves pushing a sphere indenter into a material under a specific load or indent depth to obtain the load-depth response of the specimen. This technique was initially used by Brinell, who applied this technique to study the hardness of materials.[57] The spherical indentation can also be used to study the stress-strain response of materials. During the spherical indentation test, the indentation stress keeps changing as the indenter pushes into the material. This process is similar to the tensile or compression test, which can reveal stress-strain response during the deformation of the material. The increases of applied load (P) and the contact radius (a_c) go through three stages: first, the elastic deformation regime. In this stage, the deformation of the material is recoverable. This contact mechanism follows the Hertz solution.[58] Elastic-plastic transition is the second regime, in which the initial nucleation of plastic volume appears.[58] The third regime is fully plastic. During the fully plastic regime, the deformation of the material under the indenter is plastic.[58] Fig. 2.8.1.a illustrates the schematic of the spherical indentation test. Where h_t is the total indentation displacement, which is recorded by the indentation tester, h_e is the elastic depth, which shows how much the specimen can recover after complete unload, h_r shows the plastic deformation of the specimen after the complete unload, and h_c is the contact depth which is for the determination of contact radius. Fig. 2.8.1.b is a typical indentation load-depth curve. In the loading segment, the indenter pushes into the specimen, and the indentation strain and stress keep changing. This part of the curve reflects the stress-strain response of the specimens. The unloading segment can show the elastic properties to some extent. The slope of the initial part of the unloading curve is the contact stiffness, which will be discussed later in this section.

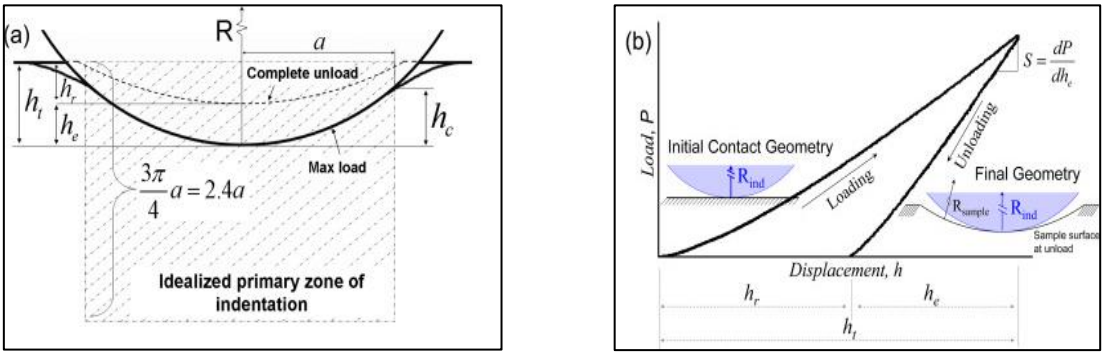

Figure 2.8.1 (a) Schematic of the spherical indentation test, (b) the load-depth curve of the indentation test.(copy from [59])

In this study, the spherical indentation tests were used to study the stress-strain response. According to the pervious researches, the determination of h_c (contact depth) is an important but difficult part of all the calculation models to deduce the stress-strain response. Many researchers have worked on it and proposed some methods to calculate the contact depth. Oliver-Pharr proposed an equation (equation 2.8.1) relating the h_c to the indentation load and the contact stiffness.[60]

$$h_c = h_t - \kappa P/S \tag{2.8.1}$$

Where the κ is a constant related to the geometry of indenter, which equals 0.75 for a sphere indenter.[60] It is easy to get the h_c by Oliver-Pharr's theory since all the parameters can be obtained in one spherical indentation test. However, this theory neglects the pileup and sink-in effect.

Hill et al. found that the h_c and h_t has an analytical relationship. The value of h_c/h equals an invariant c^2.[57]

$$c^2 = \frac{h_c}{h_t} \tag{2.8.2}$$

Hill et al. have studied the c^2 and found that the c^2 is a function of strain hardening exponent n. As equation 2.8.3 shown, this relationship is effective only for shallow

indentation (indentation diameter $\ll$ indenter diameter).[57]

$$c^2 = \frac{5(2-n)}{2(4+n)} \tag{2.8.3}$$

The contact radius a_c can be calculated using equation 2.8.4.

$$a_c = \sqrt{2h_cR - h_c^2} \tag{2.8.4}$$

Different techniques to convert the spherical indentation data to the stress-strain response of the material have been developed. In 1951 Tabor proposed that the parameters of spherical indentation have a relationship with the stress-strain response of materials. He has reported that the plastic stain ε_p equals $0.2a_c/R$ (equation 2.8.5), where a_c is the contact radius between tested specimen and sphere indenter, and R is the indenter radius.[61] Fig. 2.8.1.a demonstrates the schematic of the indentation test. This relationship has become the basis of other theories.

$$\varepsilon_p = 0.2\frac{a_c}{R} \tag{2.8.5}$$

Tabor also proposed an equation to calculate the indentation stress (equation 2.8.6).[61]

$$\sigma = \frac{P_m}{\psi} \tag{2.8.6}$$

Where the P_m is the mean pressure, which is defined as the applied load P divided by projected contact area A. The projected contact area A is only determined by the radius of the sphere indenter R and the contact depth h_c (equation 2.8.7). The ψ is a constraint factor. Equation 2.8.8 shows that the constraint factor has three different functions corresponding to the three deformation regimes.

$$A = \pi\,(2h_cR - h_c) \tag{2.8.7}$$

$$\psi = \begin{cases} C_1 & (\Phi \leq 1) \\ C_1 + C_2 \ln(\Phi) & (1 < \Phi \leq C_3) \\ \psi^c & (\Phi > C_3) \end{cases} \tag{2.8.8}$$

Where the Φ is a parameter which can be calculated by the equation 2.8.9.

$$\Phi = \frac{4Eh_c}{d\sigma_t} \tag{2.8.9}$$

Herbert et al.[62] proposed a model, which is based on the models from Hertz, Oliver and Pharr, and Tabor, to convert the spherical indentation to stress-strain response and compared the results with the stress-strain curves obtained from a uniaxial tensile test. They conducted the indentation tests using the continuous stiffness measurement (CSM) technique, which can output the contact stiffness (S) as a function of the indentation displacement.[62] The contact stiffness is then used to calculate the reduced modulus (E*) using equation 2.8.10.

$$E^* = \frac{\sqrt{\pi}}{2}\frac{S}{\sqrt{A}} \tag{2.8.10}$$

It should be noted that there are several models to determine contact depth: Matthews model, Hill model, and Oliver-Pharr model.[63][57][60]. In Herbert's work, the determination of contact depth h_c is based on the Oliver-Pharr model[62] (equation 2.8.1).

Based on Tabor's theory Herbert uses equation 2.8.11 and 2.8.12 to calculate the indentation stress and indentation strain, respectively.[62]

$$\sigma_{ind.} \approx P_m/3 \approx \sigma_t \tag{2.8.11}$$

$$\varepsilon_{ind.} \approx 0.2a_c/R \approx \varepsilon_p \tag{2.8.12}$$

Herbert et al. provide a straightforward technique to obtain the stress-strain response from a spherical indentation test. However, the Oliver-Pharr model does not consider the effect of plastic pileup, which results in the underestimate of a_c. The accuracy of equation 2.8.11

and 2.8.12 is only limited in the fully plastic regime.[62]

Xu et al.[64] proposed a reverse analytical approach, which is based on the iterative algorithm and can deduce the stress-strain response only using the spherical indentation parameters. Based on the previous work, Xu et al. proposed equation 2.8.13 to calculate the contact depth.[64]

$$h_c = h - \frac{1}{2\left(\frac{3P}{4E^*}\right)^{\frac{2}{3}}\left(\frac{1}{R}\right)^{\frac{1}{3}}} \tag{2.8.13}$$

$$\sigma_{eff} = \frac{1}{\alpha}\frac{P}{\pi a_c^2} \tag{2.8.14}$$

$$\varepsilon_{eff} = \frac{\beta}{\sqrt{1-\left(\frac{a_c}{R}\right)^2}}\frac{a_c}{R} \tag{2.8.15}$$

By optimizing the value of α and β, the σ_{eff} and ε_{eff} can be calculated using equation 2.8.14 and 2.8.15. Xu et al. introduced two constraint factors α and β, which are related to the properties of material. As equation 2.8.16 and 2.8.17 shown, the α is a function of the strain-hardening exponent n, while the β is a function of n and E/σ_y. The coefficients in the equation 2.8.16 and 2.8.17 are listed in table 2.8.1.[64]

$$\alpha = q_1 + q_2 n \tag{2.8.16}$$

$$\beta = \frac{p_1 + p_2\xi + p_3\eta + p_4\xi^2 + p_5\eta^2 + p_6\xi\eta}{1 + p_7\xi + p_8\eta} \tag{2.8.17}$$

Where $\xi = n, \eta = \ln(\frac{E}{\sigma_y})$

Table 2.8.1 Coefficients used in the equation 2.8.16 and 2.8.17.

q_1	q_2	p_1	p_2	p_3
4.30731	-2.14173	-0.10484	0.65039	0.03770
p_4	p_5	p_6	p_7	p_8
0.68093	-0.00348	-0.05567	3.36158	-0.16857

This analytical approach provides a new perspective to deduce the stress-strain curves from the spherical indentation test. However, the value of constraint factors α and β have a great influence on the final result.

This study proposes a new analytic approach to convert the load-depth data obtained from spherical indentation tests to stress-strain curves. This technique is based on the work of Hill et al and Matthew et al. to relate the indentation stress and indentation strain with strain hardening exponent.

Based on Tabor's theory the value of strain ε is related to the ratio of contact radius (a_c)and indenter radius(R), (equation 2.8.5). This equation is the basis of this study to calculate ε. The radius of the indenter can be easily measured, and the radius of the indenter used in this study is 110μm (R=110μm). However, the determination of the contact radius is much more complex. Due to the geometrical relation between contact radius (a_c), contact depth (h_c), and indenter radius (R), (equation 2.8.4) the determination of a_c can be regarded as the determination of (h_c). As introduced previously, different technologies have been developed to calculate the contact depth. In this study, the equation 2.8.2 & 2.8.3 proposed by Hill et al. is used to calculate h_c.

According to the equation 2.8.2, 2.8.3, 2.8.4, 2.8.5.

$$\varepsilon = \frac{0.2}{R}\sqrt{5\left(\frac{2-n}{4+n}\right)hR - \left(\frac{5(2-n)}{2(4+n)}h\right)^2} \tag{2.8.18}$$

Equation 2.8.18 correlated the strain ε with the strain hardening exponent (n)

This study correlates the stress with the n value either, by the equation 2.8.19 proposed by Matthew and Tirupataiah.[63][65]

$$\frac{P_m}{\sigma} = \frac{6}{2+n}\left(\frac{40}{9\pi}\right)^n \tag{2.8.19}$$

Where $P_m = \frac{P}{\pi a_c{}^2}$

As a result,

$$\sigma = \frac{P(2+n)}{6\pi\left(5\left(\frac{2-n}{4+n}\right)hR - \left(\frac{5(2-n)}{2(4+n)}h\right)^2\right)\left(\frac{40}{9\pi}\right)^n} \tag{2.8.20}$$

Equation 2.8.18 and 2.8.20 provide a new method to deduce the strain and stress from the load and depth. In these equations, only the strain hardening exponent cannot be obtained from the test. However, this problem can be solved by an iterative algorithm. Before the calculation, input a deaf n value, n = 0.3, and then calculate the strain and stress, a new strain hardening exponent can be deduced by fitting the log(stress)-log(strain) curve. Then repeat the procedure by using the new n value until the error of n value is less than 0.0001.

In this chapter, the background information of magnesium and common Mg-Al alloys and indentation techniques is introduced. Due to the excellent specific strength and good die-cast ability, the Mg-Al alloys are ideal lightweight materials for the automobile industry. In this thesis, the microstructure and mechanical properties of two kinds of AE44 alloys (AE44-2 and AE44-4) are studied to find the effect of different RE additions on the properties of AE44 alloys and the relationship between grain size and the mechanical properties. As introduced in this chapter the newly developed iterative algorithm is used to convert the indentation load-depth curves into stress-strain response. The specific experiment methods will be introduced in the next chapter.

Chapter 3

3 Experimental Methods

The overall objective of this thesis is to conduct an experimentation-based assessment of selected mechanical properties (hardness, stress-strain response, creep resistance) of die-cast AE44-4 and AE44-2 alloys at 25˚C and 200˚C such that we can compare the properties of the less expensive AE44-2 alloy relative to the more expensive, and more well established, AE44-4 alloy. The experimental methods that were used are described below. In this study, numerous specialized high pressure die castings were made of each of the two alloys, and data were collected on the temperature-time history of the metal during each casting process. The castings were then sectioned, and the microstructure, α-Mg grain size, at various regions of each casting was assessed and related to the specific cooling rate during casting. An extensive set of micro-spherical indentations were performed on various regions of the casting at 25˚C and 200˚C, and the resulting localized stress-strain response was determined as a function of grain size. Finally, constant-load of Berkovich micro-indentation creep tests were performed at 25˚C and 200˚C on various regions of the die-cast AE44-2 and AE44-4 alloys.

3.1 Test materials (AE44-2 and AE44-4)

The AE44-2 and AE44-4 material used in this study was supplied by Meridian Lightweight Technologies Inc., located in Strathroy, Ontario, Canada. The chemical composition of both alloys is listed in Table 2.5.1. As was mentioned earlier, the main difference between these two alloys is the composition of the rare earth mischmetal added to the alloys. The rare earth elements present in AE44-4 are Cerium, Lanthanum, Neodymium, and Praseodymium, while AE44-2 only contains Cerium, Lanthanum. The total content of the rare earth elements in both alloys is about 4wt.%.

Die-cast panels of AE44-2 and AE44-4, supplied by Meridian Lightweight Technologies, were analyzed by X-ray diffraction using a Rigaku diffractometer located in the Department of Earth Sciences at the University of Western Ontario. This analysis was performed to determine if the two alloys contained different crystalline phases within their microstructures. In the X-ray diffraction process, a monochromatic X-Ray beam was directed upon the samples, and the intensity of the reflected X-ray beam was measured as a function of scattering angle (2θ). Peaks in the reflected X-Ray intensity at particular values of 2θ indicates the presence of crystalline phases, of unique inter-planar spacing and crystal structure. The angular location of these "Bragg Peaks" was compared to the Bragg Peak locations corresponding to known Mg-Al-RE compounds.

3.2 Specimen preparation

In this study, two kinds of specimens were used: (i) die-cast pyramidal test specimens and (ii) high pressure die cast (HPDC) panels (Fig. 3.2.2). The pyramidal casting specimens were cast using an instrumented mini caster located at the Canmet Labs in Hamilton, Ontario. A dimensioned drawing of the steel mold assembly used to cast these specimens is shown in Fig. 3.2.1. This drawing indicates the location of ten thermocouples that were installed to record the temperature of the mold. The thermocouple 1 (TC 1) recorded the temperature of the molten alloy in the center of the mold. The AE44-2 and AE44-4 HPDC panels are supplied by Meridian and were used in several tests to compare the grain size and indentation hardness with the cast pyramids.

A total of seven pyramidal castings, three AE44-4, and four AE44-2, were performed in this study (Table 3.2.1). These castings were produced under different casting conditions. During the whole casting process, the casting pressure and temperature were recorded.

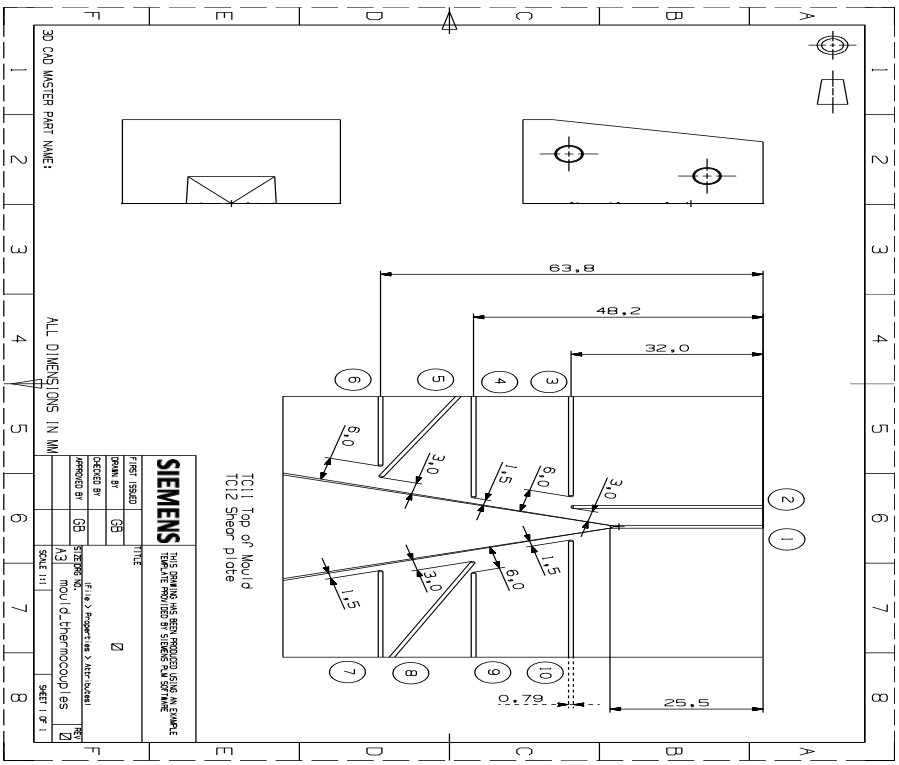

Figure 3.2.1 Dimensioned drawing of the steel pyramidal mold

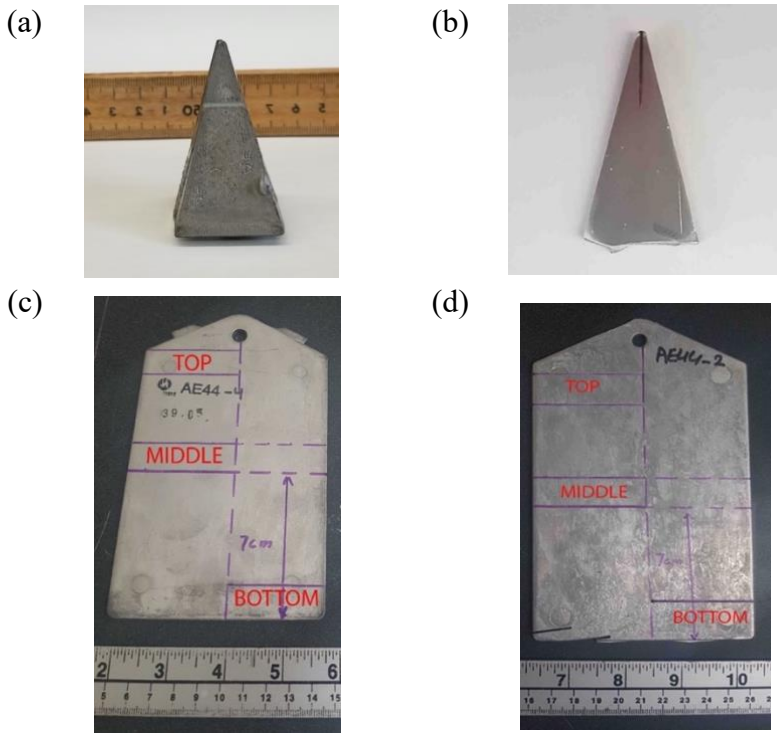

Figure 3.2.2 Photos of the test specimens used in this study: (a) as-cast pyramidal specimen, (b) the mid-plane cross-section of a pyramidal specimen, (c) the HDPC panels of AE44-4, and (d) the HDPC panels of AE44-2.

Figure 3.2.3 Illustration of a cast pyramidal specimen which has been sectioned to provide surfaces upon which micro-indentation tests were performed.

In order to perform spherical indentation tests on the pyramidal specimens, the pyramidal castings were cut into three pieces (Fig. 3.2.3). The middle plane, which has two flat surfaces and a triangle cross-section, was then ground with 400, 600, and 1200 grit SiC abrasive paper before being polished using a 0.05 μm colloidal silica polishing suspension.

The HPDC panels were cut into 1cm×1cm squares. Some squares were ground until the thickness was reduced by half to study the microstructure and mechanical properties at the core region. Because the surface and core regions have different grain sizes, the spherical micro-indentation tests were performed on the polished surface and the mid-thickness core regions of the AE44-2 and the AE44-4 HPDC panels.

Table 3.2.1 Information of the pyramidal specimens tested in this study

Casting Date (2018)	Alloy	Estimated TC 1 cooling rate, $\left.\frac{dT}{dt}\right\|_{T=620C}$ (°C/sec)	Effective solidification time $\Delta t_{T=620-500C}$ (sec.)	Measured average grain size at the TC 1 location.* (μm)	Comments
July 10	AE44-4	58	0.6 sec.	10.0	
July 25	AE44-2	49	2.1 sec.	10.7, 18.4	
Sep. 11	AE44-2				Test failed (leaked)
Sep. 13	AE44-2	121	0.9 sec.	5.0, 2.8	
Oct. 10	AE44-4				Test failed (recorded data error)
Oct. 23	AE44-4	125	1.1 sec.	6.6, 4.0	
Oct. 29	AE44-2	40	1.9 sec.	6.9, 7.9	

Table 3.2.2 Information of the Meridian HPDC test panels tested in this study

Alloy	Estimated cooling rate, $\left.\frac{dT}{dt}\right\|_{T=620C}$ (°C/sec)	Measured average grain size at the TC 1 location.* (μm)
AE44-4	150**	3 – 8 (4-14)***
AE44-2	150**	3 – 12 (9-12)***

* Adjoining numbers represent values obtained from independent measurement sets.

** Estimated.

*** Grain size measured on the surface (skin) of the test panels. Grain size measured at the mid-plane (core) is shown in brackets.

3.3 Grain size measurement

The grain size measurement was performed on the mid-plane of cut pyramidal specimens and as-cast panels because the cooling rate varies throughout the specimens resulting in the grain size varies with locations. In this study the grain size was measured from the tip region to the bottom region of the mid-plane of pyramidal specimens, and the skin- and core region of test panels. (Note the grain size was measured by Aira Khalili and Himmatpal Matharoo). The microstructure of the polished specimens were then imaged with Scanning Electron Microscopy (SEM). Assessment of the average α-Mg matrix phase grain size was determined from the obtained SEM images of the microstructure by using the Clemex image analysis software.[2]

3.4 Hardness tests

In this study, the hardness tests were performed on the panels at room temperature.[3] The Vickers hardness was measured using 100 g load and 10 second dwell period by Buechler Microhardness Machine. The hardness measurement was performed at the top-, middle-, and bottom regions, each region has three test location named edge, between, and center (as shown in Fig. 3.4.1)

[2] Note the grain size measurements were performed by Aria Khalili and Himmatpal Singh Matharoo.

[3] The Vickers hardness of AE44-2 and AE44-4 panels was measured by Aria Khalili.

(a) (b)

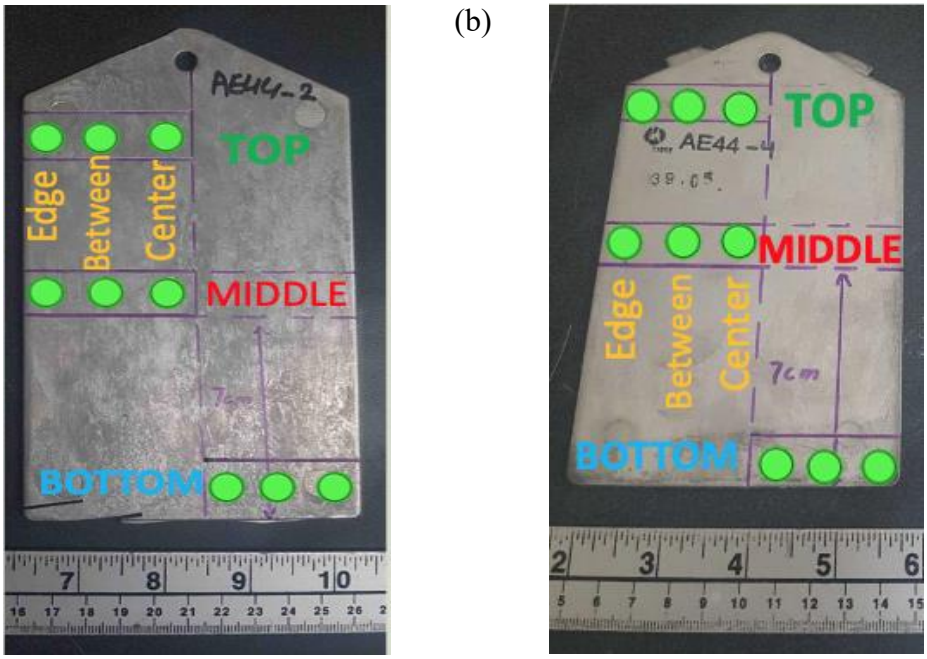

Figure 3.4.1 The locations where Vickers hardness measurements were performed on (a) AE44-2 panel, (b) AE44-4 panel.

3.5 Spherical micro-indentation tests

Spherical micro-indentation tests were performed on the polished specimens with a NanoTestTM micro-indentation hardness tester. (Fig.3.5.1.a) The micro-indentation tester is located in a temperature-controlled chamber situated on a pneumatic vibration isolation table. The micro-indentation tester has an optical microscope attached to it, which allows the user to accurately select the location on the sample where the indentation test is to be performed.

The micro-indentation test is performed by moving the indenter, which in the case of these tests is a diamond sphere of radius R = 110 μm (as shown in Fig.3.5.1.c) against the polished sample, and an indentation is made at a constant loading rate of 5 mN/s. The indentation load and depth are continuously recorded during the indentation process.

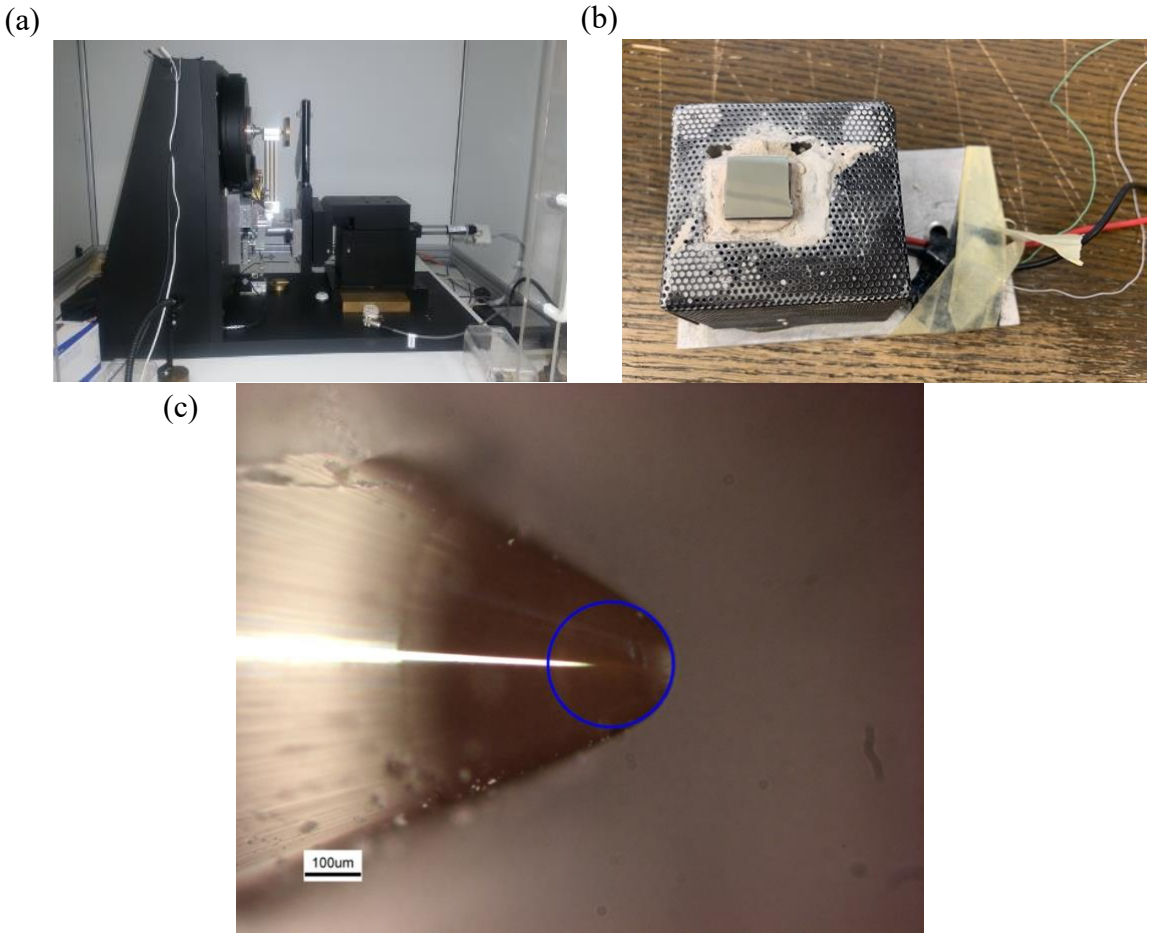

Figure 3.5.1 (a) NanoTest^{TM} micro-indentation hardness tester, (b) the specimen mounted on the heater, (c) the shape and radius of spherical indenter used in this study.

In this study, indentation tests were performed in the single- and multiple load-unload formats shown in Fig. 3.5.2. These tests were conducted at room temperature (25˚C) and 200˚C. For the elevated temperature test, the temperature of the indenter was controlled by an electrical resistance heater attached directly to the indenter, while another heater was attached beneath the specimens (Fig.3.5.1.b). Both heaters were controlled to 200˚C, thus maintained a constant temperature in the indenter-sample area of contact. The temperature of the indenter and specimen was monitored by two thermocouples respectively. The temperature of both specimen and indenter fluctuated between 199.8 and 200.1 ˚C. The indenter and specimen were heated to 200˚C then kept this temperature for at least 1 hour

before the indentation test to ensure the testing environment was stable. For a single load-unload test, the maximum load were set as 385 mN. A typical single load-depth curve is shown in Fig. 3.5.2.a. The blue curve is the loading part, from which the stress-strain response can be deduced. While the green curve is the unloading part. The slope of the initial part of the unloading curve, shown as the red line in Fig. 3.5.2.a, demonstrates the contact stiffness (S) of the material. The multiple load-unload curves are shown in Fig.3.5.2.b. the number of load-unloading cycles is 7, and the maximum load is set as 385 mN. Spherical micro-indentation tests, described above, were performed at the tip-, TC 1-, and bottom-regions of pyramidal specimens and the skin and core regions of the test HPDC panels. The multiple load-unload tests were performed at various regions with different grain sizes. The specific information of spherical indentations performed on every single specimen is listed in Table 3.4.1.

The results of all spherical micro-indentation tests were converted to stress-strain response via the analytic approach proposed in this paper. The load and depth data of the loading segment were converted to indentation stress and strain, respectively, through equation 2.8.18 and 2.8.20. The deduced stress-strain curves were compared with tensile stress-strain curves, and the strain hardening exponent, deduced from the analytic approach, of each test was related to grain size.

(a) (b)

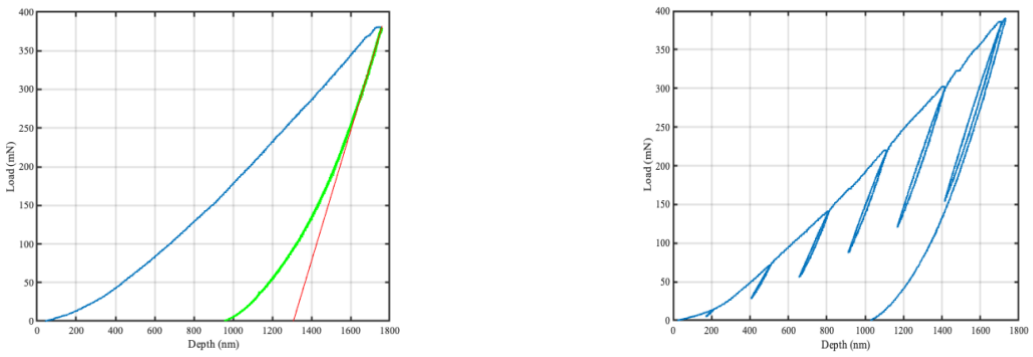

Figure 3.5.2 Typical Load-Depth curve of (a) single load-unload spherical micro-indentation test, (b) multiple load-unload spherical micro- indentation test.

Table 3.5.1 List of locations where spherical micro-indentations were performed on the various test samples. The number of tests performed at each location is also listed

Casting Date (2018)	Alloy	Location of the indentations within the sample	Indentation tests performed at 25ºC.	Indentation tests performed at 200ºC	Comments
July 10	AE44-4	tip		2 tests	single load-unload indentation tests
		TC 1		4 tests	
		bottom			
July 25	AE44-2	tip	2 tests		single load-unload indentation tests plus 17 multiple load-unload indentation tests (7 tests at 25˚C, 10 tests at 200˚C
		TC 1	6 tests		
		bottom	3 tests		
Sep. 13	AE44-2	tip	3 tests		single load-unload indentation tests
		TC 1	3 tests		
		bottom	4 tests		
Oct. 23	AE44-4	tip	5 tests	6 tests	single load-unload indentation tests plus 8 multiple load-unload indentation tests (2 tests at 25˚C, 6 tests at 200˚C)
		TC 1	4 tests	5 tests	
		bottom	4 tests	3 tests	
Oct. 29	AE44-2	tip	4 tests	4 tests	single load-unload indentation tests
		TC 1	3 tests	3 tests	
		bottom	4 tests	6 tests	
HPDC AE44-2 panel		skin	8 tests	1 test	multiple load-unload indentation tests
		core	7 tests	2 tests	
HPDC AE44-4 panel		skin	5 tests		multiple load-unload indentation tests
		core	6 tests		

3.6 Tensile test

The flat-coupon tensile test specimens, cut from HDPC AE44-2 and AE44-4 panels, were supplied by Meridian (Fig.3.6.1). Tensile tests were performed on these specimens at 25˚C and 200˚C. The 25˚C tensile tests were performed on an ATM tensile test machine (Adelaide Testing Machines Inc.) at the UWO. The tests were performed at constant crosshead speed of 0.25 mm/s. Two AE44-2 and three AE44-4 specimens were tested. The 200˚C tensile tests were performed on an MTS tensile testing machine located in the Centre for Advanced Composites located at the Fraunhofer Project Center in London, Ontario. This testing machine is equipped with an elevated temperature environmental chamber (Fig. 3.6.2). The tensile specimens were kept in the furnace at least 30 minutes before testing to ensure they reached the required 200˚C testing temperature. The tensile tests were performed at a constant crosshead speed of 0.08 mm/s. Three AE44-2 and two AE44-4 specimens were tested at 200˚C. The stress-strain curves obtained from these tensile tests were compared with those deduced from the spherical indentation tests.

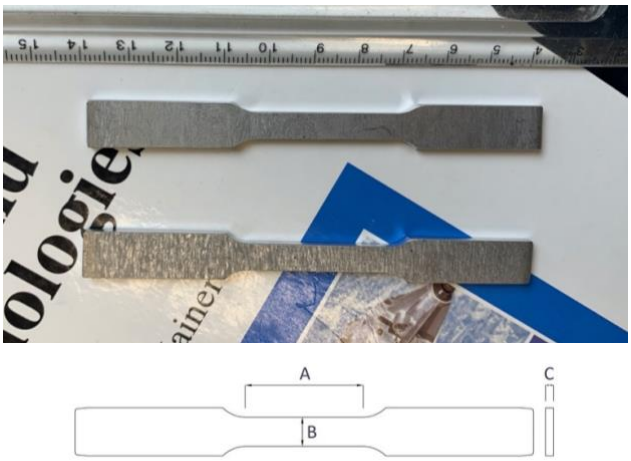

Figure 3.6.1 The photo and schematic of the tensile test specimens, where A = 40mm and the cross area (C*B) = 17.405 mm^2.

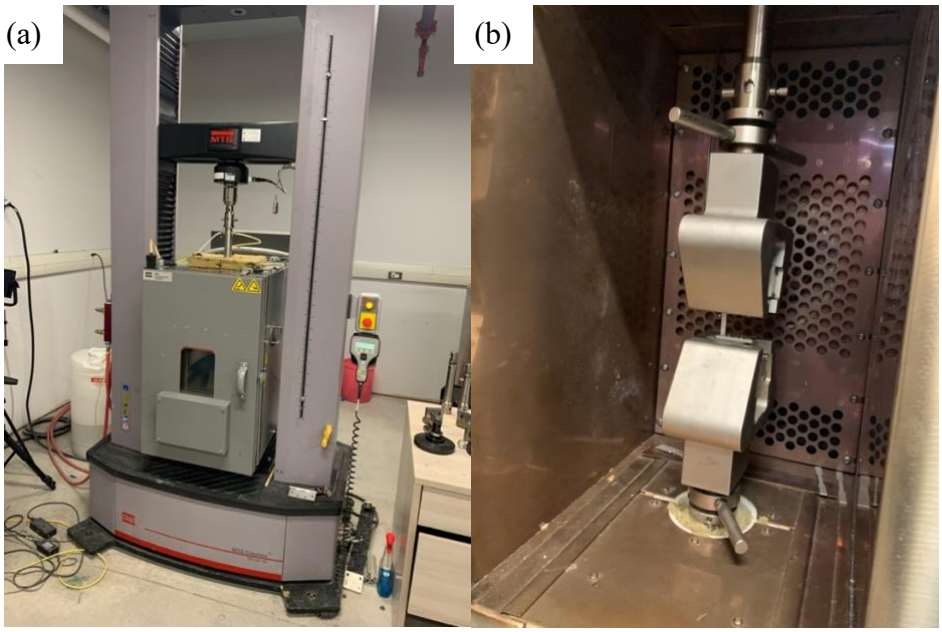

Figure 3.6.2 (a) MTS tensile test machine with furnace (b) the specimens were heated in the furnace.

In this study, the strain of the tensile tests was calculated based on the motion of the cross-heads. As shown in equation 3.6.1, where $l_{cross-head}$ is the distance between the cross-heads of the tensile test machine, and l_0 is the gauge length of the specimen.

$$\varepsilon_{tensile} = \frac{l_{cross-head} - l_0}{l_0} \tag{3.6.1}$$

It should be noted that this method for measuring strain is incorrect because the tensile test machine does not measure the distance between the cross-heads directly. As a result, the strain obtained via this method is larger than the true strain of the specimen.

3.7 Constant load creep tests.

The importance of creep resistance of magnesium alloys has been introduced in chapter 2. In order to study the creep resistance of AE44-2 and AE44-4 alloys, the constant load indentation tests were performed on July 25 (AE44-2) and Oct 23 (AE44-4) specimens. As introduced in specimen preparation (section 3.2), the pyramidal specimens were cut into

three pieces, and the middle panels were used for spherical indentation teats, while the rest part of July 25 and Oct 23 specimens were cut and polished for the constant load creep tests. Fig. 3.7.1 shows the cut specimens before polishing. Alemnis indentation tester (shown in Fig. 3.7.2) equipped with a three-sided pyramidal (Berkovich) indenter was used for the constant load creep test.[4] The creep tests were performed at 25˚C and 200˚C. The maximum constant load is set as 20mN and hold for 3600 seconds. The indenter was then retracted partially to 10% of the max load (2mN) and hold for 1 hour for thermal drift calculation.

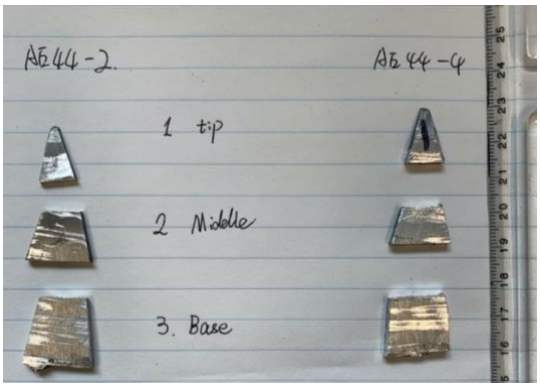

Figure 3.7.1 The specimens prepared for creep tests the left three pieces are July 25, right three pieces are Oct 23.

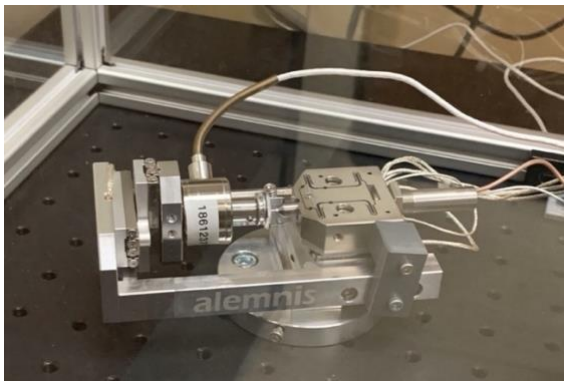

Figure 3.7.2 The picture of Alemnis indentation tester

[4] The creep tests were performed with help from Giancarlo Jones.

Chapter 3 illustrates the main study methods used in this paper. The alloys studied were processed into two types, the die cast pyramidal castings, and HPDC panels. These two specimens were cut into an appropriate shape and polished for the microstructure and mechanical properties study. This chapter introduced the methods used for grain size, hardness measurement, and the spherical micro-indentation tests and constant load creep test to study the mechanical properties of AE44-2 and AE44-4 alloys. The results will be shown in the next chapter, and further discussion about these results will be presented in chapter 5.

Chapter 4

4 Results

This thesis aims to study the mechanical properties of AE44-2 and AE44-4 alloys and the effects of cooling rate, grain size, and the temperature on their mechanical peripeties. Chapter 4 presents the results of (i) XRD analysis of AE44-2 and AE44-4, (ii) the variation of temperature and pressure at TC 1 location for each pyramidal casting, and the cooling rate of TC 1, TC2, TC 10 locations, (iii) the measured grain size of each casting at different regions, (iv) Hardness of HPDC panels at different regions, (v) the load-depth graphs for the spherical indentations made at each location within the samples, (vi) tensile tests performed at 25˚C and 200˚C, and (vii) the displacement-time graphs obtained by the constant-load indentation creep tests performed, with the Alemnis indenter, at 25˚C and 200˚C.

4.1 Microstructural analysis of the pyramidal castings and the panels

As mentioned in previous chapters, the main difference between these two alloys used in this study is the chemical composition. Table 4.1.1 lists the chemical composition of the AE44-2 and AE44-4 alloys. The typical microstructure of the AE44-4 and AE44-2 specimens used in this study is shown in Fig. 4.1.1. Three different phases can be observed from the SEM image: dark grey phase, white phase, and light grey phase. A further study, using the back-scattered X-Ray diffraction (XRD) analysis, indicates that the AE44-2 panel contained La_3Al_{11}, $LaAl_4$, and $CeAl_4$ precipitates while the AE44-4 panel contained $NdAl_2$, Al_2Pr, CeMnAl, and $Pr_{0.6}NdAl_2$ precipitates (Fig. 4.1.2). These precipitates are consistent with the fact that the AE44-2 alloy contained only La and Ce rare earth additions while the AE 44-4 alloy contained Nd, Pr, Ce, and La additions. Neither alloy contained diffraction peaks characteristic of $Mg_{17}Al_{12}$ β-phase precipitates.

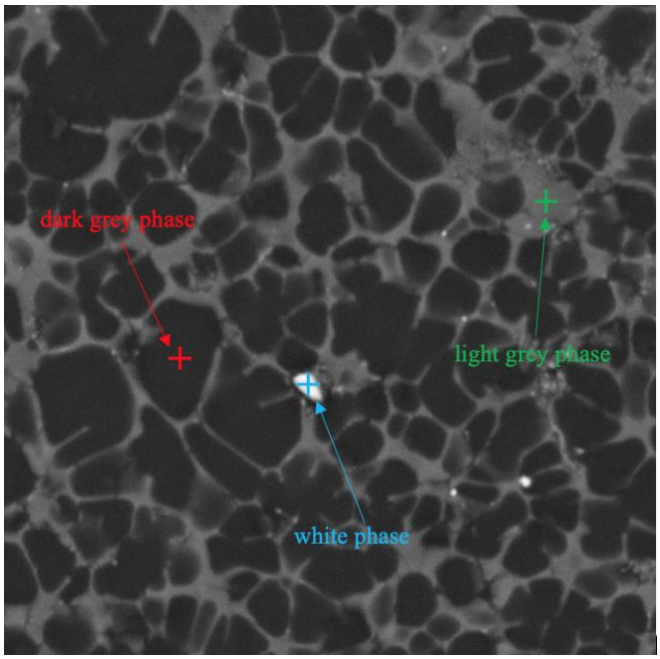

Figure 4.1.1 SEM picture of a specimen where three different phases can be observed.

Table 4.1.1 Alloy composition (wt%) of the AE44-4 and AE44-2 alloys.

Alloy	Metallic additions			Rare-Earth additions			
	Al	Zn	Mn	Ce	La	Nd	Pr
AE44-4	3.69	0.03	0.37	2.24	1.32	0.64	0.24
AE44-2	4.03	0.02	0.27	2.51	1.56	0	0

The complex chemical composition of the AE44-2 and AE44-4 alloys means that their microstructural evolution during die-casting can in no way is inferred from the standard Mg-Al binary equilibrium phase diagram (Fig. 2.2.1). While complete phase diagrams do not exist for the AE44 alloys, computed phase diagrams for the AE44-2 and AE44-4 alloys were obtained with the assistance of Prof. M. Medraj (Concordia U.). (attached in appendices).

(a)

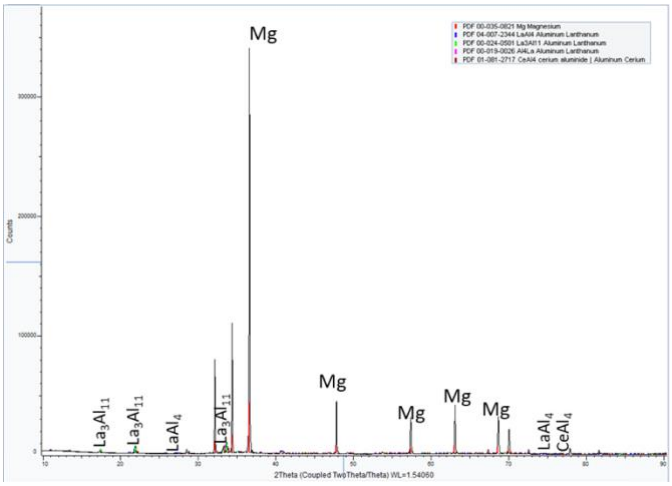

(b)

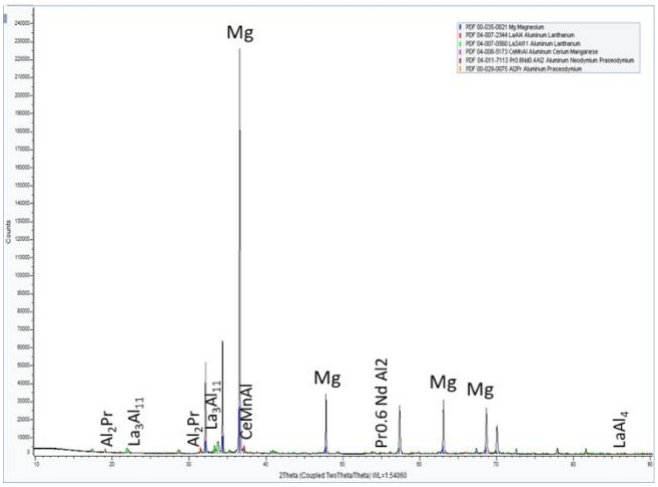

Figure 4.1.2 Reflected X-Ray intensity versus scattering angle, 2q, for (a) the AE44-2 sample, and (b) the AE44-4 sample.

4.2 The solidification process of pyramidal castings

The pyramidal castings used in this study consist of three AE44-4 castings and two AE44-2 castings. Detailed information has been introduced in the previous chapter (Table. 3.2.1). As mentioned above, the change of temperature and the cast pressure was monitored to study the effect of the casting parameters on the microstructure of castings. The cooling rate can influence the grain size and, therefore, affect the mechanical properties of the specimens. It is essential to understand the relationship between the cooling rate and grain size for optimizing the process parameters during the high pressure die casting to get the

desired mechanical properties. There are ten thermocouples in the pyramidal mold, but only one thermocouple (thermocouple 1) recodes the temperature of molten metal during the casting process. The results are shown below.

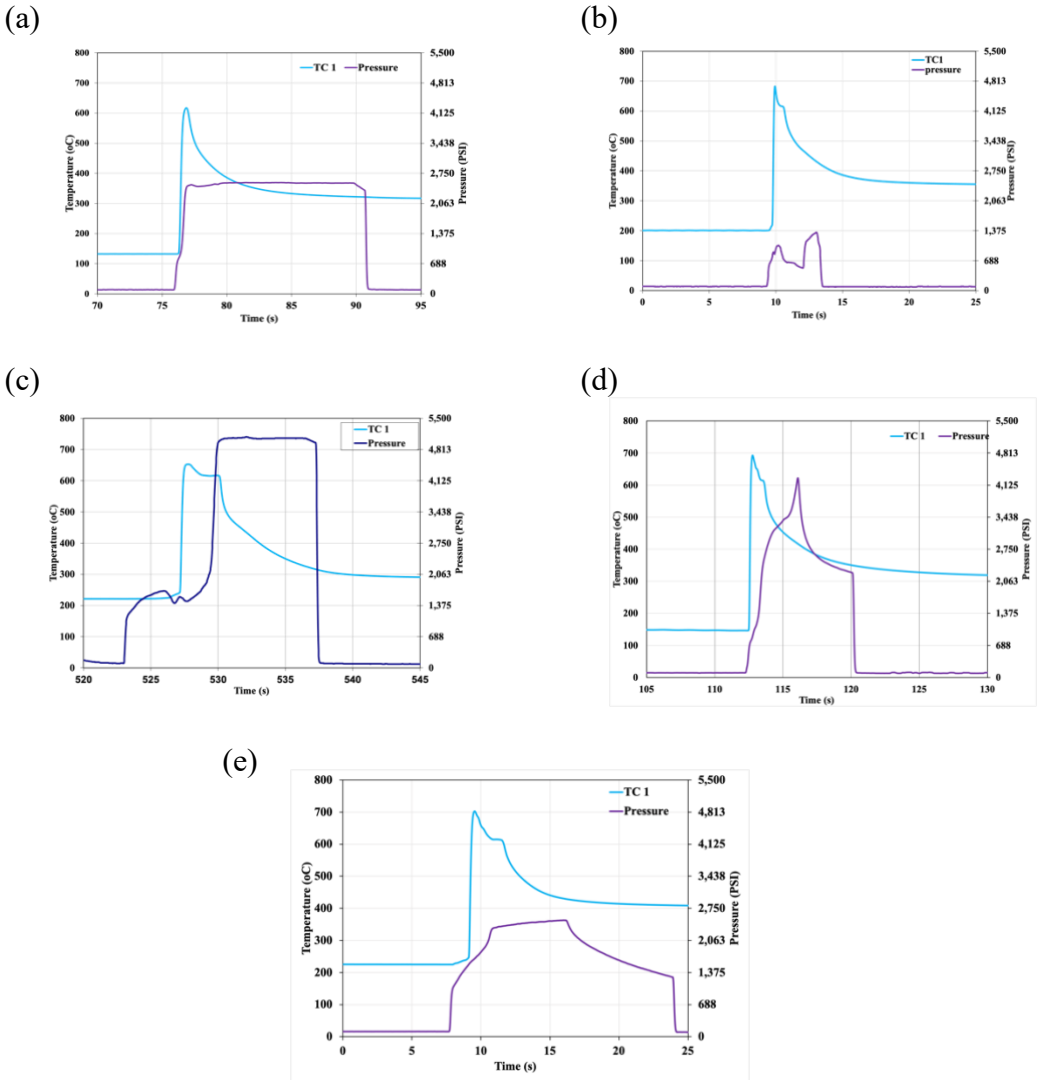

Figure 4.2.1 The temperature and pressure versus time of (a) July 10 casting, (b) Oct. 23 casting, (c) Oct. 29 casting, (d) Sep. 13 casting, (e) July 25 casting.

The cooling rate of the castings is essential for estimating the microstructure and mechanical properties. Since the temperature of every pyramidal casting has been recorded as a function of time, the instantaneous cooling rate ($r_{cooling}$) can be calculated via equation 4.2.1.

$$r_{cooling} = \frac{dT}{dt} \tag{4.2.1}$$

Additionally, the location of TC 2 and TC 10 (as shown in Fig. 3.2.1) is relatively near castings, so the cooling rate at these two locations are also calculated. Fig. 4.2.2 shows how the temperature and cooling rate changes with time. The temperature recorded by TC 2 and TC 10 is far less than that of TC 1. This could be attributed to the location of thermocouples. As shown in Fig. 3.2.1, although the TC 2 and TC 10 near the casting, they still record the temperature of the mold rather than the temperature of molten alloys.

Similarly, the cooling rate of TC 2 and TC 10 is much smaller than that of TC 1 location. Another fact is that the cooling rate of TC 1 location varies with castings. The highest instantaneous cooling rate has been seen in Oct 29 casting with 433˚C/s. The lowest instantaneous cooling rate is 181˚C/s of July 25 casting. For July 10-, Oct 23-, and Sep 13-casting, the cooling rate is 267.50˚C/s, 378.50˚C/s, and 371˚C/s, respectively.

(a)

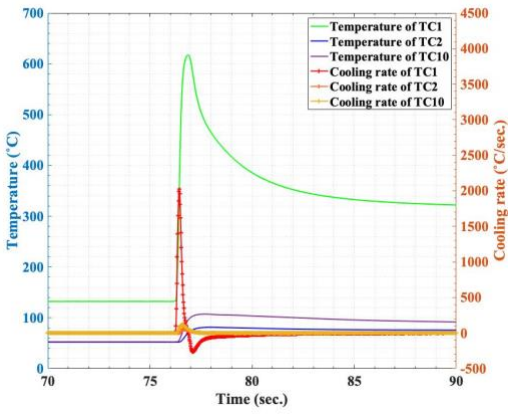

(b)

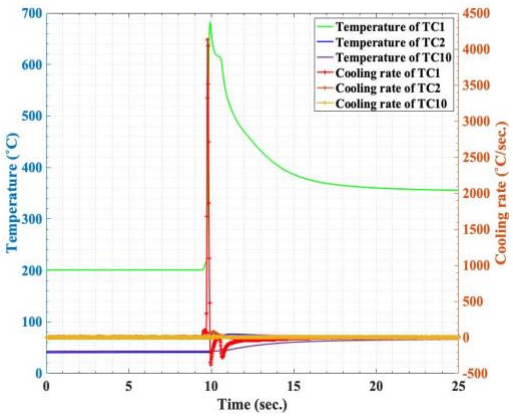

(c)

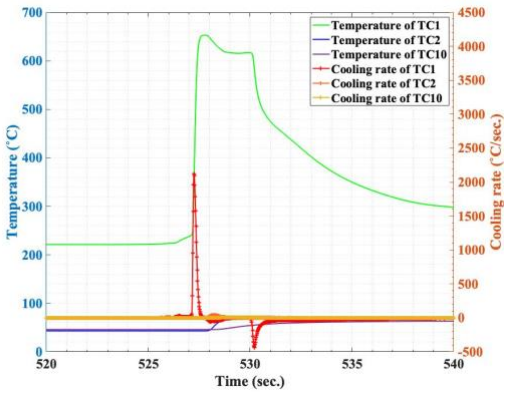

(d)

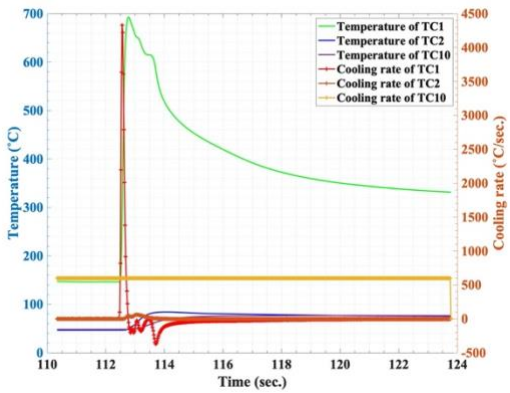

(e)

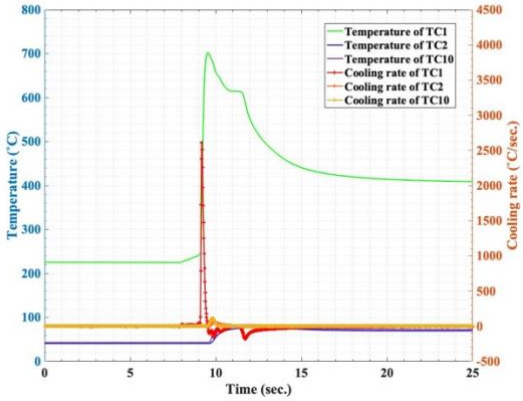

Figure 4.2.2 The cooling rate and temperature of TC 1, TC2, TC 10 locations of (a) July 10 casting, (b) Oct. 23 casting, (c) Oct. 29 casting, (d) Sep. 13 casting, (e) July 25 casting.

While the instantaneous cooling rate only reflects how quickly the temperature changed in a short time ($dt = 0.02s$), which can fluctuate in a large range. The average cooling rate ($\bar{r}_{cooling}$), which is defined as the speed of the temperature drops 20% from the highest point, could better describe the solidification process. Table 4.2.1 compares the instantaneous cooling rate and the average cooling rate of these castings. From Table 4.2.1, the large difference between these two kinds of cooling rate can be seen, for example, the instantaneous cooling rate of Oct. 29 casting is highest, but the average cooling rate is lowest. In this study, we believe that the average cooling rate can describe the solidification process better. These average cooling rates will be related to the grain size at TC 1 locations

in the next chapter to see the effect of the cooling rate on the grain size.

Table 4.2.1 Instantaneous cooling rate and average cooling rate of pyramidal castings.

Casting	July 10	Oct. 23	Oct. 29	Sep. 13	July 25
$r_{cooling}$ (˚C/s)	267.50	378.50	433	371	181
$\bar{r}_{cooling}$ (˚C/s)	170.17	142.69	49.77	136.68	59.90

4.3 Grain size measurement of the pyramidal castings and the test panels

The variation of grain size within the castings has been studied. The SEM images of mid-plane of pyramidal castings were analyzed by CLEMEX software to measure the grain size. For each specimen, 25 locations along the Y-axis and 25 locations parallel with the X-axis were selected to measure the grain size of the α-Mg phase. (Fig. 4.3.1) These locations are marked by number 1 to 25, from top to bottom, and left to right. Table 4.3.1 and 4.3.2 show the grain size of each location. Due to the pyramidal shape, the cooling rate varies with locations in the castings. As a result, the grain size would vary with locations. Theoretically, the tip region of the pyramidal castings would have a relatively small grain size, while the base region would have a larger grain size. Fig. 4.3.2 and Fig. 4.3.3 show how the grain size change in vertical (Y-axis) and horizontal (X-axis) direction.

The same procedure was used to study the grain size of the AE44-2 and AE44-4 panels at the top-, middle-, and bottom regions (as shown in Fig. 3.2.2). Due to the cooling rate varies with the thickness during the high pressure die casting process, the grain size measurement was performed at the skin region and the mid-plane (core region) of the panels. The average grain size of each region is listed in Table 4.3.3. Fig. 4.3.4 and 4.3.5 show the relationship between the location and grain size at the core region and the skin region, respectively.

(a) (b)

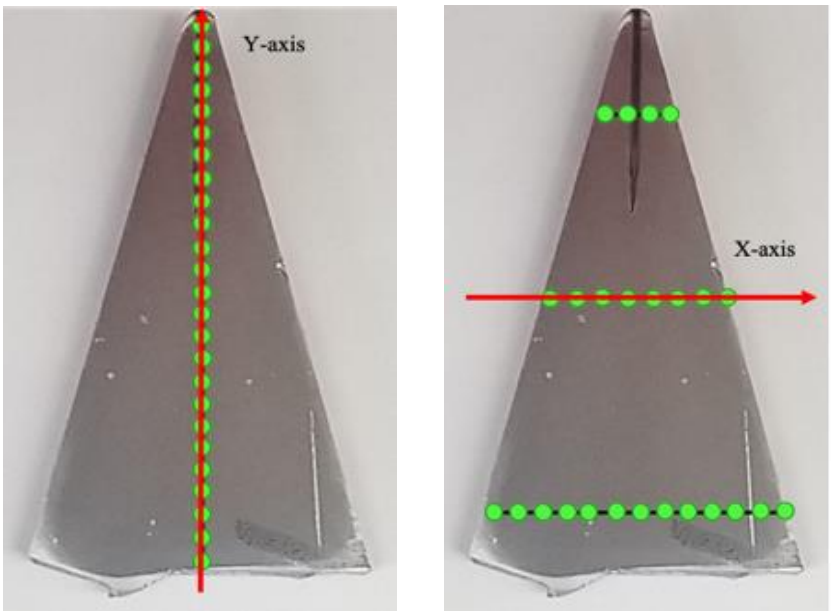

Figure 4.3.1 The points selected to measure the grain size along (a) the Y-axis and (b) the X-axis.

Table 4.3.1 The measured grain size of each location along the Y-axis

AE44-2 (July 25)				AE44-4 (July 10)			
Location Number	Grain Size (μm)	Location Number	Grain Size (μm)	Location Number	Grain Size (μm)	Location Number	Grain Size (μm)
1	3.30	14	6.70	1	5.60	14	18.90
2	9.40	15	11.20	2	7.90	15	13.30
3	13.30	16	11.20	3	7.90	16	18.90
4	11.20	17	5.60	4	7.90	17	22.50
5	11.20	18	9.40	5	7.90	18	7.90
6	7.90	19	18.90	6	15.90	19	7.90
7	7.90	20	9.40	7	7.90	20	15.90
8	11.20	21	13.30	8	7.90	21	11.30
9	11.20	22	11.20	9	15.90	22	18.90
10	13.30	23	11.20	10	9.40	23	15.90
11	11.20	24	11.20	11	9.40	24	26.70
12	15.30	25	11.20	12	15.90	25	26.70
13	9.40			13	15.90		

Table 4.3.2 The measured grain size of each location along the X-axis

AE44-2 (July 25)				AE44-4 (July 10)			
Location Number	Grain Size (μm)	Location Number	Grain Size (μm)	Location Number	Grain Size (μm)	Location Number	Grain Size (μm)
1	9.40	14	9.40	1	6.70	14	9.40
2	5.60	15	13.30	2	9.40	15	9.40
3	7.90	16	15.90	3	5.60	16	13.30
4	11.20	17	11.20	4	<2.80	17	13.30
5	11.20	18	22.50	5	6.70	18	11.20
6	11.20	19	18.90	6	7.90	19	6.70
7	11.20	20	13.30	7	11.20	20	11.20
8	13.30	21	13.30	8	15.90	21	11.20
9	15.90	22	11.20	9	13.30	22	15.90
10	15.90	23	11.20	10	13.30	23	13.30
11	15.90	24	13.30	11	9.40	24	9.40
12	9.40	25	11.20	12	6.70	25	9.40
13	11.20			13	4.70		

In the vertical direction, the experimental data shows that the grain size varies along the Y-axis. However, the variation trend of the grain size is not uniform. (as shown in Fig. 4.3.2) This phenomenon might be caused by some pre-solidified grains formed before the molten alloy was poured into the mold and mixed with the grains formed in the mold. In the AE44-4 HPDC pyramidal specimen, the grain size at the bottom region is 26.70 μm, while the grain size at the tip region reduces to 5.60~7.90 μm. This result is caused by the different cooling rates at the tip and bottom region. The volume of the melt is less in the tip than in the bottom region resulting in a higher solidification rate at the tip. The same trend is also observed in the AE44-2 pyramidal specimen. However, in the AE44-2 HPDC pyramidal specimen, the average grain size at the bottom region is about 11.20 μm, which is much smaller than that of AE44-4 (26.70 μm), then the grain size increases a little bit before it reduces to 3.30μm at the tip. The small grain size at the bottom region of the AE44-2 specimen could be attributed to the melt leak during the casting process.

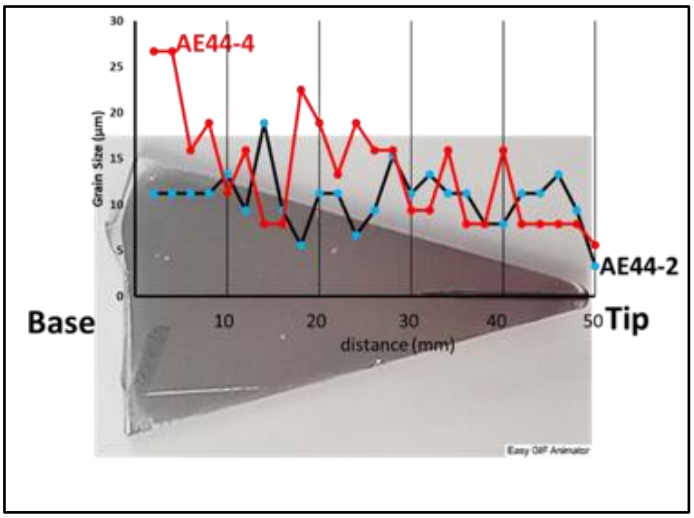

Figure 4.3.2 Variation in average grain size along the Y-axis of AE44-2 and AE44-4 alloys.

In the horizontal direction (shown in Fig. 4.3.3), the grain size of AE44-2 and AE44-4 pyramidal specimens do not show apparent fluctuation in the tip region. This because the volume of the molten alloys is relatively small, and the cooling rate in this region is even. However, in the middle region of the specimens, the grain size increases from the edges to the center. The symmetrical variation trend of the grain size in the middle region results from the different cooling rates of the edges and central region. The edge of the specimen contacts with the mold directly during the solidification so the heat can be conducted out quickly, while the heat conduction at the central region is not as good as the edge of the specimen, so the cooling rate is relatively small at the central region resulting in larger grain size. The variation trend of grain size at the bottom region is not uniform since the bottom region is near the gate of the mold and could be affected by the experiment error.

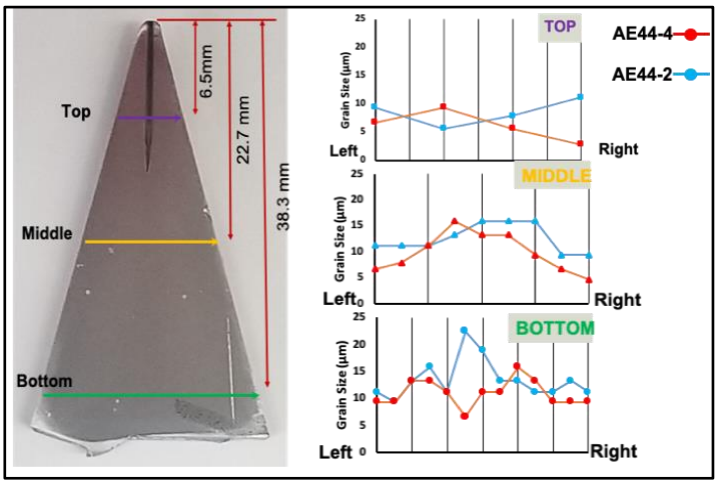

Figure 4.3.3 Variation in average grain size along the X-axis of AE44-2 and AE44-4 alloys.

Table 4.3.3 The average grain size of AE44-2 and AE44-4 panels at different regions

AE44-2			AE44-4		
skin	Top	4.00 μm	skin	Top	5.80 μm
	Middle	7.30 μm		Middle	5.20 μm
core	Top	9.40 μm	core	Top	6.80 μm
	Middle	9.90 μm		Middle	11.30 μm
	Bottom	10.20 μm		Bottom	7.90 μm

In AE44-4 and AE44-2 panels, the grain size changes have a uniform trend. As shown in Fig. 4.3.4 and Fig. 4.3.5, the variation trend of the grain size at the mid-plane (core region) and skin region of both AE44-2 and AE44-4 HPDC panels have a similar trend. The grain size decreases slightly from the center region to the edge of the panels. This result is consistent with the change of the cooling rate.

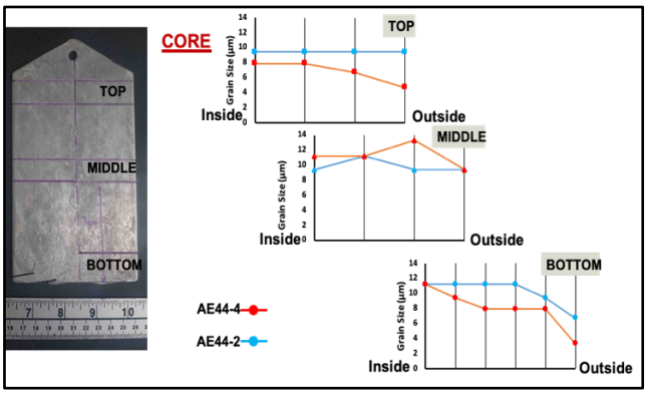

Figure 4.3.4 Variation of average grain size of AE44-2 and AE44-4 panels at the core region

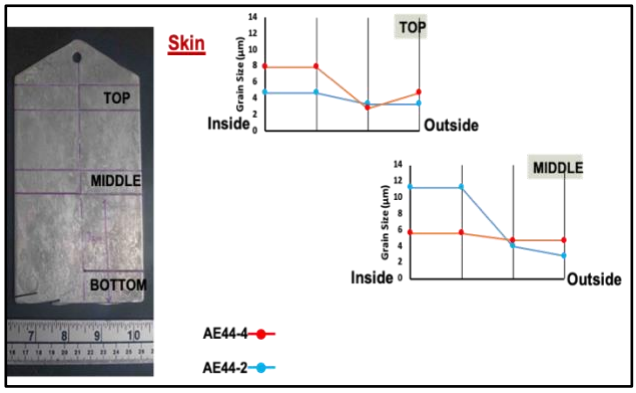

Figure 4.3.5 Variation of average grain size of AE44-2 and AE44-4 panels at the skin region

The temperature of pyramidal casting was monitored directly by a thermocouple at the TC 1 location so that the grain size at this region could be better related to the cooling rate. Three points near the TC 1 location of each pyramidal casting were selected for the grain size measurement. Fig. 4.3.6 shows the SEM images of these points. It should be noted that the image scale of (d3) is 30μm, while others are 70μm. The grain size near the TC 1 location of each specimen does not change a lot. These SEM images were analyzed by Clemex software, and the result was listed in Table 4.3.4. The relationship between grain size and the cooling rate will be discussed in the next chapter.

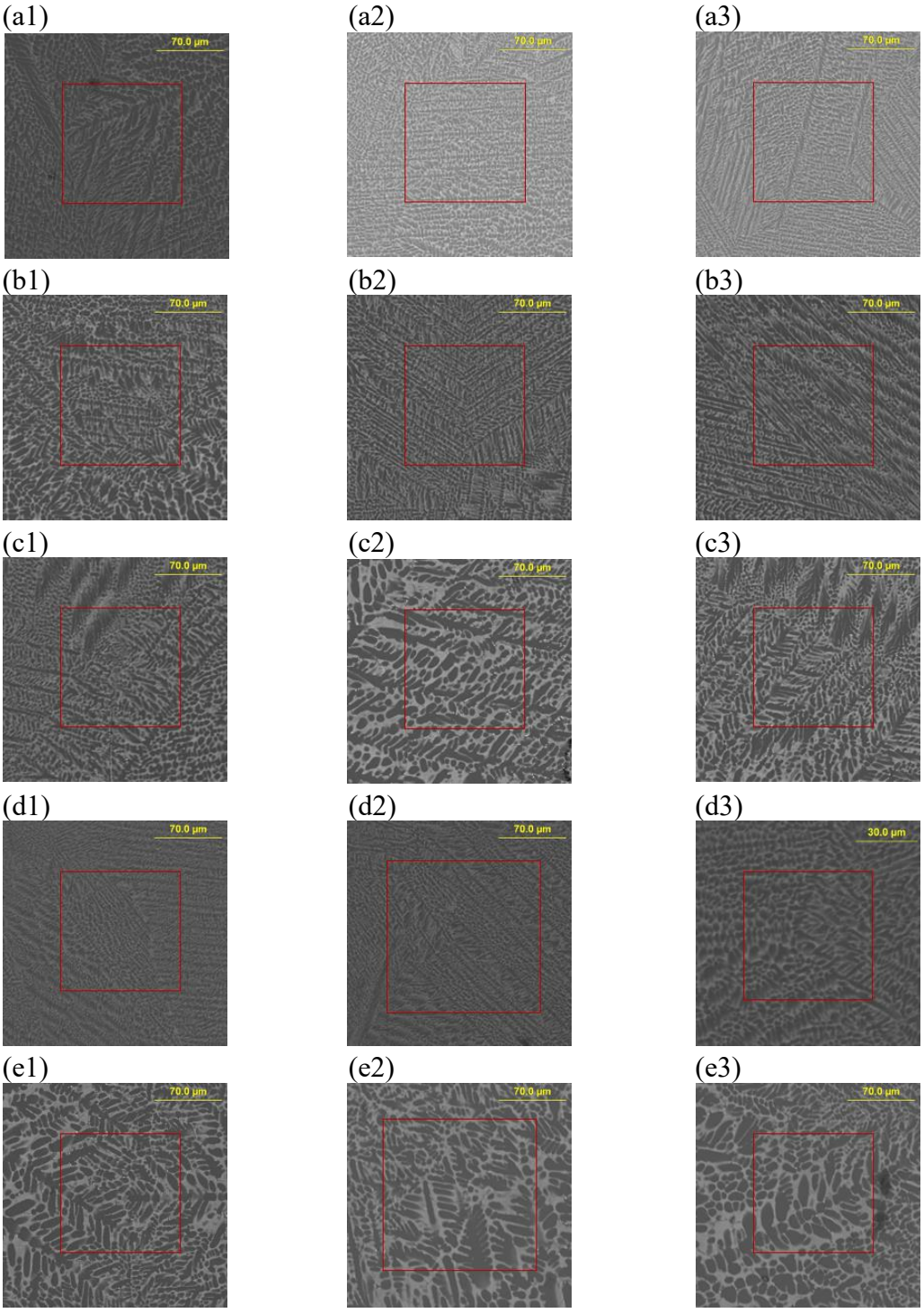

Figure 4.3.6 The SEM images of TC 1 location, show the grain size of (a1-3) July 10, (b1-3) Oct. 23, (c1-3) Oct. 29, (d1-3) Sep. 13, (e1-3) July 25, image scale for all figures is 70 µm but (d3) is 30 µm.

Table 4.3.4 The grain size of each point selected near the TC 1 location

Casting / Location	July 10	Oct. 23	Oct. 29	Sep. 13	July 25
Point1	9.40 μm	9.40 μm	4.70 μm	5.60 μm	13.30 μm
Point 2	5.60 μm	4.70 μm	9.40 μm	4.70 μm	9.40 μm
Point 3	5.60 μm	5.60 μm	6.70 μm	4.70 μm	9.40 μm

4.4 The hardness of HPDC AE44-2 and AE44-4 panels

Hardness is an important mechanical property of a material. The hardness of the metal is determined by lots of factors such as chemical composition, microstructure, etc. This study compares the hardness of AE44-2 and AE44-4 HPDC panels at various locations (Fig.3.4.1). The method of hardness measurement has been introduced in the previous chapter. The results are shown in Table 4.4.1. The grain size (GS) shown in Table 4.4.1 is measured by Image J software, using the optical microscope image of each test point. Fig. 4.4.1 demonstrates how the hardness change through the HPDC panels. The relationship between hardness and microstructure will be discussed in chapter 5.

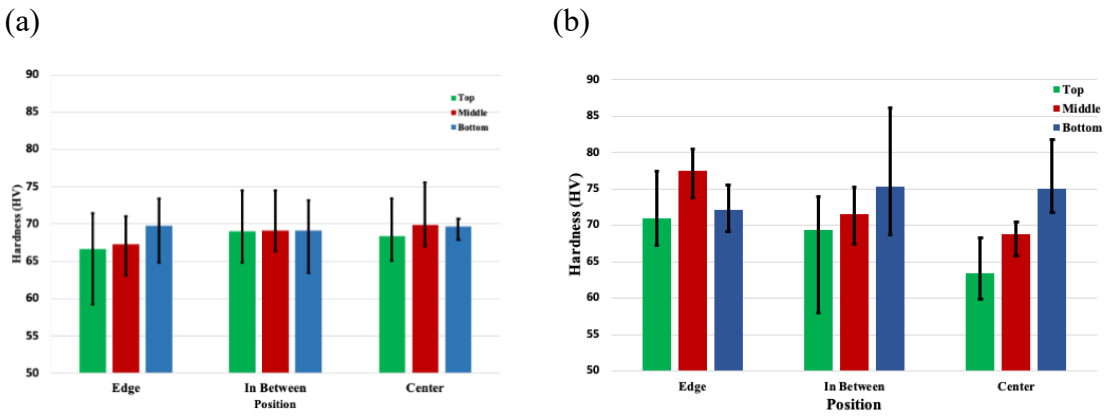

Figure 4.4.1 The Vickers Hardness of (a) AE44-2 panel and (b) AE44-4 panel.

Table 4.4.1 The Vickers Hardness and grain size of AE44-2 and AE44-4 panels at the top-, middle, and bottom-region (each region has three different points: edge, in between, and center).

AE44-2			AE44-4		
Edge	Top	66.68 (GS= 1.90μm)	Edge	Top	70.96 (GS= 1.90μm)
	Middle	67.24 (GS= 1.70μm)		Middle	77.501 (GS=NA)
	Bottom	69.73 (GS= 1.70μm)		Bottom	72.09 (GS= 2.40μm)
In Between	Top	69.07 (GS= 0.80μm)	In Between	Top	69.334 (GS= 1.65μm)
	Middle	69.18 (GS= 1.80 μm)		Middle	71.52 (GS= 1.50μm)
	Bottom	69.17 (GS= 1.30μm)		Bottom	75.373 (GS= 1.60μm)
Center	Top	68.36 (GS=1.60 μm)	Center	Top	63.44 (GS= 1.25μm)
	Middle	69.89 (GS= 1.20μm)		Middle	68.94 (GS= 1.65μm)
	Bottom	69.63 (GS= 1.60μm)		Bottom	75.09 (GS= 1.50μm)

4.5 Results of spherical micro-indentation testing

The micro-indentation test is an ideal method to study the local mechanical properties of the materials, not only the hardness but also the stress-strain response and creep resistance. In this study, the single load-unload spherical micro-indentation tests were performed on the tip-, TC 1-, and the bottom regions of the pyramidal castings (as Fig. 4.5.1shown) to study the stress-strain response of AE44-2 and AE44-4 alloys. The multiple load-unload spherical micro-indentation tests were performed on the skin and core of the panels and the Oct. 23 (AE44-4), July 25 (AE44-2) pyramidal specimens to study the local stress-strain response at the regions with different grain size. All specimens were tested at 25˚C and 200˚C. Table 3.4.1 has shown detailed information about the spherical micro-indentation tests performed on each specimen.

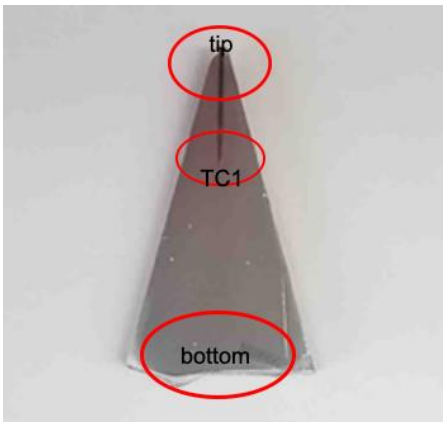

Figure 4.5.1 The regions of pyramidal specimens performed spherical micro-indentation tests.

Due to the variation of temperature was monitored at the TC 1 location, the spherical micro-indentation tests were firstly performed on this region to study the effect of cooling rate on the mechanical properties. Fig. 4.5.2 shows typical indentations around the TC 1 location. The distance between the indentations is controlled around 100±10 μm. The radius of an indentation, as shown in Fig. 4.5.2, is about 15±1μm. (the scale is 2 μm)

(a) (b)

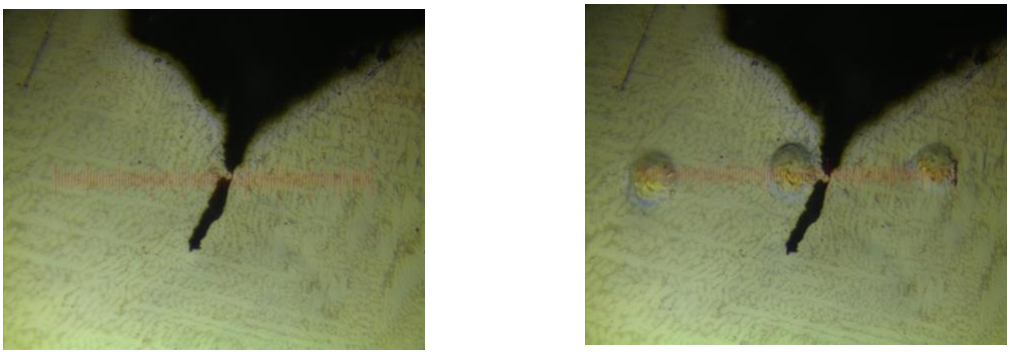

Figure 4.5.2 The typical optical microscopy picture of the TC 1 location (a) before and (b) after indentation tests

The load-depth curves obtained by single load-unload spherical micro-indentation tests on each specimen at 25˚C and 200˚C are shown in Fig. 4.5.3 and Fig. 4.5.4, respectively. The different colors of lines represent the different regions: the red lines are the load-depth curve of the indentations at the TC 1 location, while the blue lines are that at the tip region (small grain size), and the green line is that at the bottom region (large grain size). All these curves are converted to stress-strain curves by the analytical approach introduced in chapter 2 (equation 2.8.18 and 2.8.20). The resulting stress-strain curves will be shown and discussed in the following chapter. The curves obtained at 25˚C indentation tests have higher repeatability. While the load-depth curves obtained at 200˚C are more unstable than that at 25˚C.

(a) (b)

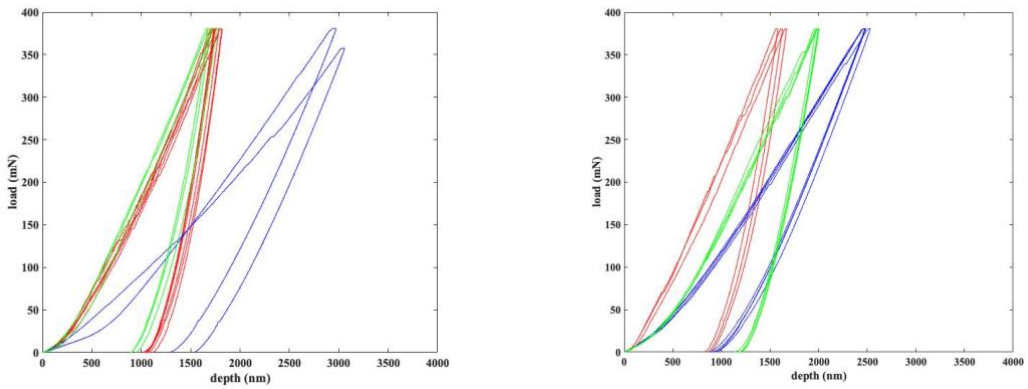

(c) (d)

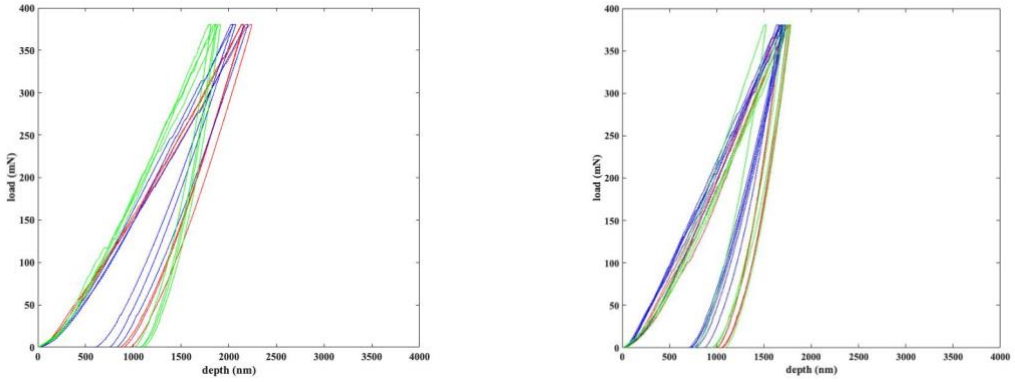

Figure 4.5.3 Load-depth curves of spherical micro-indentation tests at 25˚C (a) AE44-2 (July 25), (b) AE44-2 (Oct. 29), (c) AE44-2 (Sep. 13), (d) AE44-4 (Oct. 23).

(a) (b)

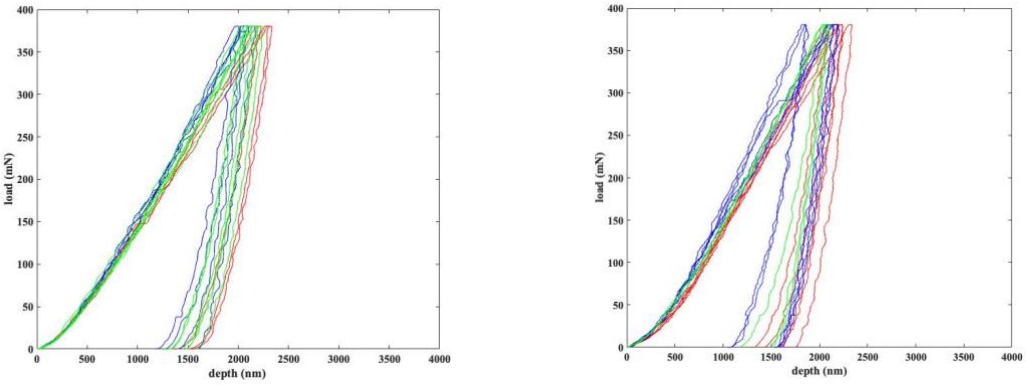

(c)

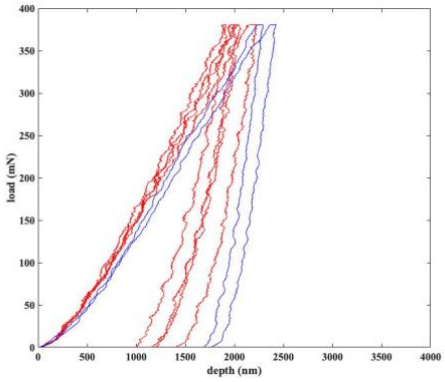

Figure 4.5.4 Load-depth curves of spherical micro-indentation tests at 200˚C (a) AE44-2 (Oct. 29), (b) AE44-4 (Oct. 23) (c) AE44-4 (July 10).

The single load-unload spherical indentation tests aim to study the stress-strain response of AE44-2 and AE44-4 specimens at different temperatures. While the multiple load-unload spherical indentation tests were performed at the pyramidal specimens and panels to investigate the effect of grain size on the mechanical properties of AE44-2 and AE44-4 alloys. The results of multiple load-unload indentation tests are shown in Fig. 4.5.5. It should be noted that the different color of curves represents the different specimens, the red lines are pyramidal castings, the blue lines are core region of the panels, the green lines are skin region of the panels. Unlike single load-unload indentation tests, the multiple load-unload are performed at regions with different grain size. These two kinds of indentation tests were converted into stress-strain curves using the new analytical approach. It should be noted that the new analytical approach only uses the loading part of the load-depth curves to deduce the stress-strain response.

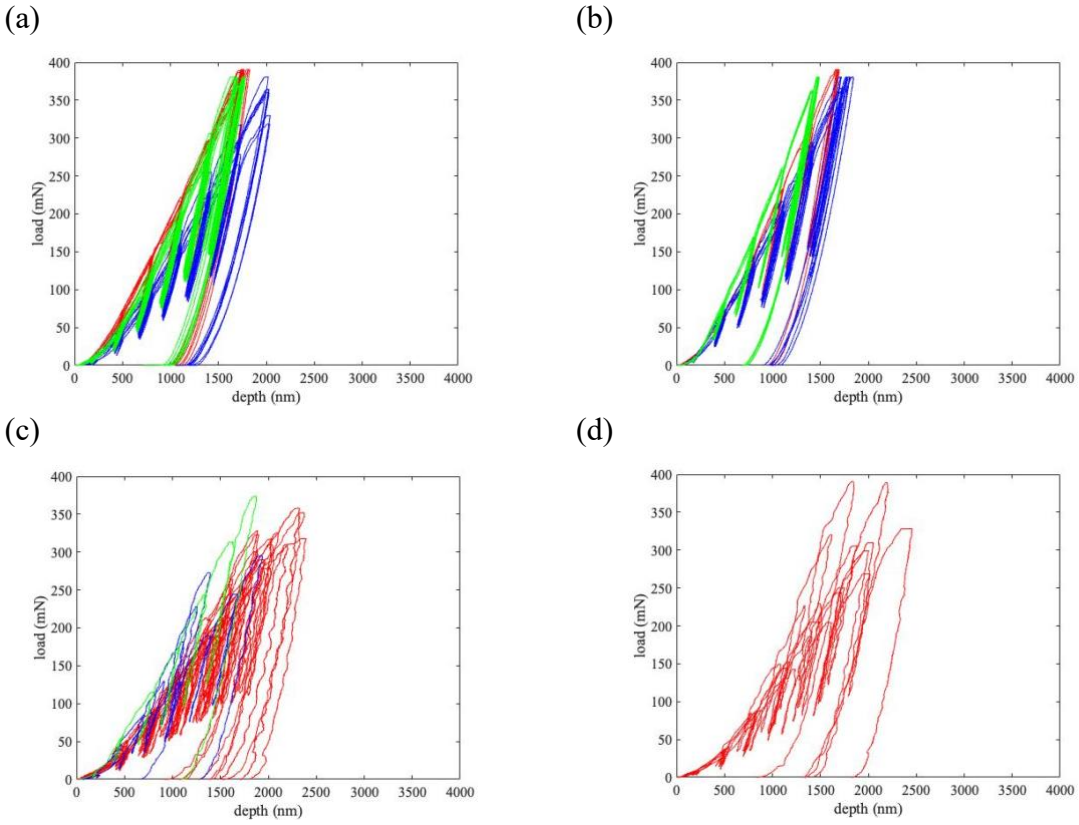

Figure 4.5.5 Load-depth curves of multiple load-unload spherical micro-indentation tests of (a) AE44-2 at 25˚C, (b) AE44-4 at 25˚C, (c) AE44-2 at 200˚C, (d) AE44-4 at 200˚C.

In these load-depth curves, the pop-ins can be observed at the loading segment. Pop-in is a phenomenon occurring at the indentation tests that the indentation depth suddenly increases while the indentation load does not change a lot.[66] As a result, there are some little plateaus appear in the loading segment. It is reported that this phenomenon might cause by the plasticity initiation and elastic-plastic transition.[66] The occurrence of this phenomenon is also affected by various factors such as grain boundaries in the stress field, grain orientation relationship, surface roughness of the specimens, and the density of dislocation within the specimens.[66][59]

4.6 Tensile tests of AE44-2 and AE44-4 specimens.

As introduced in chapter 3, the tensile tests were performed on both AE44-2 and AE44-4 alloys at 25˚C and 200˚C to study the mechanical properties of these two materials. As a reference, the tensile stress-strain curves of AE44 alloy provided by Meridian Magnesium is also present in this section. The tensile stress-strain curves of AE44-2 and AE44-4 specimens are shown in Fig 4.6.1and 4.6.2. The black curves in Fig. 4.6.1 and 4.6.2 are generated using Meridian's data, while the colored curves are obtained by the tensile tests, which have been introduced in previous chapter.

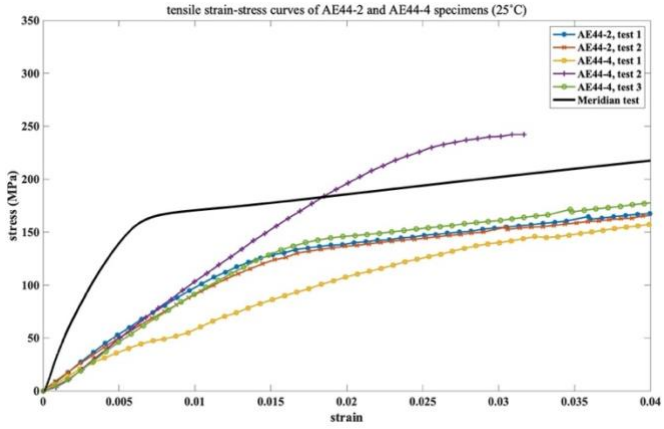

Figure 4.6.1 Comparison of stress-strain curves measured by the tensile tests and the Meridian magnesium (at 25˚C).

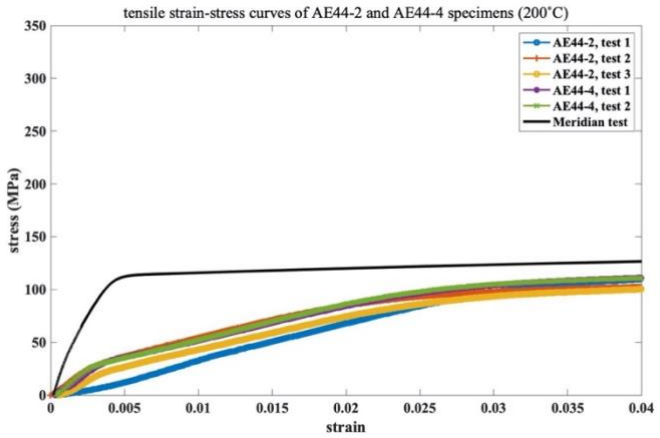

Figure 4.6.2 Comparison of stress-strain curves measured by the tensile tests and the Meridian Magnesium (at 200˚C).

It is clear that the results of our tensile tests are incorrect. Compared with Meridian's result, our stress-strain curves are flatter, and the measured yield point is lower and appears at the larger strain. This is the result of the different methods used to measure the strain. For our tensile tests, the calculation method of strain is based on the motion of the cross-head, which has been introduced in section 3.6. Our method is not perfect and tends to result in a large strain. For Meridian's test, they might use the strain gauge, which is attached directly to the specimen gauge length, and precisely measure the strain. It should be noted that the process history of Meridian's specimens is not clear, so the mechanical properties of Meridian's specimens might be different from our specimens.

4.7 Indentation creep tests of AE44-2 and AE44-4 specimens.

The poor creep resistance of most magnesium alloys is a huge limitation of further applying this material, so it is essential to understand the creep behavior of AE44-2 and AE44-4 alloys. In order to compare the creep resistance of AE44-2 and AE44-4 alloys, the constant load creep tests were performed by Alemnis indentation tester made by Alemnis company (Thun, Switzerland). The depth-time curves of constant load creep indentation tests are

shown in Fig.4.7.1. The creep tests are performed at the tip-, TC 1-, and bottom- region of AE44-2 pyramidal casting and tip region of AE44-4 pyramidal casting and the core region of AE44-4 panel. Fig.4.7.1.c and Fig. 4.7.1.d demonstrate the creep tests performed at 200˚C.

It should be noted that the maximum load applied to specimens is 20mN and continues for 3600 seconds. After a constant-load test, the applied load is reduced to 2mN to calculate the degree of thermal drift in the indentation load output. In general, creep displacement increases with temperature by order of magnitude (as shown in Fig. 4.7.1). The variability among the tests is very high, especially for AE44-4 specimens. The reason for this phenomenon is not clear yet. Maybe more creep tests are needed for more high-quality data.

(a)

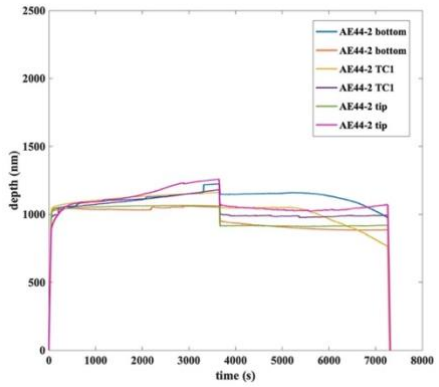

(b)

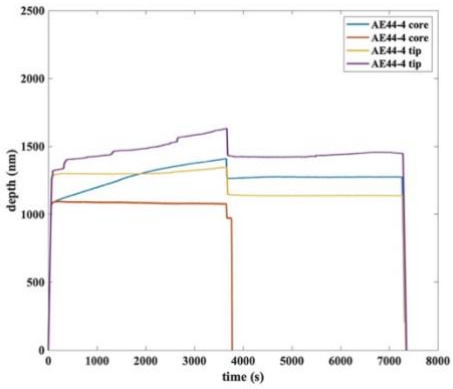

(c)

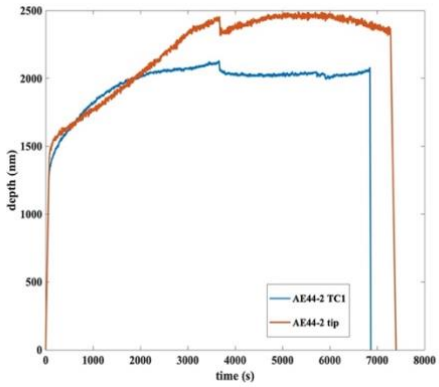

(d)

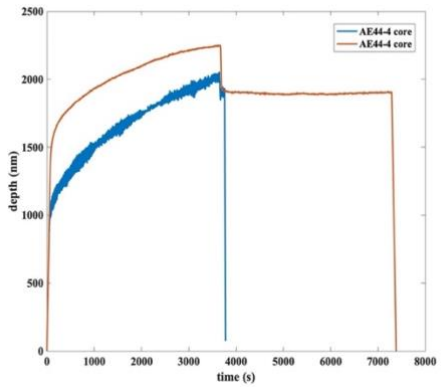

Figure 4.7.1 Depth-time curves of constant load creep tests (a) AE44-2 at 25˚C, (b) AE44-4 at 25˚C, (c) AE44-2 at 200˚C, (d) AE44-4 at 200˚C. (constant load = 20 mN, holding time = 3600 s)

The aim of chapter 4 is to demonstrate the results of this study, such as the chemical composition and variation of grain size of AE44-2 and AE44-4 castings, the cooling rate at TC 1 location of different pyramidal castings, the variation of hardness through the specimens. The results of spherical micro-indentation tests and constant loading creep tests are also introduced in this chapter. These results are going to be further discussed in the next chapter.

Chapter 5

5 Discussion

Previous chapters have introduced the background information, experimental method, and the results of various tests. All the works are aiming at the relationship between microstructure and mechanical properties of AE44-2 and AE44-4 alloys. The only difference between these two kinds of alloys is the RE additions. This study compares the mechanical properties of AE44-2 and AE44-4 high pressure die-castings. If the mechanical properties, especially the elevated temperature mechanical properties, of AE44-2 are similar to that of AE44-4, the AE44-2 could be an economical replacement of AE44-4 alloy. In this chapter, the results, which have been introduced in chapter 4, will be discussed. This chapter focuses on: (i) The relationship between Vickers hardness, grain size, and the cooling rate at the TC 1 location of AE44-2 and AE44-4 castings. (ii) Stress-strain response of AE44-2 and AE44-4 castings deduced from spherical micro-indentation tests at 25˚C and 200˚C. (iii) Comparison of stress-strain response obtained from spherical indentation tests with that obtained from tensile tests. (iv) The effect of grain size on the stress-strain response. (v) The steady-state creep behavior of the two alloys.

5.1 Vickers hardness of AE44-2 and AE44-4 panels versus grain size

The Vickers hardness has been measured at the top-, middle-, and bottom regions of high pressure die-cast panels, the results were shown in section 4.4. The hardness varies with the location within the panels. Hall et al. claimed that the hardness has a negative correlation with grain size and found that the hardness has a linear relationship with $1/d^{1/2}$, where d is the diameter of the grains.[67]

Fig. 5.1.1 illustrates the relationship between Vickers hardness and $d^{-1/2}$. Two different

trends are shown in this plot. As Hall et al. proposed, a "good" linear relationship should exist between hardness and $d^{-1/2}$.[67] As shown in Fig. 5.1.1, the Vickers hardness and $d^{-1/2}$ do not show a strong linear relationship. The explanation for this result is: (i) The collected data are not sufficient to illustrate the relationship between hardness and grain size. (ii) The grain size throughout the surface of high pressure die-cast panels does not change a lot, so the relationship of hardness and grain size cannot be studied in a wide range of grain size. (iii) There might be another factor that influences the hardness of AE44-2 and AE44-4, Yong et al. proposed that it is the density of prior dislocations in the polycrystalline metals rather than the grain size that influences the hardness of specimens.[68] Since the AE44-2 and AE44-4 specimens were prepared following the same procedure, the only factor that might cause the difference in the density of prior dislocations is the RE additions in AE44-2 and AE44-4. In order to clarify the reason accounting for this result, more tests need to be performed, especially on the pyramidal specimens, because the grain size of the pyramidal castings change a lot from the tip region to the bottom region.

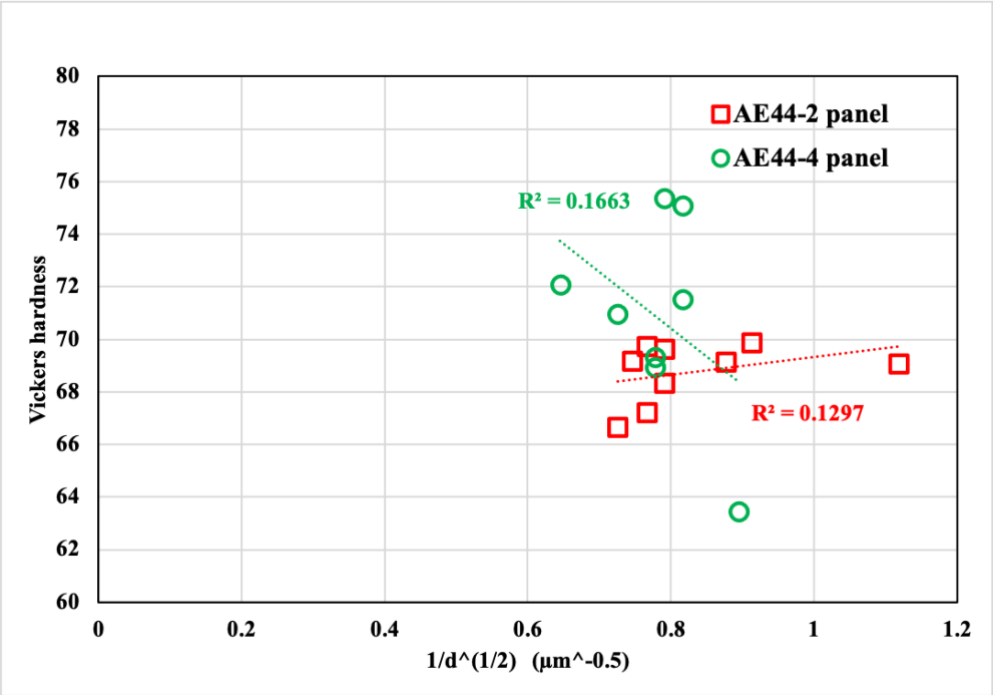

Figure 5.1.1 Vickers Hardness-$d^{-0.5}$ scatter plot of AE44-2 panel (red square) and AE44-4 panel (green circle)

5.2 Effect of cooling rate on the grain size

It is generally accepted that the cooling rate has a significant effect on the grain size, with a high cooling rate resulting in small grain size. The cooling rate of pyramidal castings used in this study decreases form tip region to bottom region, while the grain size of AE44-2 and AE44-4 pyramidal castings increases form the bottom region to the tip region (Fig. 4.1.4). To further study the effect of cooling rate on grain size, the TC 1 location of pyramidal casting is selected. The cooling rate and grain size have been shown in chapter 4 (section 4.2 and 4.3), Fig. 5.2.1 shows the variation of grain size with the cooling rate at the TC 1 location.

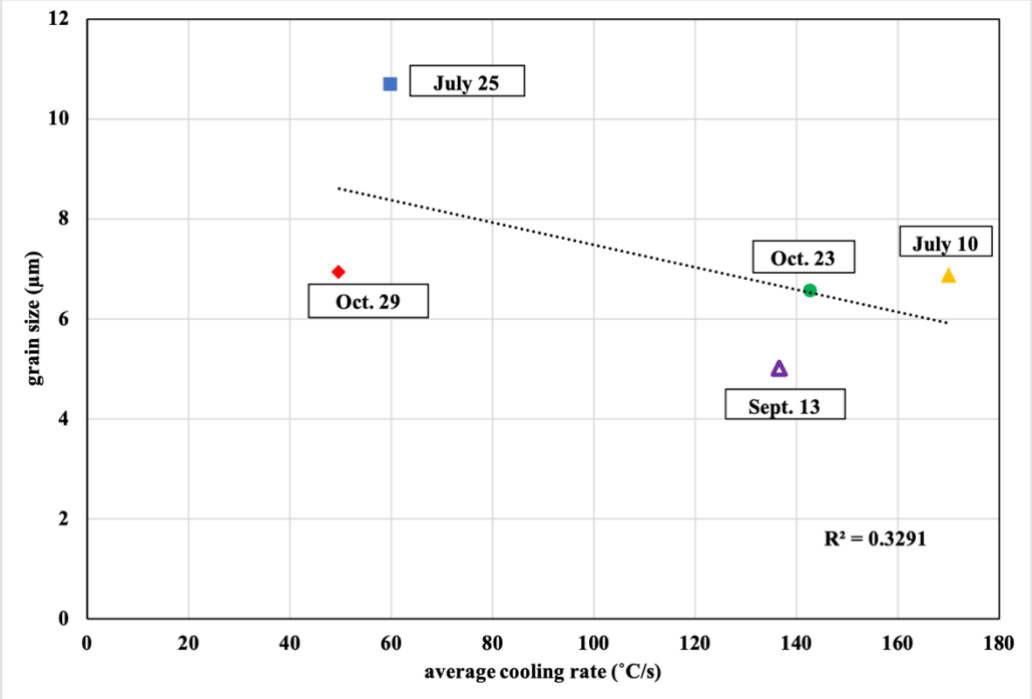

Figure 5.2.1 Grain size-average cooling rate at TC 1 location of pyramidal castings (AE44-2: July 25, Sep. 13, Oct. 29; AE44-4: July 10, Oct. 23)

It is clear that the grain size has a negative correlation with the cooling rate. The reason is easy to understand. During a high cooling rate, the grain size does not have enough time to grow, and therefore the grain size is small. Easton et al. proposed an equation relating the

grain size to cooling rate, solute content, and nucleant particles[69]

$$d = a + \frac{b}{Q\sqrt{\bar{r}_{cooling}}} \quad (5.2.1)[3]$$

Where a and b are constant. Q is the growth restriction factor, which is relating to the chemical composition of alloys. Q is calculated by this equation Q =$\sum_i m_i C_{o,i}(k_i - 1)$, where $C_{o,i}$ represents the concentration of alloying element *i* in magnesium alloys.[70] Lee et al. and St John et al. have posted $m_i(k_i - 1)$ value of most alloying elements[71][72]. According to their work, the Q value of AE44-2 and AE44-4 can be calculated (it should be noted that the Q value of La, Nd, and Pr has not been posted yet, so the Q value of RE elements in AE44-2 and AE44-4 alloys is simply regarded as Q value of Ce). The resulting Q value of AE44-2 and AE44-4 alloys is 28.71 and 28.32, respectively. Since the difference of Q value of AE44-2 and AE44-4 is small, the following calculation uses the average Q value = 28.51 for both AE44-2 and AE44-4. Input this Q value in the equation based on equation 5.2.1 and find the liner function between grain size (*d*) and $\bar{r}_{cooling}{}^{-0.5}$. Fig. 5.2.2 illustrates the *d*-$\bar{r}_{cooling}{}^{-0.5}$ scatter plot, from which a fitted linear function is obtained.

From Fig. 5.2.2, the relationship between *d* and $\bar{r}_{cooling}{}^{-0.5}$ can be roughly seen as liner. According to equation 5.2.1, the characteristic function of the grain size of AE44-2 and AE44-4 specimens can be determined as:

$$d = 3.12 + \frac{1128.18}{28.51\sqrt{\bar{r}_{cooling}}} \quad (5.2.2)$$

It should be noted that this function can only qualitatively reflect the relationship between grain size and cooling rate of AE44-2 and AE44-4. For more accurate function, more data are needed. The result of this section shows that the cooling rate does have a significant effect on grain size. The grain size is relatively small when the cooling rate is high. However,

the complicated mechanism of how the cooling process can influence the grain size of as-cast AE44-2 and AE44-4 alloys still needs to be studied in future work.

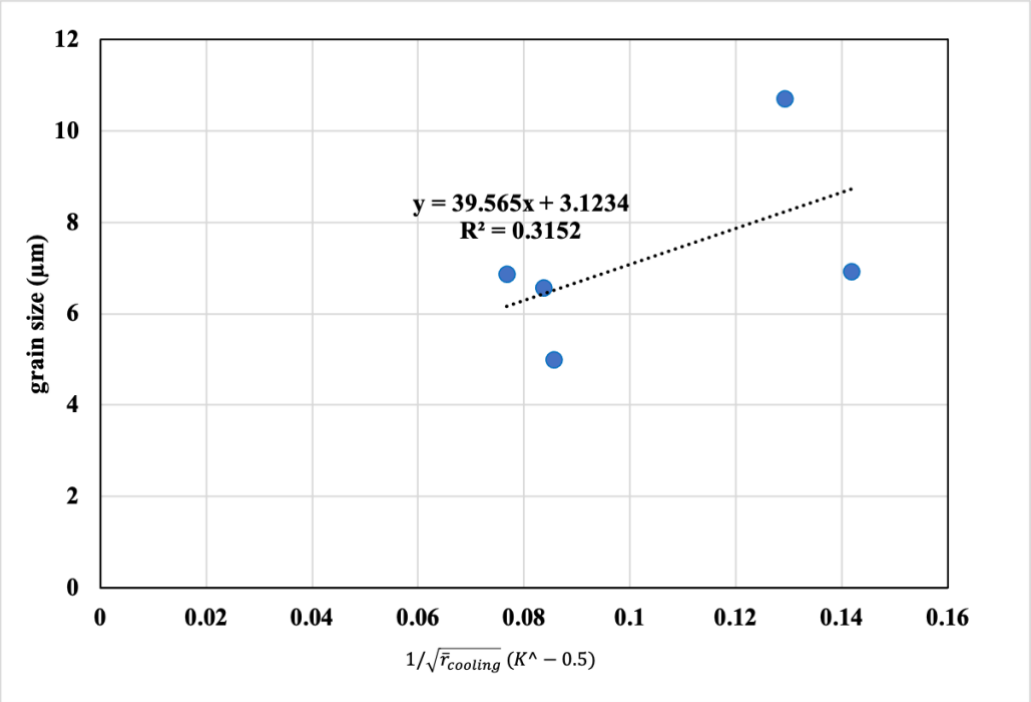

Figure 5.2.2 d-$\bar{r}_{cooling}^{-0.5}$ scatter plot of pyramidal castings.

5.3 Indentation stress-strain response of the specimens

The mechanical properties of AE44-2 and AE44-4 alloys are the most focused part of this study. The advantages of magnesium alloys have been introduced in chapter 2, the specific strength and cast-ability of magnesium alloys are excellent, but the elevated temperature mechanical properties of magnesium alloys are relatively poor. In this section, the stress-strain response deduced from spherical micro-indentation tests will be discussed. The indentation- and tensile- stress-strain response will also be compared to check the reliability of the analytical procedure used in this study and propose a possible solution to improve this analytical procedure. As introduced in chapter 3, the spherical indentation tests were performed at 25˚C and 200˚C (Table 3.5.1 shows detailed information about the spherical indentation tests). The results of spherical indentation were then converted into the stress-

strain curves by using the equation 2.8.18 and 2.8.20 (shown below).

$$\varepsilon = \frac{0.2}{R}\sqrt{5\left(\frac{2-n}{4+n}\right)hR - \left(\frac{5(2-n)}{2(4+n)}h\right)^2} \tag{2.8.18}$$

$$\sigma = \frac{P(2+n)}{6\pi\left(5\left(\frac{2-n}{4+n}\right)hR - \left(\frac{5(2-n)}{2(4+n)}h\right)^2\right)\left(\frac{40}{9\pi}\right)^n} \tag{2.8.20}$$

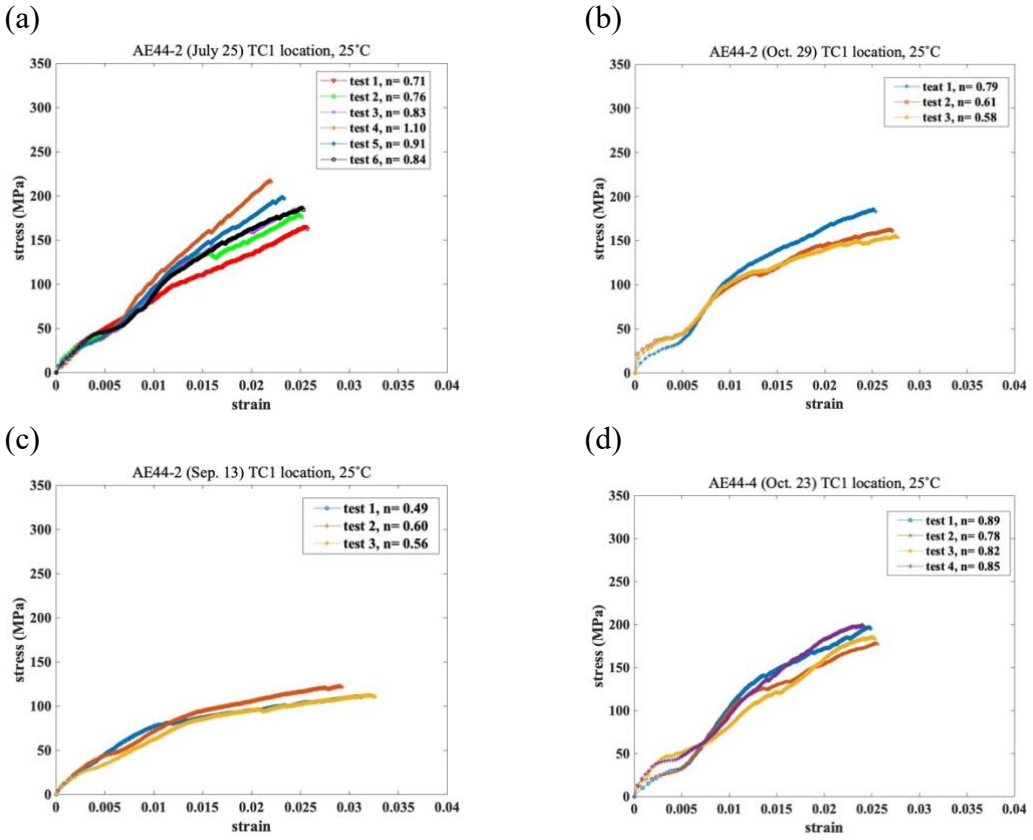

Figure 5.3.1 Indentation stress-strain curves of (a) July 25, (b) Oct. 29, (c) Sep. 13, (d) Oct. 23 pyramidal castings at TC 1 location and 25˚C.

Fig. 5.3.1 demonstrates the deduced stress-strain curves of pyramidal castings at TC 1 location and 25˚C. For the AE44-2 alloys (July 25, Oct. 29, Sep. 13), the stress-strain curves have the same trend when the strain is less than ε = 0.01, while the difference between each stress-strain curve becomes larger when the strain is larger than ε = 0.01. This could be the result of flaws on the surface of the specimens. Compared with Oct. 29 specimen (Fig.

5.3.2.c), the surface condition of the July 25 specimen has more scratches and other flaws, and the grain size under the indentation is not uniform (Fig. 5.3.2.a and 5.3.2.b shown). The average stress at strain ε = 0.025 is around 150 MPa for the July 25 and Oct. 29 specimens, while it is around 110 MPa for Sep. 13 specimen. The lower stress observed in Sep. 13 specimen might have resulted from a poorer quality surface condition at this location.(as shown in Fig 5.3.3.d). This suggests that the roughness of the indentation surface might cause this difference in stress-strain response.

For AE44-4 (Oct. 23) specimen, the stress-strain curves demonstrate two kinds of trends: the stress of test 1 and test 2 is lower than that of test 3 and 4 at the strain less than ε = 0.005. While this situation is reversed when the strain is larger than ε = 0.01(Fig. 5.3.1.d). Meanwhile, the first two tests have a more apparent flat stage at the small strain (less than ε = 0.005). Fig. 5.3.2.e and 5.3.2.f are the pictures of the indentations on the AE44-4 Oct. 23 specimen. As Fig. 5.3.2.e shows, tests 1 and 2 are relatively far away from the cavity of the TC 1 thermocouple. The dark area is the cavity, while tests 3 and 4 are near the cavity.

In this study, we assume that the stress-strain response of the AE44-2 and AE44-4 alloys follow a power-law dependence upon strain (equation 5.3.1). The resulting curves were fitted by the "CFTOOL" in MATLAB software, and the strain hardening exponent (n) and the pre-exponent term (A) of each stress-strain curve are calculated and listed in Tables 5.3.1- 5.3.6.

$$\sigma = A\,\varepsilon^{n}\ (\sigma > \sigma_y) \tag{5.3.1}$$

As Fig. 5.3.3 shows, some of the stress-strain curves demonstrate a negative correlation at small strains ($\varepsilon < 0.005$). This result is related to several factors, including the indentation surface condition and the accuracy of the analytical technique for accounting for surface roughness. Of all the 160 spherical indentation tests performed in this thesis research 38 tests produced this negative σ – ε correlation at low strains ($\varepsilon < 0.005$). The data from these tests were not included in subsequent analyses shown in this chapter.

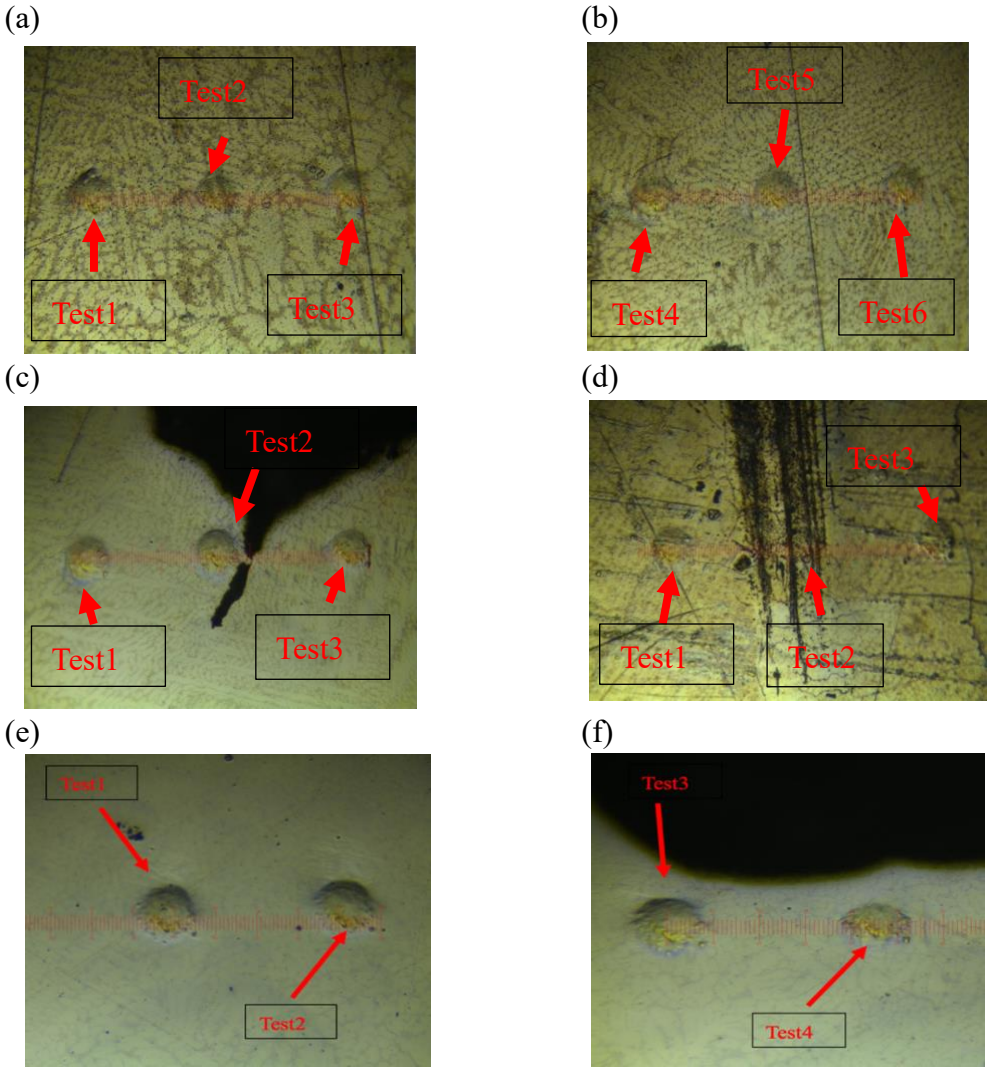

Figure 5.3.2 The optical microscopy pictures of indentations on (a)&(b) July 25 casting, (c)Oct. 29 casting, (d) Sep. 13 casting, (e)&(f) Oct. 23 casting.

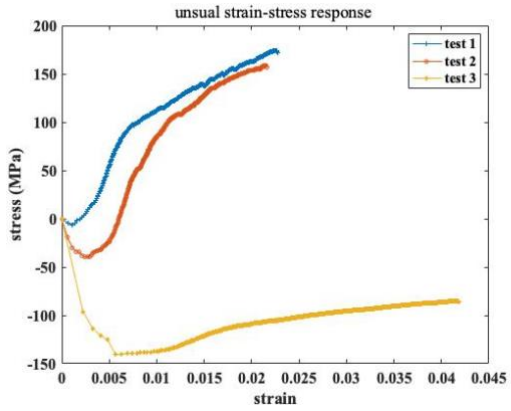

Figure 5.3.3 Unusual results generated by the analytical approach.

Table 5.3.1 includes the values of n and A of each curve. It should be noted that the value of the strain hardening exponent varies with the specimens. For three AE44-2 specimens, the average n value ranges from 0.49 (Sep. 13) to 1.10 (July 25). Additionally, even on the same specimen, the n value varies with the indentations. One reason for this is that the n value is obtained by fitting the log(strain)-log(stress) curves using the "CFTOOL" function in MATLAB, and the error of this approach is unavoidable. In order to evaluate the fitted results, the R^2 is introduced. In this study, all the value of R^2 remains above 0.8, which suggests a relatively linear relationship between log(strain) and log(stress).

Table 5.3.1 The calculated values of n, A, and R^2 of all deduced stress-strain curves (TC 1 location, 25˚C).

Casting date	AE44-2 alloys, TC 1 location, 25˚C				Average value
July 25		n	A	R^2	$n_{average} = 0.84$ $A_{average} =$ 5.11E+03
	Test 1	0.71	2.19E+03	0.99	
	Test 2	0.76	3.04E+03	0.97	
	Test 3	0.83	4.09E+03	0.97	
	Test 4	1.10	1.09E+04	0.99	
	Test 5	0.91	6.12E+03	0.98	
	Test 6	0.84	4.36E+03	0.98	
Oct. 29	Test 1	0.79	3.65E+03	0.94	$n_{average} = 0.66$ $A_{average} =$ 2.16E+03
	Test 2	0.61	1.51E+03	0.95	
	Test 3	0.58	1.31E+03	0.94	
Sep. 13	Test 1	0.49	648.6151	0.93	$n_{average} = 0.55$ $A_{average} = 844.46$
	Test 2	0.60	1.07E+03	0.97	
	Test 3	0.56	809.9585	0.95	
Casting date	AE44-4 alloys, TC 1 location, 25˚C				Average value
Oct. 23	Test 1	0.89	5.63E+03	0.94	$n_{average} = 0.83$ $A_{average}$ =4.43E+03
	Test 2	0.78	3.34E+03	0.93	
	Test 3	0.82	3.79E+03	0.98	
	Test 4	0.85	4.97E+03	0.97	

It should be noted that in some specimens the stress-strain curves illustrate a little flat stage at the very small strain (0~0.005). This phenomenon implies that some complicated deformation mechanism might be involved during the micro-indentation test. We believe

that the little flat stage observed in this study is caused by twinning deformation. Cáceres et al. studied the strain hardening behavior of Mg caused by twinning and found a similar stress-strain response in pure magnesium.[73]

As introduced in chapter 4, the grain size changes along the Y-axis of pyramidal castings, so the spherical micro-indentation tests were performed at the tip- and bottom- region to study whether the mechanical properties would vary with different regions. The deduced stress-strain curves are shown in Figs. 5.3.4 and 5.3.6 follow the same procedure the value of n, A, and R^2 are list in Tables 5.3.2 and 5.3.3.

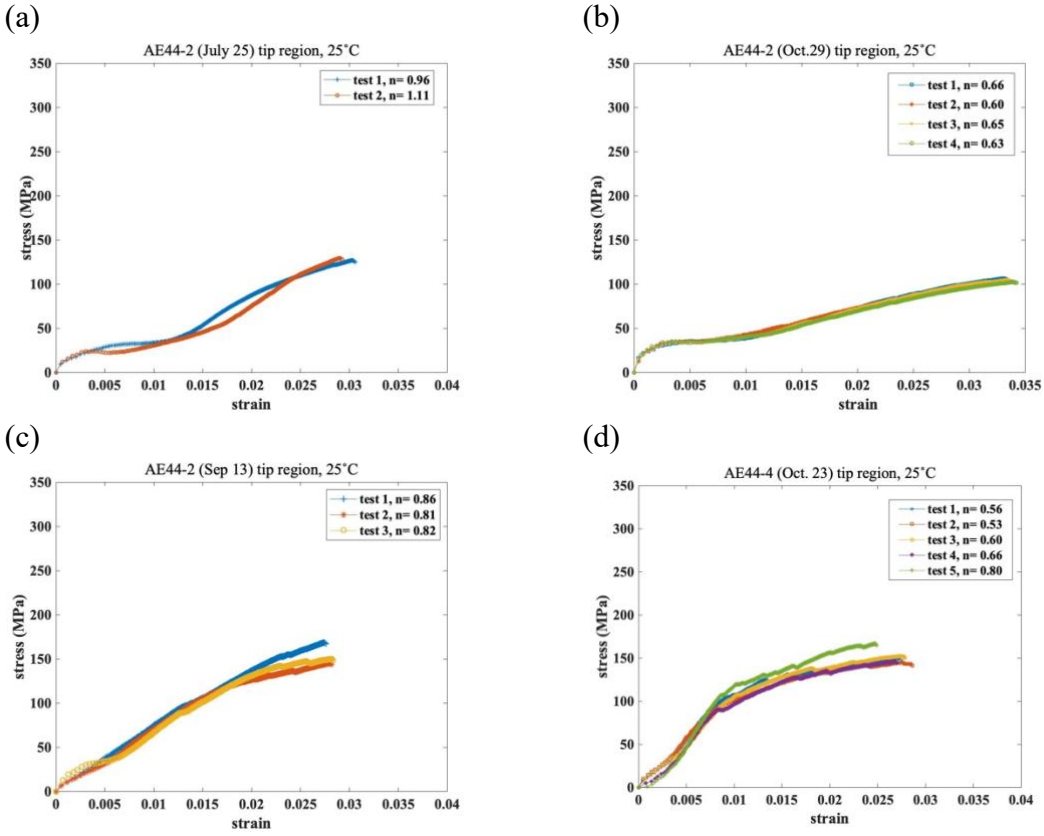

Figure 5.3.4 Indentation stress-strain curves of (a) July 25, (b) Oct. 29, (c) Sep. 13, (d) Oct. 23 pyramidal castings at tip region and 25˚C.

Compared with the TC 1 location, the deduced stress-strain curves at the tip region of all pyramidal castings appear to follow a more similar trend. The n value of all AE44-2 and AE44-4 specimens at the tip region is different at the TC 1 location. This could attribute to the surface condition of the tip region. Fig. 5.3.5 demonstrates the picture of the tip region

of all specimens before indentation testing.

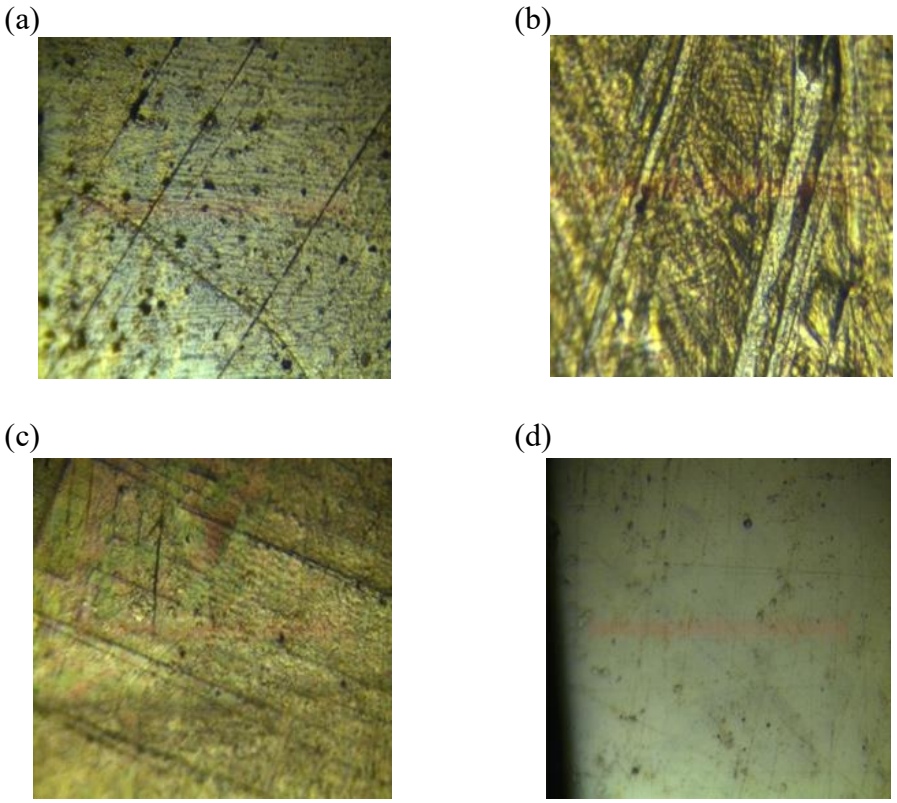

Figure 5.3.5 The optical microscopy pictures of (a) July 25 casting, (b) Oct. 29 casting, (c) Sep. 13 casting, (d) Oct. 23 casting at tip region.

Form Fig. 5.3.5, the poor surface condition of AE44-2 specimens at tip region can be seen. This kind of surface could result in the error in the indentation load-depth curves and the deduced stress-strain response, while the surface of Oct. 23 casting (AE44-4 alloy) is relatively "good," although the scratches can be seen. The poor surface condition at the tip region is caused by the imperfect polishing of the specimens. Due to the large size of pyramidal castings, the very tip region may not be polished sufficiently. This problem should be avoided in future work and require modification of how the pyramidal casting is sectioned before and supported during the mechanical polishing stage.

Table 5.3.2 The calculated values of n, A, and R^2 of all deduced stress-strain curves (tip region, 25˚C)

Casting date	AE44-2 alloys, tip region, 25˚C				Average value
July 25		n	A	R^2	
	Test 1	0.96	3.63E+03	0.91	$n_{average}$ = 1.03
	Test 2	1.11	6.04E+03	0.87	$A_{average}$ =4.84E+03
Oct. 29	Test 1	0.66	988.82	0.96	$n_{average}$ = 0.64
	Test 2	0.60	783.73	0.97	
	Test 3	0.65	936.07	0.88	$A_{average}$ =677.16
	Test 4	0.63	854.45	0.99	
Sep. 13	Test 1	0.86	3.91E+03	0.99	$n_{average}$ = 0.83
	Test 2	0.81	2.82E+03	0.96	
	Test 3	0.82	3.01E+03	0.96	$A_{average}$ =3.25E+03
Casting date	AE44-4 alloys, tip region, 25˚C				Average value
Oct. 23	Test 1	0.56	1.25E+03	0.87	$n_{average}$ = 0.63
	Test 2	0.52	1.03E+03	0.90	
	Test 3	0.60	1.42E+03	0.88	$A_{average}$ =1.84E+03
	Test 4	0.66	1.80E+03	0.86	
	Test 5	0.80	3.72E+03	0.80	

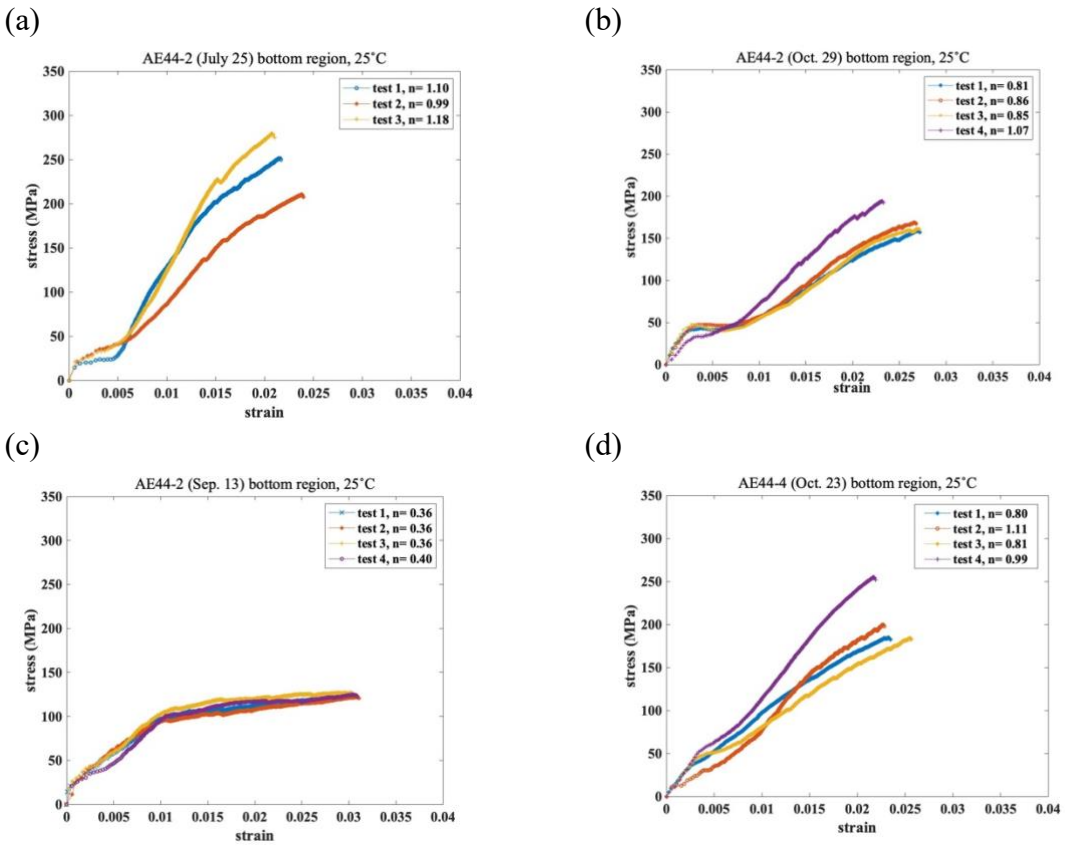

Figure 5.3.6 Indentation stress-strain curves of (a) July 25, (b) Oct. 29, (c) Sep. 13, (d) Oct. 23 pyramidal castings at bottom region and 25˚C.

From Fig. 5.3.4.a and 5.3.4.b, the stress-strain curves of July 25 and Oct. 29 castings are much lower than that of other AE44-2 castings. It seems that the tip region of July 25 and Oct. 29 are very soft. This unusual stress-strain response might be caused by the flaws of the surface. From Fig. 5.3.6, the deduced stress-strain curves of July 25 and Oct. 29 castings at the bottom region have higher strength than at the tip region. It might imply again that the quality of deduced stress-strain curves is greatly influenced by the condition of the surface where the indentation tests were performed. More spherical indentation tests need to be performed at the surface with good conditions and different grain sizes to understand the relationship between the grain size and stress-strain response without influenced by the surface condition.

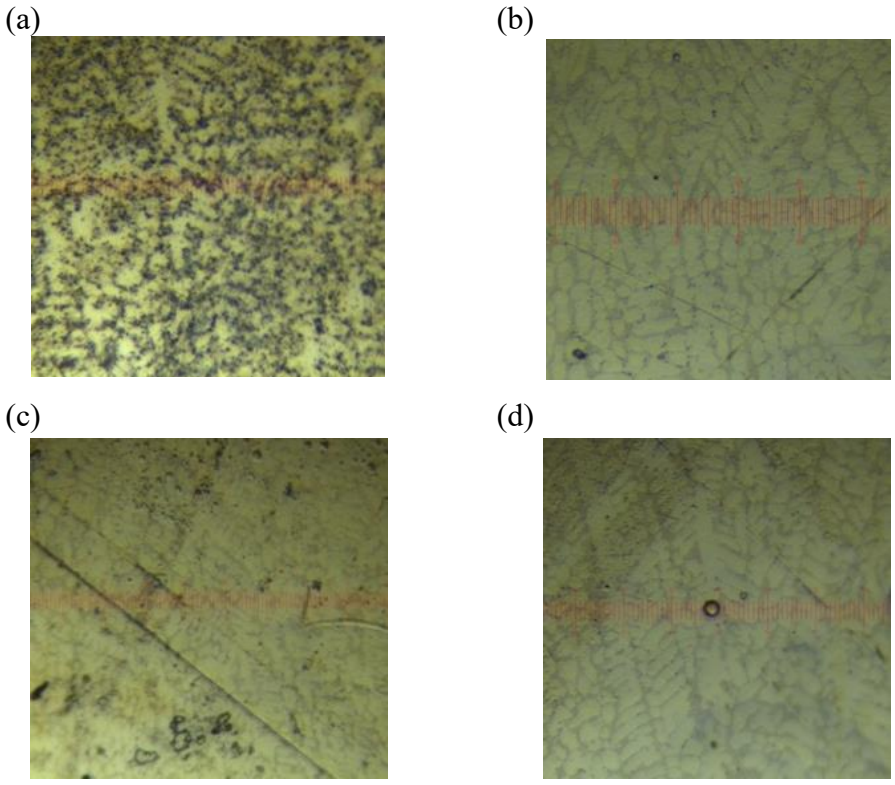

Figure 5.3.7 The optical microscopy pictures of (a) July 25 casting, (b) Oct. 29 casting, (c) Sep. 13 casting, (d) Oct. 23 casting at the bottom region.

Fig. 5.3.7 shows the surface condition at the bottom region of all specimens. Compared with the tip region, the surface condition of all specimens in this area is much better, and the grains can be seen clearly. On the contrary, the surface condition at the tip region is poor.

The stress-strain curves deduced from 25˚C spherical indentation tests are shown above. Form these stress-strain curves we can conclude that the effect of different RE additions do not have a significant effect on the stress-strain response of specimens. It is the surface condition that influence the deduced stress-strain curves.

Table 5.3.3 The calculated values of n, A, and R^2 of all deduced stress-strain curves (bottom region, 25˚C).

Casting date	AE44-2 alloys, bottom region, 25˚C				Average value
July 25		n	A	R^2	$n_{average} = 1.09$ $A_{average} = 1.87E+04$
	Test 1	1.10	1.84E+04	0.93	
	Test 2	0.99	8.82E+03	0.96	
	Test 3	1.18	2.89E+04	0.95	
Oct. 29	Test 1	0.81	2.82E+03	0.92	$n_{average} = 0.89$ $A_{average} = 5.22E+03$
	Test 2	0.86	3.76E+03	0.91	
	Test 3	0.85	3.39E+03	0.88	
	Test 4	1.07	1.09E+04	0.97	
Sep. 13	Test 1	0.36	454.55	0.91	$n_{average} = 0.37$ $A_{average} = 475.975$
	Test 2	0.36	434.81	0.90	
	Test 3	0.36	476.49	0.87	
	Test 4	0.40	538.05	0.83	
Casting date	AE44-4 alloys, bottom region, 25˚C				Average value
Oct. 23	Test 1	0.80	3.86E+03	0.99	$n_{average} = 0.93$ $A_{average} = 8.35E+03$
	Test 2	1.11	1.41E+04	0.97	
	Test 3	0.81	3.64E+03	0.99	
	Test 4	0.99	1.18E+04	0.99	

The effect of the elevated temperature on the stress-strain response of the specimens was studied by spherical indentation tests performed at 200˚C. The deduced stress-strain response of pyramidal castings at 200˚C is shown in Fig.5.3.8-5.3.10. The stress-strain curves of 200˚C tests are less smooth than that of the 25˚C tests. This phenomenon could imply that a different deformation mechanism is activated at elevated temperature. The fluctuations in the elevated temperature stress-strain curves might imply the twinning occurs during the deformation. For HCP metal, the twinning is an essential deformation mechanism.[74] Additionally, the dislocations in the specimens can move more easily at the elevated temperature. The jumping of dislocations may result in the fluctuations in the

curves.

Because the micro-indentation tester is highly sensitive to temperature change. Even the micro-indentation tester is placed in a chamber; the temperature in the chamber is less stable when the heaters are working. The fluctuation of the curves would unavoidably affect the accuracy of the values of n and A, but the R^2 value of the fitted result is still above 0.8. All the parameters of stress-strain curves are shown in Tables 5.3.4-5.3.6.

(a)

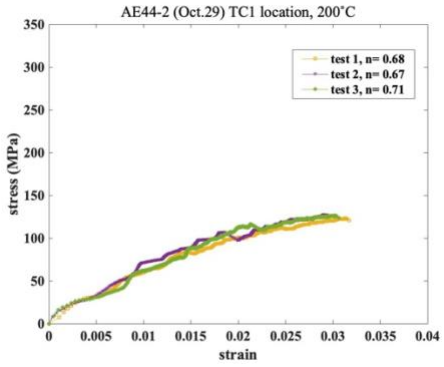

(b)

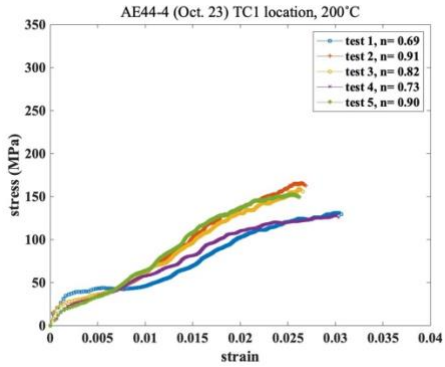

(c)

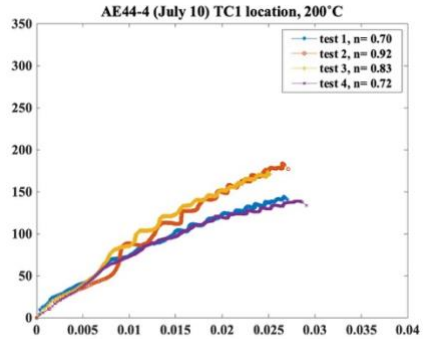

Figure 5.3.8 Indentation stress-strain curves of (a) Oct. 29 (AE44-2), (b) Oct. 23 (AE44-4), (c) July 10 (AE44-4) pyramidal castings at TC 1 location and 200˚C.

It can be seen that the mechanical strength of all specimens decreases more or less at 200˚C. At the TC 1 location of AE44-4 specimens (Oct. 23 and July 10), the stress-strain curves demonstrate two kinds of trends. The same behavior also occurs at the tip region of the AE44-4 specimens. As Fig 5.3.8.b shown the test 1 and test 4 on AE44-4 specimen (Oct. 23) have a flatter trend than other tests.

Table 5.3.4 The calculated values of n, A, and R^2 of all deduced stress-strain curves (TC 1 location, 200˚C).

Casting date	AE44-2 alloys, TC 1 location, 200˚C				Average value
Oct. 29		n	A	R^2	$n_{average}$ = 0.68 $A_{average}$ =1.46 E+03
	Test 1	0.68	1.37E+03	0.97	
	Test 2	0.67	1.39E+03	0.97	
	Test 3	0.71	1.63E+03	0.96	
Casting date	AE44-4 alloys, TC 1 location, 200˚C				Average value
Oct. 23	Test 1	0.69	1.47E+03	0.88	$n_{average}$ = 0.81 $A_{average}$ =3.09 E+03
	Test 2	0.91	4.67E+03	0.96	
	Test 3	0.82	3.04E+03	0.94	
	Test 4	0.73	1.80E+03	0.97	
	Test 5	0.90	4.49E+03	0.97	
July 10	Test 1	0.70	1.83E+03	0.99	$n_{average}$ = 0.79 $A_{average}$ =3.28 E+03
	Test 2	0.92	5.46E+03	0.97	
	Test 3	0.83	3.90E+03	0.98	
	Test 4	0.72	1.94E+03	0.97	

The stress-strain curves for the tip region are shown in Fig. 5.3.9. Compared with the results of 25˚C tests, the AE44-2 specimen demonstrates a reasonable stress-strain response at 200˚C. As mentioned previously all the specimens were repolished before the 200˚C indentation tests. The test 1 at the tip region of Oct. 23 specimen illustrates that the stress suddenly drops at the ε=0.0225, this might be caused by defects in the specimen. Only two stress-strain curves obtained for July 10 specimens and these two curves have divergence at $\varepsilon > 0.007$.

(a)

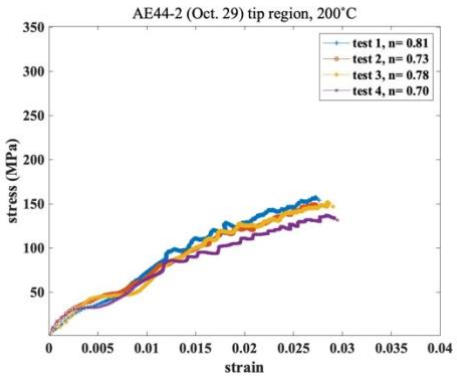

(b)

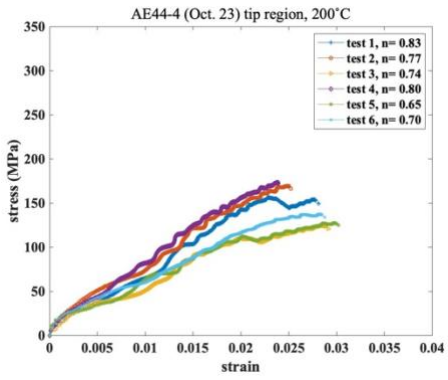

(c)

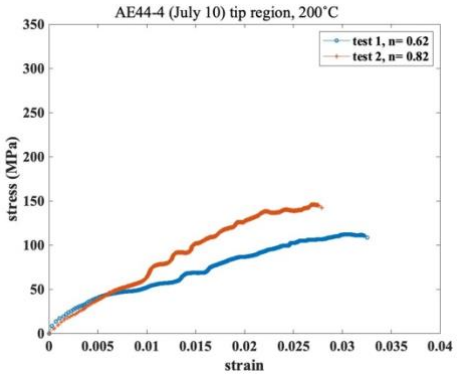

Figure 5.3.9 Indentation stress-strain curves of (a) Oct. 29, (b) Oct. 23, (c) July 10 pyramidal castings at tip region and 200˚C.

Table 5.3.5 The calculated values of n, A, and R^2 of all deduced stress-strain curves (tip region, 200˚C).

Casting date	AE44-2 alloys, tip region, 200˚C				Average value
Oct. 29		n	A	R^2	$n_{average}$ = 0.75 $A_{average}$ =2.31 E+03
	Test 1	0.81	2.98E+03	0.98	
	Test 2	0.73	2.06E+03	0.99	
	Test 3	0.78	2.54E+03	0.96	
	Test 4	0.70	1.65E+03	0.97	
Casting date	AE44-4 alloys, tip region, 200˚C				Average value
Oct. 23	Test 1	0.83	3.42E+03	0.95	$n_{average}$ = 0.75 $A_{average}$ =2.46 E+03
	Test 2	0.77	2.92E+03	0.98	
	Test 3	0.74	1.82E+03	0.96	
	Test 4	0.80	3.55E+03	0.98	
	Test 5	0.65	1.31E+03	0.95	
	Test 6	0.70	1.73E+03	0.97	
July 10	Test 1	0.62	964.2043	0.98	$n_{average}$ = 0.72 $A_{average}$ =1.98 E+03
	Test 2	0.82	2.99E+03	0.98	

(a)

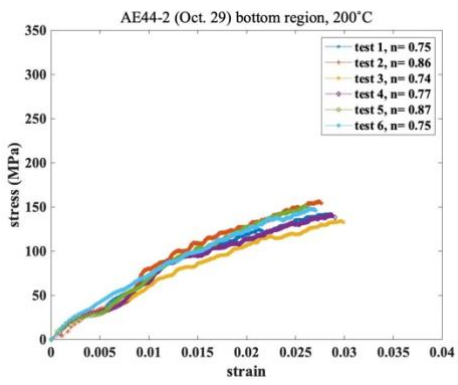

(b)

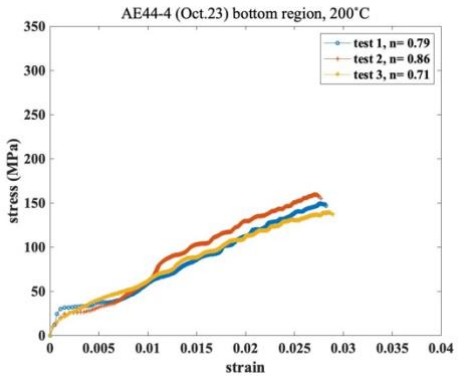

Figure 5.3.10 Indentation stress-strain curves of (a) Oct. 29, (b) Oct. 23 pyramidal castings at the bottom region, and 200˚C.

Table 5.3.6 The calculated values of n, A, and R^2 of all deduced stress-strain curves (bottom region, 200˚C).

Casting date	AE44-2 alloys, bottom region, 200˚C				Average value
Oct. 29th		n	A	R^2	$n_{average}$ = 0.79 $A_{average}$ =2.69 E+03
	Test 1	0.75	2.19E+03	0.98	
	Test 2	0.86	3.73E+03	0.94	
	Test 3	0.74	1.87E+03	0.98	
	Test 4	0.77	2.25E+03	0.96	
	Test 5	0.87	3.82E+03	0.98	
	Test 6	0.75	2.29E+03	0.99	
Casting date	AE44-4 alloys, bottom region, 200˚C				Average value
Oct. 23rd	Test 1	0.79	2.44E+03	0.94	$n_{average}$ = 0.78 $A_{average}$ =2.59 E+03
	Test 2	0.86	3.57E+03	0.96	
	Test 3	0.71	1.77E+03	0.98	

The results of spherical micro-indentation tests at 200˚C show that most of the calculated strain hardening exponents of both AE44-2 and AE44-4 specimens decrease. The total

average stress of elevated temperature tests is also lower than that of room temperature tests, although the elevated temperature tests have a higher stress level for some specimens at the tip region. This result consistent with the fact that all specimens are softer at elevated temperature than at room temperature.

According to the n valves in the Tables above, at 25˚C, the average strain hardening exponent of the AE44-2 specimens at the tip region is 0.83, while it is 0.78 at the bottom region. For the AE44-4 specimen, the strain hardening exponent is 0.63 at the tip region and 0.93 at the bottom region. It is clear that the calculated strain hardening exponents are relatively high. This result might result from the calculation method of strain hardening exponent used in this analytic approach. As mentioned before, we assume that the stress-strain response of AE44-2 and AE44-4 alloys follow the equation 5.3.1. However, this power-law form only valid for the plastic deformation range (when the applied stress is larger than the yield stress). While, in this study the n value is obtained by fitting the whole log(σ)-log(ε) curve, including the initial part of the log(σ)-log(ε) curve ($\sigma < \sigma_y$), where the stress and strain do not follow the power-law equation. The error caused by this fitting method is shown in Fig. 5.3.11.

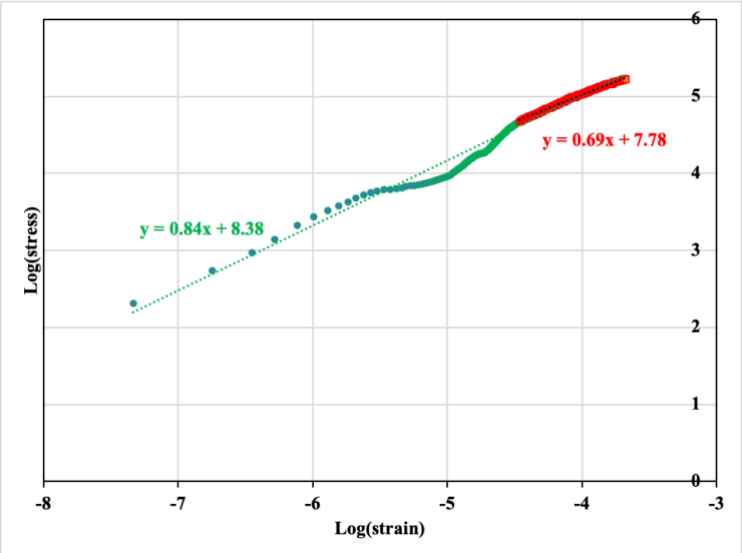

Figure 5.3.11 Different n value fitted by the whole curve (green line) and partial curve (red line)

From Fig. 5.3.11, the different n values can be seen. The bigger n value (n = 0.84) is obtained by fitting the entire log(σ)-log(ε) curve, which is used in this study, while the smaller n value (n = 0.69) is obtained by fitting the curve excluding the first 150 data points. It can be seen that the initial data point can significantly affect the n value and result in a higher n value. Additionally, the higher n value is more likely to occur in the stress-strain curve, which has a small flat stage at the small strain. This suggests that the high n value might be resulted from the deformation mechanism. It should be noted that the HCP metal is anisotropic, while the analytic approach is proposed based on the isotropic material. Finally, this phenomenon could result from the fact that at the initial stage of the indentation tests, the indentation depth is very small (< 1μm) and only a few grains deform, resulting in a flow stress similar to a single or bi-crystal sample. With the increase of indentation depth, more grains begin to deform, and the effect of grain boundaries becomes obvious, resulting in the shape of the deduced stress-strain curves. All factors mentioned above could result the error in the calculated n value. In order to eliminate the effect of initial unstable stress-strain response on the fitted n value, The analytic approach needs to be improved and the deformation mechanism of AE44-2 and AE44-4 needs to be fully understood.

Above are all the results of spherical micro-indentation tests. Although the relatively high R^2 value provides confidence to the fitted values of strain hardening exponent and the pre-exponent term, the fluctuation range of these parameters is still large. The reasons for this result, could be attributed to that: Firstly, the spherical micro-indentation tests involve only a very small area of the specimen. As a result, one stress-strain curve only represents the mechanical response of a few grains under the indenter. Secondly, during the indentation tests, the indenter might leave an indentation on a surface flaw. Thirdly, the values of n and A have errors caused by the analytical approach.

In order to illustrate the results more clearly, the average value of n and A are listed in Table 5.3.7. these parameters are then put into the equation $\sigma = A\varepsilon^n$ to create the characteristic curve for each alloy at different temperatures. These curves are then compared with the

stress-strain curves obtained from the tensile tests to study the differences caused by these two test methods.

Table 5.3.7 The average stress (ε = 0.01, 0.02, 0.025, 0.03) for AE44-2 and AE44-4 specimens at 25˚C and 200˚C.

Alloy	Temperature	$n_{average}$	$A_{average}$ (MPa)	$\sigma_{\varepsilon=0.01}$ (MPa)	$\sigma_{\varepsilon=0.02}$ (MPa)	$\sigma_{\varepsilon=0.025}$ (MPa)	$\sigma_{\varepsilon=0.03}$ (MPa)
AE44-2	25˚C	0.73	4.65E+03	133.92	228.42	271.26	312.16
	200˚C	0.75	2.29E+03	70.80	119.47	141.40	162.26
AE44-4	25˚C	0.79	4.64E+03	124.77	215.02	256.20	295.63
	200˚C	0.78	2.75E+03	77.08	132.01	156.97	180.83

5.4 Tensile tests of AE44-2 and AE44-4 specimens at 25˚C and 200˚C

As introduced in chapter 3, the tensile tests were performed on both AE44-2 and AE44-4 alloys at 25˚C and 200˚C to study the mechanical properties of these two alloys. As a reference, the tensile stress-strain curves of AE44 alloy provided by Meridian Magnesium is also present in this section. The average stress-strain curves generated by the analytical approach are also presented and discussed.

The stress-strain curves of AE44-2 and AE44-4 specimens are shown in Fig 5.41 and 5.4.2. The black curves in Fig. 5.4.1 and 5.4.2 are generated using Meridian's data, while the colored curves are obtained by the tensile tests, which have been introduced in the previous chapter. At 25˚C, three AE44-4 and two AE44-2 specimens were tested, but the first two tests on AE44-4 specimens were failed (purple and yellow lines in Fig 4.6.1).

As shown in Fig. 5.4.1, the curves show good repeatability. The strength of AE44-4 specimens is slightly higher than that of AE44-2 specimens at 25˚C and 200˚C. This difference is so small that these two kinds of alloys have nearly the same tensile strength.

The tensile strength of AE44-2 and AE44-4 specimens lose about 40% strength when heated to 200˚C. Compared with Meridian's tensile test curves, our tensile stress-strain curves are flatter. This might be the result of the method used to determine the strain (we used cross-head displacement while the Meridian tests may have used a resistance strain gauge attached directly to the specimen gauge length, or by possible slippage occurring between the specimen and the grips during our tensile tests).

Figures 5.4.1 and 5.4.2 also show the comparison between stress-strain curves obtained by spherical indentation, along with its associated analytic approach (dashed lines) and the tensile tests. When the strain is less than $\varepsilon = 0.015$, the deduced stress-strain curves are close to the curves of the tensile tests. However, at the large strain ($\varepsilon > 0.02$), the deviation of the deduced curves and the tensile stress-strain curves becomes large. The deduced stress-strain curves increase quickly and exceed the Meridian 's curves when the strain is larger than $\varepsilon = 0.015$. This property of the deduced stress-strain curves occurs at both 25˚C and 200˚C. The difference between the deduced stress-strain curves and the tensile stress-strain curves is primarily the result of the high calculated strain hardening exponent. Table. 5.4.1 compares the strain hardening exponents obtained by tensile tests and indentation tests. The elevated temperature, 200ºC, lowers the strain hardening exponent and makes the spherical indentation analytical stress-strain curves closer to the tensile curves. Although the deduced stress-strain curves show that at 25˚C, the strength of AE44-2 alloy is slightly higher than that of AE44-4 alloy, while at the 200˚C AE44-4 alloy is stronger than AE44-2, the difference in the mechanical strength of both alloys is small at both temperatures. This is consistent with the tensile test results.

Table 5.4.1 shows that the strain hardening exponents of the stress-strain curves deduced from indentation tests are very high compared with that of the tensile stress-strain curves. The high n value results in the steep slope of the deduced curves. The reason for the high n value has been discussed in section 5.3. While it should note that stress was applied in different ways in tensile tests and indentation tests, the indentation test is more like a

compression test.

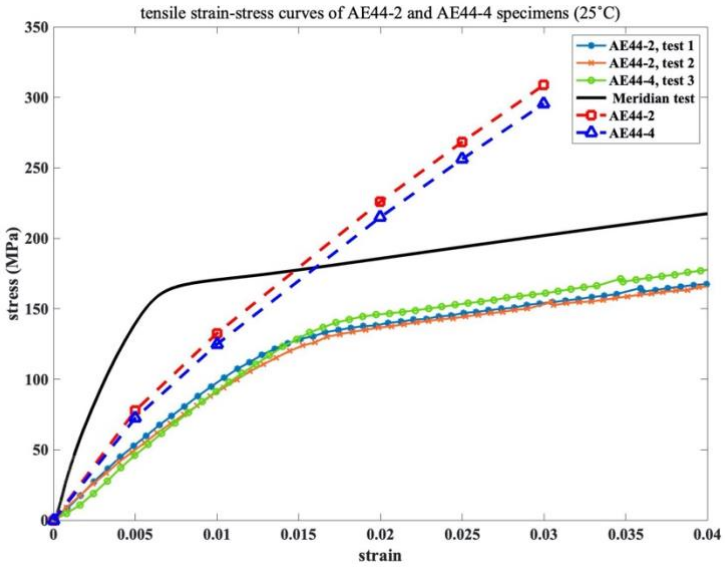

Figure 5.4.1 Comparison of stress-strain curves measured by the tensile tests (including Meridian 's result) and by the spherical micro-indentation tests (25˚C).

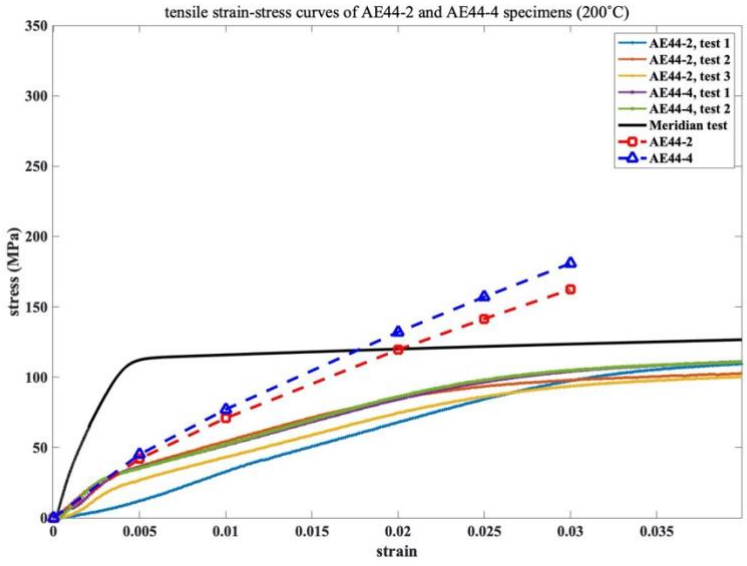

Figure 5.4.2 Comparison of stress-strain curves measured by the tensile tests (including Meridian's result) and by the spherical micro-indentation tests (at 200˚C).

Table 5.4.1 Comparison of strain hardening exponent obtained by tensile tests, Meridian 's data, and spherical micro-indentation tests.

Method	temperature	alloys	Strain hardening exponent
Tensile tests	25˚C	AE44-2	0.32
		AE44-4	0.35
	200˚C	AE44-2	0.22
		AE44-4	0.14
Meridian ’s data	25˚C	AE44	0.20
	200˚C	AE44	0.07
Spherical micro-indentation tests	25˚C	AE44-2	0.77
		AE44-4	0.79
	200˚C	AE44-2	0.75
		AE44-4	0.78

5.5 The dependence of stress-strain response upon grain size

In the previous section, the hardness of HPDC panels varies with the grain size. In order to study the effect of grain size on the stress-strain response of AE44-2 and AE44-4 alloys, the multiple load-unload spherical indentation tests were performed on different grain size regions of the pyramidal specimens and the test panels. In this study the grain size under the indentation is defined as effective grain size d_{eff}. The edge of spherical indentation was highlighted by a black circle (as Fig. 5.5.1 shown) to measure the grain size around the indentation. Then using the equation 5.5.1 to calculate the local effective grain size d_{eff}.

$$d_{eff} = \frac{2\pi R}{N} \tag{5.5.1}$$

Where the N is the number of the grain boundaries intercepting the black line, and the R is the radius of the indentation. The value of d_{eff} decreases with increases of N.

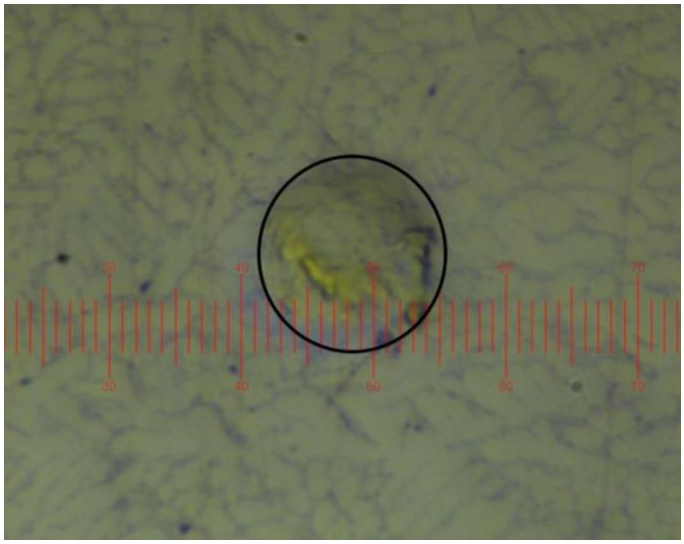

Figure 5.5.1 The optical microscope image of an indentation highlighted by a black circle.

The effective grain size of every indentation is then related to the calculated strain hardening exponent, as shown in Fig. 5.5.2. A negative correlation between strain hardening exponent and the grain size, the n value decreases with the grain size increases. This trend can be seen in both AE44-2 and AE44-4 alloys at 25˚C and 200˚C. The increase of temperature has no obvious effect on the slope of n-d_{eff}. While it is the RE additions that affects the slope. The slope of AE44-4 alloys is about three times larger than that of AE44-2 alloy.

The effect of grain size on the yield stress follows the Hall-Petch law, as introduced in section 2.6. In this study, the relationship between effective grain size and stress at small strain (ε = 0.005) was studied. Fig. 5.5.3 shows the $\sigma_{\varepsilon=0.005}$-$d_{eff}$ scatter plots of AE44-2 and AE44-4 alloys. It should be noted that the effective grain size and stress at small strain

can only show the Hall-Petch law of the specimens approximately.

(a)

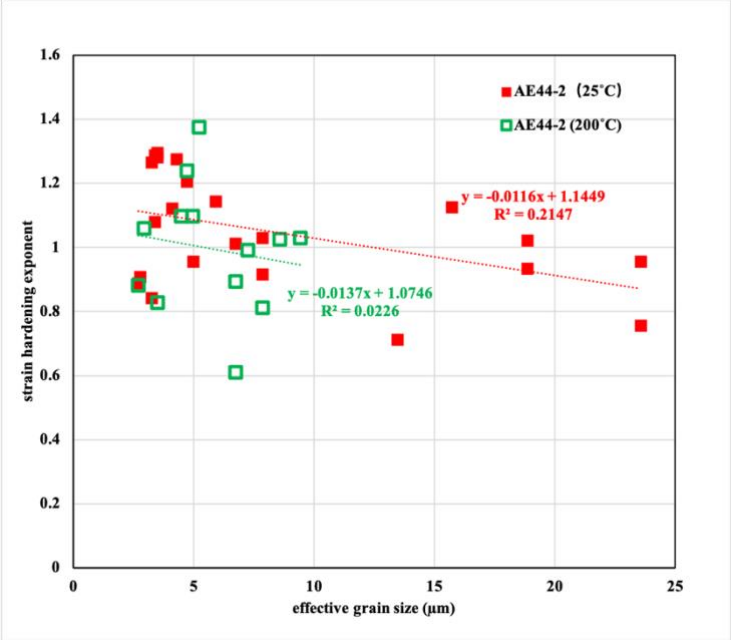

(b)

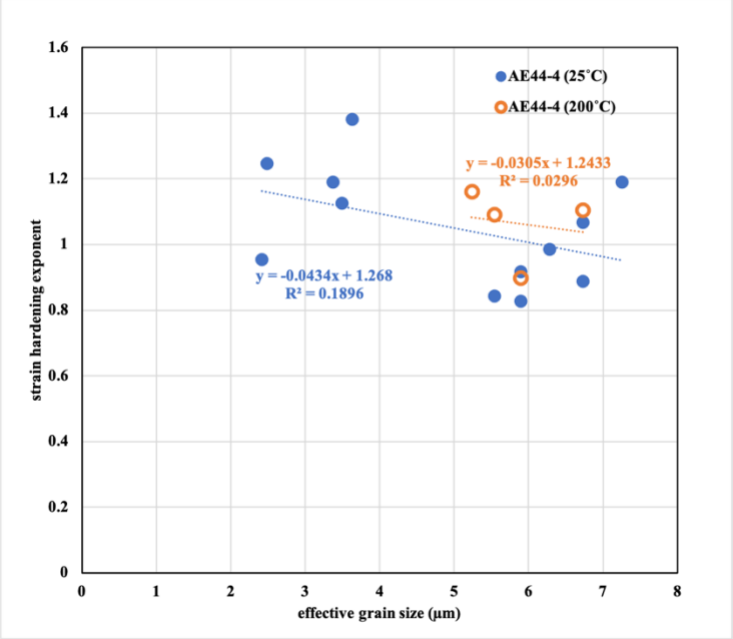

Figure 5.5.2 Strain hardening exponent-effective grain size (a) AE44-2 specimen, (b) AE44-4 specimen, at 25˚C at 200˚C.

(a)

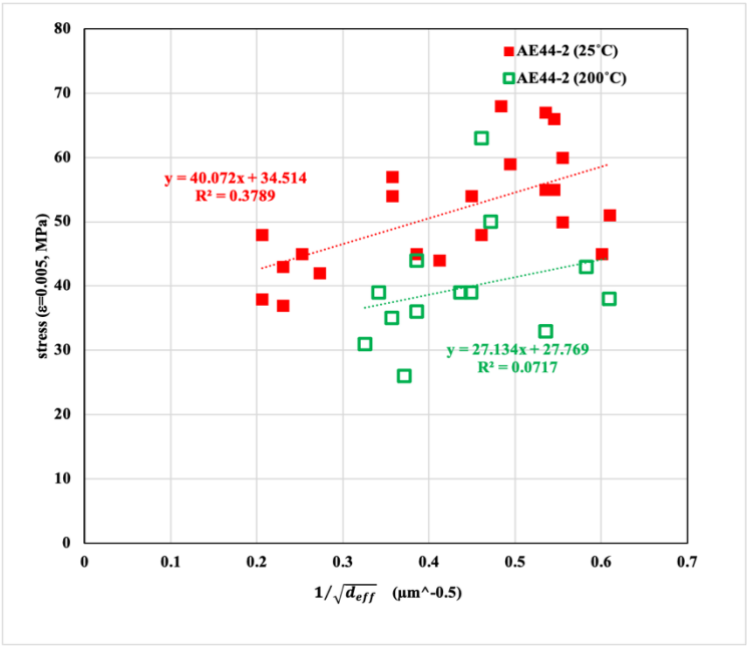

(b)

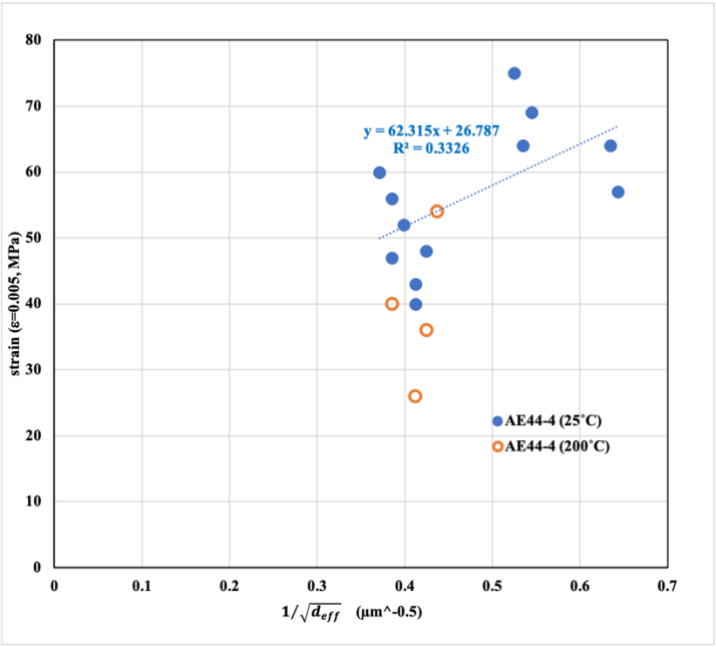

Figure 5.5.3 $\sigma_{\varepsilon=0.005}$-$d_{eff}$ plots of (a) AE44-2, (b) AE44-4 at 25°C and 200°C.

From Fig. 5.5.3, the $\sigma_{\varepsilon=0.005}$ of both AE44-2 and AE44-4 alloys have a positive correlation with effective grain size. This kind of relationship is similar to the Hall-Petch law. However, the Hall-Petch slope of the specimens is smaller than the Hall-Petch slope of similar alloys. Sharifi et al. studied the Hall-Petch slope of AE44 alloy and found that the Hall-Petch slope, for micro-indentation testing, is 178 (MPa·μm$^{0.5}$)[16], while in this study, the Hall-Petch slope of the specimens is much smaller than Sharifi's result except

AE44-4 alloy at 200˚C. This could be caused by the grain size used in our calculation is not accurate. The high value of the Hall-Petch slope of AE44-4 specimen at 200˚C could result from the small data points. If more data points can be shown in the scatter plot, the fitted result could be more accurate. Although the error exists in this method, this section still reveals that the grain size can affect the stress-strain response of AE44-2 and AE44-4 alloys. The results of this section show that the flow stress of AE44-2 and AE44-4 alloys increase with the decrease of grain size at 25˚C and 200˚C.

5.6 Creep behavior of AE44-2 and AE44-4 alloys

The creep resistance of AE44-2 and AE44-4 alloys is an important mechanical property because the poor creep resistance of traditional Mg-Al alloys is the main restriction of the application of this kind of alloys. As introduced in chapter 2, the RE elements can improve the creep resistance of Mg-Al alloys. In this section, the creep behavior of AE44-2 and AE44-4 specimens will be discussed to see whether the grain size and the chemical composition would affect the creep resistance of the specimens. The constant-load indentation creep tests (20mN) were performed by Alemnis indentation tester at 25˚C and 200˚C to study the creep resistance of AE44-2 and AE44-4 alloys at elevated temperature. Fig. 5.6.1 show the depth-time curves of all specimens. The creep strain rate $\dot{\epsilon}_{creep}$ of every test was calculated from the indentation depth-time curves. The results are shown in Fig 5.6.4. It should be noted that the Alemnis indentation tester is very sensitive to the vibration, so the resulting curves, especially the $\dot{\epsilon}_{creep}$- t curves, fluctuate. During the creep tests, the Alemnis indentation tester records 400 data points per second. To simplify the calculation and reduce noise, the average value of displacement was calculated for every minute, which means that each data used in the curves is an average value of 400*60 data points.

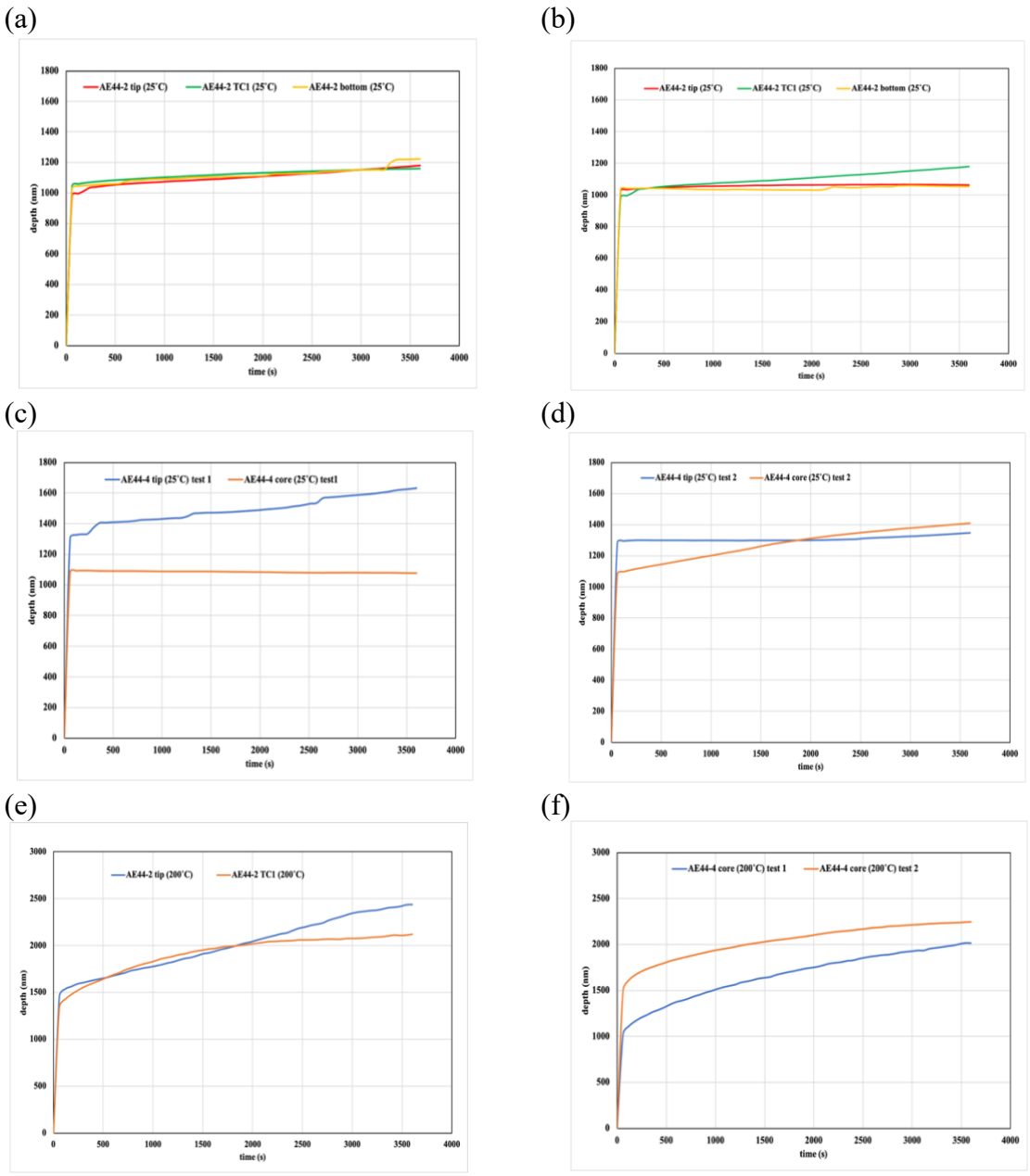

Figure 5.6.1 The depth-time curves of (a) and (b) AE44-2 specimen at tip-, TC 1-, and bottom- regions, at 25˚C, (c) and (d) AE44-4 specimen at tip-, core- regions, at 25˚C, (e) AE44-2 specimen at tip- and TC 1- regions, at 200˚C, (f) AE44-4 specimen at core region, at 200˚C.

The constant load applied to the specimens was set as 20 mN, so the indentation creep stress decreases with time. Fig. 5.6.2 demonstrates a schematic picture of the Berkovich indentation test, as this figure shows the total displacement (h), which is recorded by the

tester, is the summation of h_c and h_s, where the h_c is the contact depth, and h_s is the displacement of the surface sinking around the indenter. According to Oliver and Pharr, the contact area (A_c) between the indenter and the surface of the specimen is a function of contact depth. In this section, the area function is shown below (equation 5.6.1)

$$A_c = 1.227064 \times 10^2 \times {h_c}^2 - 9.319401 \times 10^{-5} \times h_c + 7.901876 \times 10^{-8} \times {h_c}^{\frac{1}{2}} - 9.076759 \times 10^{-10} \times {h_c}^{1/4} \quad (5.6.1)$$

Where the unit h_c is the meter (m), it should be noted that in this study we ignore the sink in effect and assume that the total displacement equals contact depth to simplify the calculation.

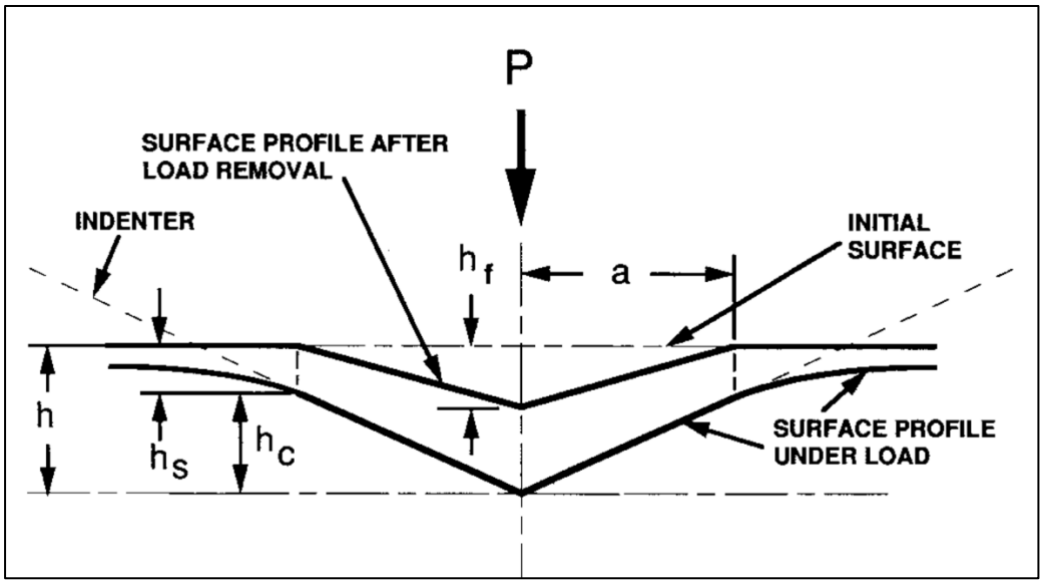

Figure 5.6.2 The schematic picture of the Berkovich indentation test.[60]

The indentation creep stress is calculated for every indentation. Fig. 5.6.3 shows the change of indentation creep stress of the tests at 25˚C and 200˚C. Because the contact area increases with the increase of the displacement of the indenter, the stress applied to the specimen will reduce during the creep test.

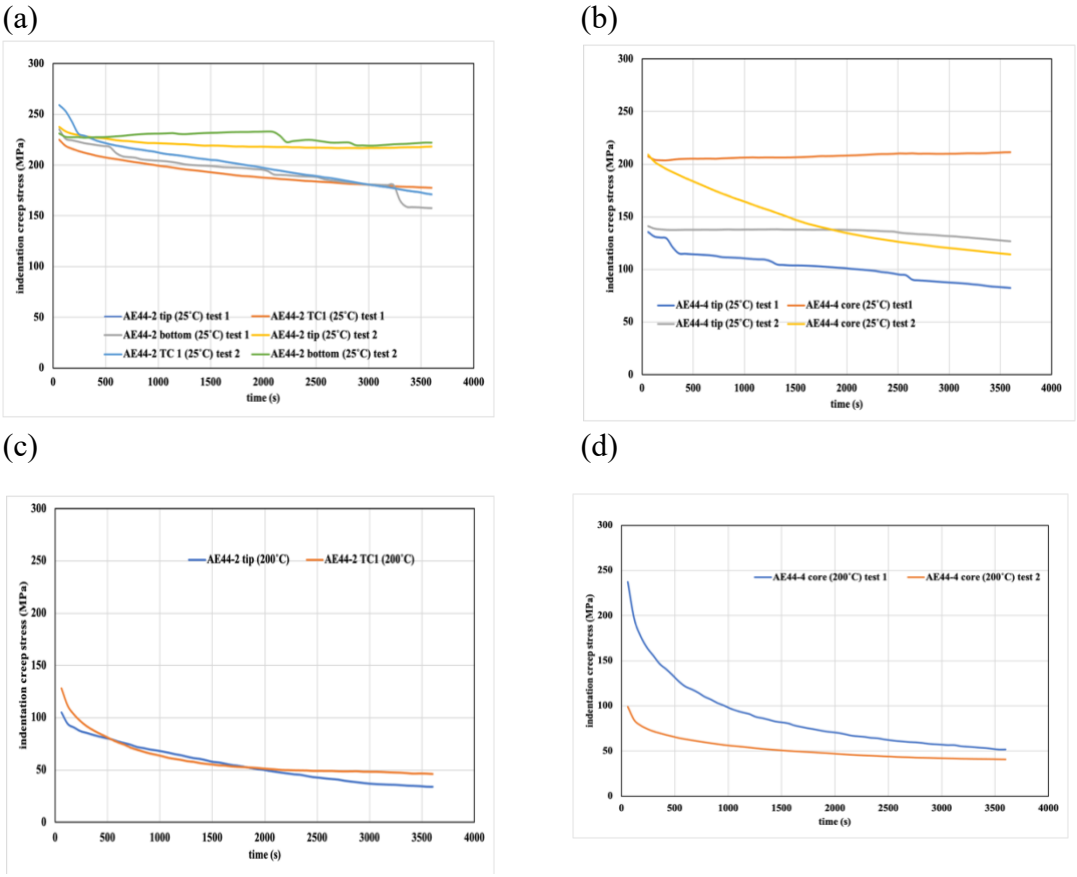

Figure 5.6.3 The dependence of indentation creep stress on the time (a) AE44-2 at 25˚C, (b) AE44-4 at 25˚C, (c) AE44-2 at 200˚C, (d) AE44-4 at 200˚C.

As shown in Fig. 5.6.3, for most tests the stress decrease with time, and the reduction of stress over 1 hour is about 10%~80%. While the stress of the 25˚C test on the AE44-4 core region (Fig. 5.6.3.b, orange line) does not reduce with time. This might be caused by the experimental error. For the 200˚C indentation creep tests, the reduction of stress is larger than the 25˚C tests in most cases. It is easy to understand because the specimens are "softer" at 200˚C than 25˚C, so the indentation creep stress reduces more quickly at 200˚C.

The creep strain rate is an important parameter to evaluate the creep resistance of the specimens. In this study, the creep strain rate was calculated by equation 5.6.2. where t is time. Fig. 5.6.4 shows the $\dot{\epsilon}_{creep}$-t curves of all indentation creep tests.

$$\dot{\epsilon}_{creep} = \frac{\left(\frac{dh}{dt}\right)}{h} \tag{5.6.2}$$

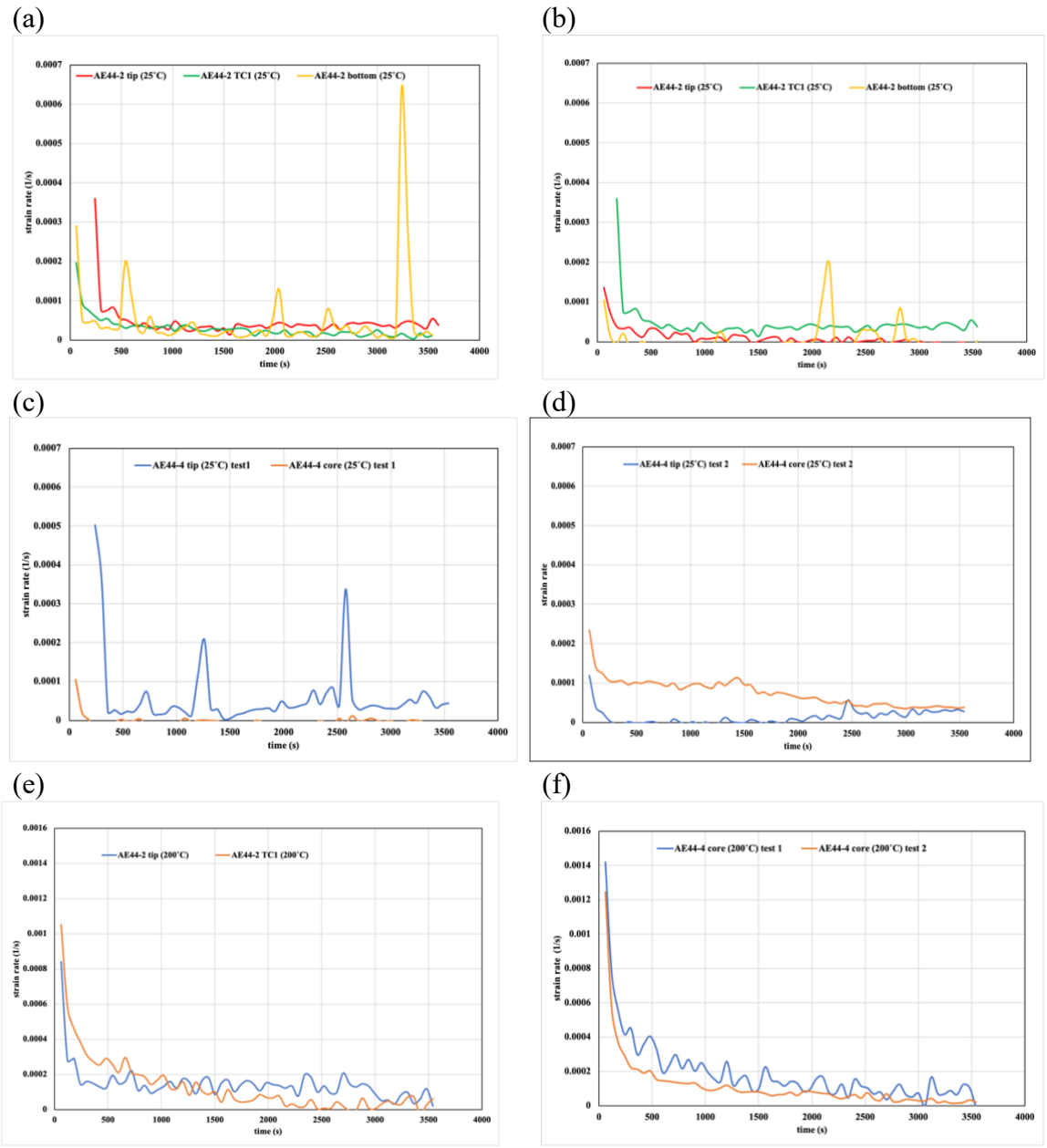

Figure 5.6.4 The creep strain rate-time curves of (a) and (b) AE44-2 specimen at tip-, TC 1-, and bottom- regions, at 25˚C, (c) and (d) AE44-4 specimen at tip-, core- regions, at 25˚C, (e) AE44-2 specimen at tip- and TC 1- regions, at 200˚C, (f) AE44-4 specimen at core region, at 200˚C.

From Fig. 5.6.4, it can be seen that the creep strain rate does not have a strong dependence on the grain size. The grain size of pyramidal castings varies from the tip region to the bottom region (section 4.3), but the creep strain rate does not appear the same behavior. This could be attributed to the difference in the grain size under the indenter is not big enough to cause a noticeable difference in the creep strain rate of every indentation test. In some plots, the creep strain rate has a negative value, which is unusual. For example, Fig. 5.6.4.b, the creep rate of AE44-2 specimen at the tip and bottom regions drop below 0 at some points. The same situation happens to other tests. This problem might be the result of vibration from the environment. As mentioned before, the Alemnis indentation tester is very sensitive to vibration. Although the average values are used in these curves, huge fluctuations still exist in the $\dot{\epsilon}_{creep}$-t curves. In Fig. 5.6.4.a, Fig. 5.6.4.b, and Fig. 5.6.4.c, the creep strain rate fluctuates in a large range. These fluctuations can also be seen in the corresponding depth-time curves. For example, the creep rate of AE44-2 specimens at the bottom region suddenly increases at about 3250 seconds. Meanwhile, a large jump can be seen in the depth-time curve of this indentation creep test. Various reasons can cause the vibration of depth-time curves obtained by the Alemnis indentation tester in this study, For example, different dislocation slip systems might occur during the tests. The activation energy of these slip systems is different. The sudden activation of other slip systems could result in fluctuations in the curves. While it should be noted that at 25˚C, the prismatic and pyramidal slip system is hard to activate. The small vibration of the temperature would be another reason for the fluctuations in the depth-time curves.

and this problem has not been solved yet. In order to compare the creep resistance of AE44-2 and AE44-4 alloys, the average creep strain rate is calculated. Since the creep strain rate of all tests tends to be relatively stable after 500 seconds, the average value of creep strain rate after 500 seconds is used to compare the creep resistance of AE44-2 and AE44-4 alloys. (hereafter, the average creep strain rate will be named as steady-state creep rate) Fig. 5.6.5 shows the steady-state creep rate of each test.

From Fig. 5.6.5, a negative creep strain rate can be seen. For AE44-4 at the core region, this result might result from the experimental error. The depth-time curve of this indentation test (Fig. 5.6.1.c) shows that the indentation displacement reduces with time. This behavior is unusual and might be caused by the thermal drift. Except for this unusual result, the difference in steady-state creep rate of these tests can be seen that the steady-state creep rate of both AE44-2 and AE44-4 specimens at 200˚C are higher than at 25 ˚C, the steady-state creep rate of AE44-2 alloy at 200˚C is 1.03E-04 (1/s), while it is only 2.48E-05 (1/s) at 25˚C. For AE44-4 alloy, the steady-state creep rate is 1.00E-04 (1/s) at 200˚C and 4.21E-05 at 25 ˚C. From 25˚C to 200˚C, the steady-state creep rate increases 315% for AE44-2 and 137% for AE44-4 alloy. The number of 200˚C creep tests is not sufficient enough to support the conclusion that the AE44-4 alloy tends to remain the creep resistance at 200˚C. However, it is clear that the creep resistance of AE44-2 and AE44-4 reduces quickly at 200˚C.

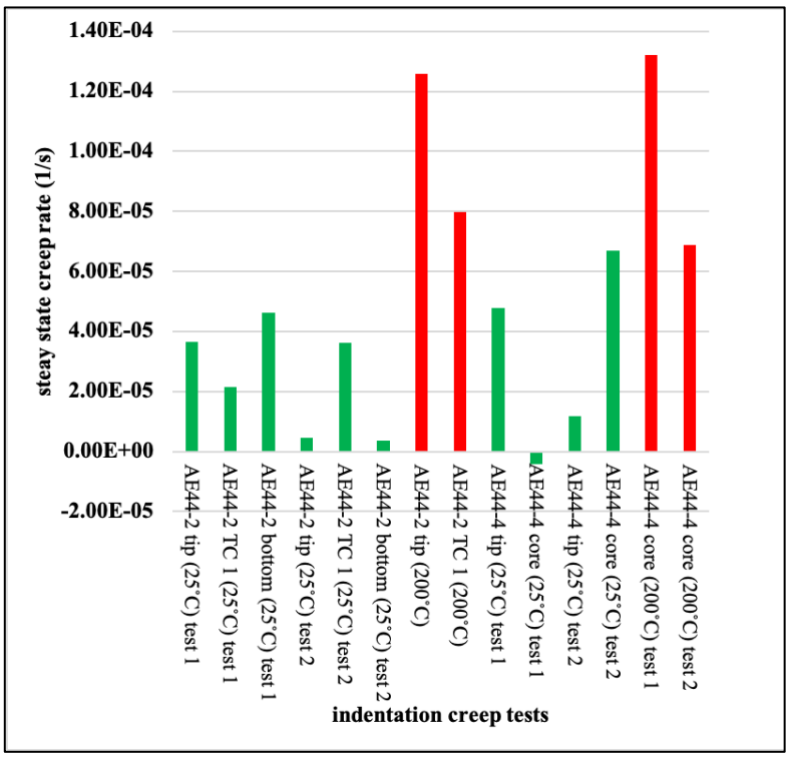

Figure 5.6.5 The steady-state creep rate of the indentation creep tests.

This section compares the steady-state creep rate of AE44-2 and AE44-4 alloys at 25˚C and 200˚C and found that the AE44-2 alloy has a higher creep resistance at 25˚C than AE44-4 alloy, but the creep rate of AE44-2 alloy is increased relative to that of the AE44-4 alloy when the test temperature is 200˚C.

In this chapter, the relationship of Vickers hardness and the grain size was studied, and two kinds of trends were found for AE44-2 and AE44-4 alloys. The effect of cooling rate on the grain size was also discussed for the pyramidal castings. The spherical micro-indentation tests were analyzed by a new iterative algorithm to deduce the stress-strain response of AE44-2 and AE44-4 specimens. We related the deduced stress-strain response of the specimens to the grain size and found the Hall-Petch law of AE44-2 and AE44-4 alloys at 25˚C and 200˚C. Additionally, by comparing the stress-strain curves obtained by the tensile tests and indentation tests, we found that the analytical approach using in this study could predict the stress-strain response in a certain strain range but the high value of strain hardening exponent results in a large deviation at large strain. The reason for this problem has been discussed in this chapter. The creep behavior of AE44-2 and AE44-4 alloys was also studied, and the different creep resistance properties were discussed.

Chapter 6

6 Conclusions and Future Work

The object of this study is adopting spherical micro-indentation tests and constant load Berkovich indentation tests to study the micro-scale mechanical properties of AE44-2 and AE44-4 alloys at 25˚C and 200˚C, and correlating the microstructure, especially the grain size, to the mechanical properties. Additionally, compare the results of tensile tests and indentation tests to examine the new analytical approach developed in this study.

6.1 Conclusions

(1) The difference between AE44-2 and AE44-4 alloys is the chemical composition. By X-Ray diffraction analysis, it can be confirmed that the AE44-2 alloy contains only Ce and La, while AE44-4 alloy contains Ce, La, Pr, and Nd.

(2) In this study, two kinds of specimens were used, the pyramidal specimens and the panels. For pyramidal specimens, the grain size varies from the tip to the bottom. Due to the special geometrical structure, the pyramidal castings have various cooling rates during the solidification. The tip region has the smallest grain size (5.60~7.90μm and 3.30μm for AE44-4 and AE44-2 specimens, respectively), while the bottom region has the largest grain size (26.70μm and 11.20μm for AE44-4 and AE44-2 specimens, respectively). For the panels, the grain size increases from the skin region to the core region.

(3) The hardness of both AE44-2 and AE44-4 HPDC panels show a dependence on the grain size, but two opposite trends appear in the AE44-2 and AE44-4 panels. For the AE44-2 panel, the hardness decreases with the increase of grain size, while for the AE44-4 panel, the hardness increases with the increase of grain size. These different

results could be the result of insufficient data points. The variation of grain size is relatively too small to reveal the real relationship between the hardness and grain size of the specimens.

(4) The cooling rate effect during the solidification on the microstructure of pyramidal castings was studied, and a linear function was developed between the grain size and the inverse square root of the average cooling rate (equation 5.2.2). Although this equation still has a significant error, only five data points were used to fit this equation. It still can reveal the relationship between the cooling rate and grain size for the AE44-2 and AE44-4 alloys.

(5) The deduced stress-strain curves from indentation tests show that the difference of mechanical strength between the AE44-2 and AE44-4 is small. Although at 200˚C the strength of AE44-2 alloy decreases, the AE44-2 alloy still has 90% strength of AE44-4 alloy. Compared with the strength at 25˚C, AE44-2 alloy loses 50% strength while the AE44-4 alloy loses about 60% strength at 200˚C.

(6) The strain hardening exponent of AE44-2 and AE44-4 alloys have a negative correlation with the grain size. The quasi-Hall-Petch slope is 40.07 ($MPa\bullet\mu m^{0.5}$) at 25˚C and 27.13 ($MPa\bullet\mu m^{0.5}$) at 200˚C for AE44-2 alloy, 62.32 ($MPa\bullet\mu m^{0.5}$) at 25˚C for AE44-4. The quasi-Hall-Petch slope in this study is calculated via the effective grain size and stress at $\varepsilon = 0.005$ strain, so the value of the quasi-Hall-Petch slope is different from the true Hall-Petch slope of these alloys.

(7) Compared with the tensile tests, the deduced stress-strain curves have a high value of strain hardening exponents. Additionally the stress-strain curves are not smooth but sometimes flat and, especially at 200˚C appear to be unstable (have jumps). These phenomena might indicate the complex deformation mechanisms, which probably involve both dislocations slip and twinning, occurring in these alloys especially at 200˚C. Besides, the initial data points of stress-strain curves can greatly improve the n value. However, the reason for these phenomena has not been fully understood yet.

(8) The constant load indentation tests show that the steady-state creep rate of AE44-2 and

AE44-4 increases with temperature. The creep resistance of AE44-2 are similar with that of AE44-4 at 25 ˚C but the steady-state creep rate increases rapidly when the temperature increases to 200˚C. both AE44-2 and AE44-4 alloys lose a lot of creep resistance at elevated temperature.

(9) In this study, we have some new findings: (i) a newly developed analytical technique to deduce the stress-strain response of die-cast multi-phase AE alloys. This analytical technique is based on the theories of Hill, Tabor, Matthew and Tirupataiah and relates the indentation stress and strain to the strain hardening exponent. through an iterative algorithm the stress-strain curves can calculated form the spherical indentation tests. The local stress-strain curves at 25˚C and 200˚C illustrate the complex stress-strain response of AE44-2 and AE44-4 alloys. (ii) the relationship between the grain size and the strain hardening exponent (n) was studied and found that the grain size has a negative correlation with the strain hardening exponent at 25˚C and 200˚C.

6.2 Future work

The relationship between the microstructure and the mechanical properties of AE44-2 and AE44-4 alloys was studied in this study, and the conclusions have been shown above. However, more works need to be done in the future.

(1) The Vickers hardness tests need to be performed on the pyramidal castings. Because the pyramidal castings have a wide range of grain sizes, this will benefit studying the grain size effect on hardness.

(2) The cooling rate of the castings should be monitored at various locations to study the relationship between the cooling rate and the grain size and improve the accuracy of equation 5.2.2.

(3) Although the analytical approach can convert the load-depth curves to stress-strain curves, there is still some error in this approach. The critical point is to improve the accuracy of the value of the strain hardening exponent.

(4) The stress-strain response of AE44-2 and AE44-4 suggests that there might be some complex deformation mechanism existing in these alloys, especially at elevated temperature. In order to study the possible mechanism more researches are need. For example, the TEM (transmission electron microscope) should be used to study the twinning structure in the specimens before and after the indentation tests.

(5) In this study, the method of measuring the grain size within the indentations causes some error and needs to be improved. In the future, these indentations would be studied using SEM and measure the grain size in the indentations by the SEM images to reduce the error.

(6) The creep tests at various temperatures need to be performed on AE44-2 and AE44-4 specimens to study their creep behavior and calculate the activation energy of creep to compare their creep resistance.

Reference

[1] F. Pan, M. Yang, and X. Chen, “A Review on Casting Magnesium Alloys: Modification of Commercial Alloys and Development of New Alloys,” *J. Mater. Sci. Technol.*, vol. 32, no. 12, pp. 1211–1221, Dec. 2016, doi: 10.1016/j.jmst.2016.07.001.

[2] A. Luo and M. Pekguleryuz, “Cast magnesium alloys for elevated temperature applications,” *J. Mater. Sci.*, vol. 29, no. 20, pp. 5259–5271, 1994, doi: 10.1007/BF01171534.

[3] M. Regev, E. Aghion, and A. Rosen, “creep studies of AZ91D pressure die casting,” *Mater. Sci. Eng. A*, pp. 123–126, 1997.

[4] M. M. Avedesian, H. Baker, and ASM International. Handbook Committee, *Magnesium and magnesium alloys*. Materials Park, OH: ASM International, 1999.

[5] B. L. Mordike and T. Ebert, “Magnesium Properties — applications — potential,” *Mater. Sci. Eng. A*, p. 9, 2001.

[6] K. U. Kainer and Deutsche Gesellschaft für Materialkunde, *Magnesium alloys and technology*. Weinheim: DGM, 2003.

[7] M. Mezbahul-Islam, A. O. Mostafa, and M. Medraj, “Essential Magnesium Alloys Binary Phase Diagrams and Their Thermochemical Data,” *J. Mater.*, vol. 2014, pp. 1–33, Apr. 2014, doi: 10.1155/2014/704283.

[8] K. N. Braszczyńska-Malik, “Discontinuous and continuous precipitation in magnesium–aluminium type alloys,” *J. Alloys Compd.*, vol. 477, no. 1–2, pp. 870–876, May 2009, doi: 10.1016/j.jallcom.2008.11.008.

[9] K. Habib, K. Al-Muhanna, F. Al-Sabti, and A. Al-Arbeed, “Measurement of Oxide Barrier-Film Thickness of Al-Alloy by Electrochemical Impedance Spectroscopy at the

Nanometre-Scale," *Defect Diffus. Forum*, vol. 268, pp. 1–13, Nov. 2007, doi: 10.4028/www.scientific.net/DDF.268.1.

[10] C. R. Hutchinson, J. F. Nie, and S. Gorsse, "Modeling the precipitation processes and strengthening mechanisms in a Mg-Al-(Zn) AZ91 alloy," *Metall. Mater. Trans. A*, vol. 36, no. 8, pp. 2093–2105, Aug. 2005, doi: 10.1007/s11661-005-0330-x.

[11] C. H. Cáceres and D. M. Rovera, "Solid solution strengthening in concentrated Mg–Al alloys," *J. Light Met.*, vol. 1, no. 3, pp. 151–156, Aug. 2001, doi: 10.1016/S1471-5317(01)00008-6.

[12] A. Akhtar and E. Teghtsoonian, "Solid solution strengthening of magnesium single crystals—ii the effect of solute on the ease of prismatic slip," *Acta Metall.*, vol. 17, no. 11, pp. 1351–1356, Nov. 1969, doi: 10.1016/0001-6160(69)90152-7.

[13] M. Bamberger and G. Dehm, "Trends in the Development of New Mg Alloys," *Annu. Rev. Mater. Res.*, vol. 38, no. 1, pp. 505–533, Aug. 2008, doi: 10.1146/annurev.matsci.020408.133717.

[14] L. Han, H. Hu, D. O. Northwood, and N. Li, "Microstructure and nano-scale mechanical behavior of Mg–Al and Mg–Al–Ca alloys," *Mater. Sci. Eng. A*, vol. 473, no. 1–2, pp. 16–27, Jan. 2008, doi: 10.1016/j.msea.2007.03.053.

[15] J. P. Weiler, "Structure-property relationships for die-cast magnesium alloy AM60B.," Faculty of Graduate Studies, University of Western Ontario, London, Ont, 2005.

[16] P. Sharifi, "Process-Structure-Property relationships for High Pressure Die-cast Magnesium Alloys," p. 221.

[17] M. A. Easton *et al.*, "Evaluation of Magnesium Die-Casting Alloys for Elevated Temperature Applications: Castability: Evaluation of Magnesium Die-Casting Alloys…,"

Adv. Eng. Mater., vol. 18, no. 6, pp. 953–962, Jun. 2016, doi: 10.1002/adem.201500407.

[18] A. A. Luo, “Recent magnesium alloy development for elevated temperature applications,” *Int. Mater. Rev.*, vol. 49, no. 1, pp. 13–30, Feb. 2004, doi: 10.1179/095066004225010497.

[19] I. P. Moreno, T. K. Nandy, J. W. Jones, J. E. Allison, and T. M. Pollock, “Microstructural stability and creep of rare-earth containing magnesium alloys,” *Scr. Mater.*, vol. 48, no. 8, pp. 1029–1034, Apr. 2003, doi: 10.1016/S1359-6462(02)00595-X.

[20] S. G. Lee, G. R. Patel, A. M. Gokhale, A. Sreeranganathan, and M. F. Horstemeyer, “Quantitative fractographic analysis of variability in the tensile ductility of high-pressure die-cast AE44 Mg-alloy,” *Mater. Sci. Eng. A*, vol. 427, no. 1–2, pp. 255–262, Jul. 2006, doi: 10.1016/j.msea.2006.04.108.

[21] T. Rzychoń, A. Kiełbus, J. Cwajna, and J. Mizera, “Microstructural stability and creep properties of die casting Mg–4Al–4RE magnesium alloy,” *Mater. Charact.*, vol. 60, no. 10, pp. 1107–1113, Oct. 2009, doi: 10.1016/j.matchar.2009.05.014.

[22] A. A. Luo, “Recent magnesium alloy development for elevated temperature applications,” *Int. Mater. Rev.*, vol. 49, no. 1, pp. 13–30, Feb. 2004, doi: 10.1179/095066004225010497.

[23] C. Suman, “Creep of Diecast Magnesium Alloys AZ91D and AM60B,” Feb. 1991, p. 910416, doi: 10.4271/910416.

[24] S. R. Agnew, K. C. Liu, E. A. Kenik, and S. Viswanathan, “Tensile and Compressive Creep Behavior of Die Cast Magnesium Alloy AM60B,” in *Magnesium Technology 2000*, John Wiley & Sons, Ltd, 2013, pp. 285–290.

[25] K. Meshinchi Asl, A. Tari, and F. Khomamizadeh, “The effect of different content of Al, RE and Si element on the microstructure, mechanical and creep properties of Mg–Al

alloys," *Mater. Sci. Eng. A*, vol. 523, no. 1–2, pp. 1–6, Oct. 2009, doi: 10.1016/j.msea.2009.06.048.

[26] P. Shahbeigi Roodposhti, A. Sarkar, K. L. Murty, and R. O. Scattergood, "Effects of Microstructure and Processing Methods on Creep Behavior of AZ91 Magnesium Alloy," *J. Mater. Eng. Perform.*, vol. 25, no. 9, pp. 3697–3709, Sep. 2016, doi: 10.1007/s11665-016-2222-1.

[27] Z. Yang, J. Li, J. Zhang, G. Lorimer, and J. Robson, "Review on Research and Development of Magnesium Alloys," *Acta Metall. Sin. Engl. Lett.*, vol. 21, no. 5, pp. 313–328, Oct. 2008, doi: 10.1016/S1006-7191(08)60054-X.

[28] M. Zubair *et al.*, "On the role of Laves phases on the mechanical properties of Mg-Al-Ca alloys," *Mater. Sci. Eng. A*, vol. 756, pp. 272–283, May 2019, doi: 10.1016/j.msea.2019.04.048.

[29] A. A. Luo, B. R. Powell, and M. P. Balogh, "Creep and microstructure of magnesium-aluminum-calcium based alloys," *Metall. Mater. Trans. A*, vol. 33, no. 3, pp. 567–574, Mar. 2002, doi: 10.1007/s11661-002-0118-1.

[30] K. U. Kainer, Ed., "Front Matter," in *Magnesium Alloys and their Applications*, Weinheim, FRG: Wiley-VCH Verlag GmbH & Co. KGaA, 2006, p. I–XVIII.

[31] J. Zhang, S. Liu, Z. Leng, M. Zhang, J. Meng, and R. Wu, "Microstructures and mechanical properties of heat-resistant HPDC Mg–4Al-based alloys containing cheap misch metal," *Mater. Sci. Eng. A*, vol. 528, no. 6, pp. 2670–2677, Mar. 2011, doi: 10.1016/j.msea.2010.12.031.

[32] G. Pettersen, H. Westengen, R. Høier, and O. Lohne, "Microstructure of a pressure die cast magnesium—4wt.% aluminium alloy modified with rare earth additions," *Mater. Sci. Eng. A*, vol. 207, no. 1, pp. 115–120, Mar. 1996, doi: 10.1016/0921-5093(95)10035-

0.

[33] B. R. Powell, V. Rezhets, M. P. Balogh, and R. A. Waldo, “Microstructure and creep behavior in AE42 magnesium die-casting alloy,” *JOM*, vol. 54, no. 8, pp. 34–38, Aug. 2002, doi: 10.1007/BF02711864.

[34] M. J. Nayyeri and K. Dehghani, “Microstructure Evolution in As-Cast and SIMA-Processed AE42 Magnesium Alloy,” *J. Mater. Eng. Perform.*, vol. 23, no. 9, pp. 3077–3084, Sep. 2014, doi: 10.1007/s11665-014-1080-y.

[35] I. P. Moreno, T. K. Nandy, J. W. Jones, J. E. Allison, and T. M. Pollock, “Microstructural stability and creep of rare-earth containing magnesium alloys,” *Scr. Mater.*, vol. 48, no. 8, pp. 1029–1034, Apr. 2003, doi: 10.1016/S1359-6462(02)00595-X.

[36] S. Zhu *et al.*, “Evaluation of Magnesium Die-Casting Alloys for Elevated Temperature Applications: Microstructure, Tensile Properties, and Creep Resistance,” *Metall. Mater. Trans. A*, vol. 46, no. 8, pp. 3543–3554, Aug. 2015, doi: 10.1007/s11661-015-2946-9.

[37] E. G. Sieracki, J. J. Velazquez, and K. Kabiri, “Compressive Stress Retention Characteristics of High Pressure Die Casting Magnesium Alloys,” Feb. 1996, p. 960421, doi: 10.4271/960421.

[38] L. Y. Wei, G. L. Dunlop, and H. Westengen, “Development of microstructure in cast Mg-Al-rare earth alloys,” *Mater. Sci. Technol.*, vol. 12, no. 9, pp. 741–750, 1996, doi: 10.1179/mst.1996.12.9.741.

[39] S. M. Zhu, M. A. Gibson, J. F. Nie, M. A. Easton, and T. B. Abbott, “Microstructural analysis of the creep resistance of die-cast Mg–4Al–2RE alloy,” *Scr. Mater.*, vol. 58, no. 6, pp. 477–480, Mar. 2008, doi: 10.1016/j.scriptamat.2007.10.041.

[40] S. Zhu *et al.*, “Evaluation of Magnesium Die-Casting Alloys for Elevated

Temperature Applications: Microstructure, Tensile Properties, and Creep Resistance," *Metall. Mater. Trans. A*, vol. 46, no. 8, pp. 3543–3554, Aug. 2015, doi: 10.1007/s11661-015-2946-9.

[41] T. Rzychoń, A. Kiełbus, J. Cwajna, and J. Mizera, "Microstructural stability and creep properties of die casting Mg–4Al–4RE magnesium alloy," *Mater. Charact.*, vol. 60, no. 10, pp. 1107–1113, Oct. 2009, doi: 10.1016/j.matchar.2009.05.014.

[42] S. M. Zhu, J. F. Nie, M. A. Gibson, M. A. Easton, and P. Bakke, "Microstructure and Creep Behavior of High-Pressure Die-Cast Magnesium Alloy AE44," *Metall. Mater. Trans. A*, vol. 43, no. 11, pp. 4137–4144, Nov. 2012, doi: 10.1007/s11661-012-1247-9.

[43] J. Zhang, P. Yu, Ke. Liu, D. Fang, D. Tang, and J. Meng, "Effect of substituting cerium-rich mischmetal with lanthanum on microstructure and mechanical properties of die-cast Mg–Al–RE alloys," *Mater. Des.*, vol. 30, no. 7, pp. 2372–2378, Aug. 2009, doi: 10.1016/j.matdes.2008.10.028.

[44] K. Y. Ko, S. Yoon, and J. G. Booth, "Magnetic properties and microstructure of hot-pressed and die-upset Mischmetal-FeB-(Al)permanent magnets," *J. Magn. Magn. Mater.*, vol. 176, no. 2, pp. 313–320, Dec. 1997, doi: 10.1016/S0304-8853(97)00652-5.

[45] J. Zhang, K. Liu, D. Fang, X. Qiu, D. Tang, and J. Meng, "Microstructure, tensile properties, and creep behavior of high-pressure die-cast Mg–4Al–4RE–0.4Mn (RE = La, Ce) alloys," *J. Mater. Sci.*, vol. 44, no. 8, pp. 2046–2054, Apr. 2009, doi: 10.1007/s10853-009-3283-4.

[46] J. Zhang *et al.*, "Microstructures, tensile properties and corrosion behavior of die-cast Mg–4Al-based alloys containing La and/or Ce," *Mater. Sci. Eng. A*, vol. 489, no. 1–2, pp. 113–119, Aug. 2008, doi: 10.1016/j.msea.2007.12.024.

[47] Q. Yang *et al.*, "Creep behavior of high-pressure die-cast Mg-4Al-4La-0.4Mn alloy

under medium stresses and at intermediate temperatures," *Mater. Sci. Eng. A*, vol. 650, pp. 190–196, Jan. 2016, doi: 10.1016/j.msea.2015.09.061.

[48] S. Zhu, M. A. Easton, T. B. Abbott, M. A. Gibson, and J.-F. Nie, "The Influence of Individual Rare Earth Elements (La, Ce, or Nd) on Creep Resistance of Die-Cast Magnesium Alloy AE44: Creep Resistance of Die-cast Magnesium Alloy AE44," *Adv. Eng. Mater.*, vol. 18, no. 6, pp. 932–937, Jun. 2016, doi: 10.1002/adem.201500545.

[49] J. Zhang, M. Zhang, J. Meng, R. Wu, and D. Tang, "Microstructures and mechanical properties of heat-resistant high-pressure die-cast Mg–4Al–xLa–0.3Mn (x=1, 2, 4, 6) alloys," *Mater. Sci. Eng. A*, vol. 527, no. 10, pp. 2527–2537, Apr. 2010, doi: 10.1016/j.msea.2009.12.048.

[50] T. Rzychoñ and A. Kie, "The influence of wall thickness on the microstructure of HPDC AE44 alloy," p. 5.

[51] E. O. Hall, "The Deformation and Ageing of Mild Steel: III Discussion of Results," *Proc. Phys. Soc. Sect. B*, vol. 64, no. 9, pp. 747–753, Sep. 1951, doi: 10.1088/0370-1301/64/9/303.

[52] N. J. Petch, "The cleavage strength of polycrystals," *J. Iron Steel Inst.*, vol. 174, pp. 25–28, 1953.

[53] C. J. Bettles, M. A. Gibson, and S. M. Zhu, "Microstructure and mechanical behaviour of an elevated temperature Mg-rare earth based alloy," *Mater. Sci. Eng. A*, vol. 505, no. 1–2, pp. 6–12, Apr. 2009, doi: 10.1016/j.msea.2008.11.004.

[54] G. E. Dieter, *Mechanical metallurgy*, 3rd ed. New York ; McGraw-Hill, 1986.

[55] A. A. Luo, B. R. Powell, and M. P. Balogh, "Creep and microstructure of magnesium-aluminum-calcium based alloys," *Metall. Mater. Trans. A*, vol. 33, no. 3, pp. 567–574, Mar. 2002, doi: 10.1007/s11661-002-0118-1.

[56] J. Pelleg, *Creep in Ceramics*, vol. 241. Cham: Springer International Publishing, 2017.

[57] R. Hill, B. Storåkers, and A. B. Zdunek, “A theoretical study of the Brinell hardness test,” *Proc. R. Soc. Lond. Math. Phys. Sci.*, vol. 423, no. 1865, pp. 301–330, Jun. 1989, doi: 10.1098/rspa.1989.0056.

[58] H. A. Francis, “Phenomenological Analysis of Plastic Spherical Indentation,” *J. Eng. Mater. Technol.*, vol. 98, no. 3, pp. 272–281, Jul. 1976, doi: 10.1115/1.3443378.

[59] S. Pathak and S. R. Kalidindi, “Spherical nanoindentation stress–strain curves,” *Mater. Sci. Eng. R Rep.*, vol. 91, pp. 1–36, May 2015, doi: 10.1016/j.mser.2015.02.001.

[60] W. C. Oliver and G. M. Pharr, “An improved technique for determining hardness and elastic modulus using load and displacement sensing indentation experiments,” *J. Mater. Res.*, vol. 7, no. 6, pp. 1564–1583, Jun. 1992, doi: 10.1557/JMR.1992.1564.

[61] D. Tabor, *The hardness of metals*. Oxford: Clarendon Press, 1951.

[62] E. G. Herbert, G. M. Pharr, W. C. Oliver, B. N. Lucas, and J. L. Hay, “On the measurement of stress–strain curves by spherical indentation,” *Thin Solid Films*, p. 5, 2001.

[63] J. R. Matthews, “Indentation hardness and hot pressing,” *Acta Metall.*, vol. 28, no. 3, pp. 311–318, Mar. 1980, doi: 10.1016/0001-6160(80)90166-2.

[64] B. Xu and X. Chen, “Determining engineering stress–strain curve directly from the load–depth curve of spherical indentation test,” *J. Mater. Res.*, vol. 25, no. 12, pp. 2297–2307, Dec. 2010, doi: 10.1557/jmr.2010.0310.

[65] Y. Tirupataiah and G. Sundararajan, “On the constraint factor associated with the indentation of work-hardening materials with a spherical ball,” *Metall. Trans. A*, vol. 22,

no. 10, pp. 2375–2384, Oct. 1991, doi: 10.1007/BF02665003.

[66] F. Pöhl, “Pop-in behavior and elastic-to-plastic transition of polycrystalline pure iron during sharp nanoindentation,” *Sci. Rep.*, vol. 9, no. 1, p. 15350, Dec. 2019, doi: 10.1038/s41598-019-51644-5.

[67] E. O. Hall, “Variation of Hardness of Metals with Grain Size,” *Nature*, vol. 173, no. 4411, Art. no. 4411, May 1954, doi: 10.1038/173948b0.

[68] Y. Y. Lim and M. M. Chaudhri, “The influence of grain size on the indentation hardness of high-purity copper and aluminium,” *Philos. Mag. A*, vol. 82, no. 10, pp. 2071–2080, Jul. 2002, doi: 10.1080/01418610208235717.

[69] M. A. Easton and D. H. StJohn, “Improved prediction of the grain size of aluminum alloys that includes the effect of cooling rate,” *Mater. Sci. Eng. A*, vol. 486, no. 1–2, pp. 8–13, Jul. 2008, doi: 10.1016/j.msea.2007.11.009.

[70] M. Sun, “Effect of Cooling Rate on the Grain Refinement of Mg-Y-Zr Alloys,” *Metall. Mater. Trans. A*, p. 15.

[71] Y. C. Lee, A. K. Dahle, and D. H. StJohn, “The role of solute in grain refinement of magnesium,” *Metall. Mater. Trans. A*, vol. 31, no. 11, pp. 2895–2906, Nov. 2000, doi: 10.1007/BF02830349.

[72] D. H. StJohn, M. Qian, M. A. Easton, P. Cao, and Z. Hildebrand, “Grain refinement of magnesium alloys,” *Metall. Mater. Trans. A*, vol. 36, no. 7, pp. 1669–1679, Jul. 2005, doi: 10.1007/s11661-005-0030-6.

[73] C. H. Cáceres, P. Lukáč, and A. Blake, “Strain hardening due to {10 1 2} twinning in pure magnesium,” *Philos. Mag.*, vol. 88, no. 7, pp. 991–1003, Mar. 2008, doi: 10.1080/14786430701881211.

[74]H. J. Frost, *Deformation-mechanism maps: the plasticity and creep of metals and ceramics*, 1st ed. Oxford [Oxfordshire] ; Pergamon Press, 1982.

Appendices

Appendix A: computed phase diagrams for the AE44-2 and AE44-4 alloys

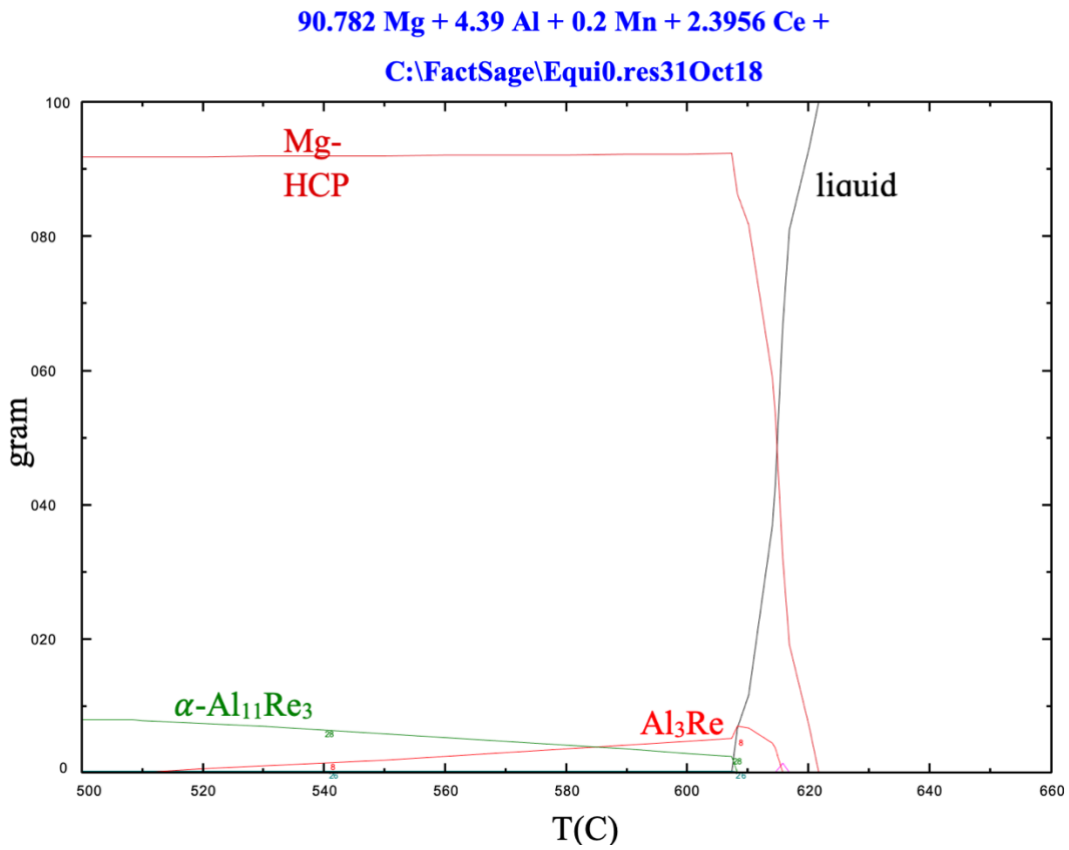

Equilibrium cooling of AE44-4

Comments:

- Trace elements (Zn, Si, Cu, Fe, Ni, Be) are not considered in this calculation due to their very small concentration. They are assumed to either be in the solid solution such as Cu or as pure impurity such as Fe.
- At room temperature, out of 100g sample, I expect to form 92g (Mg) solid solution and around 8g of α-$Al_{11}Re_3$ (Re= Ce, La, Nd, Pr)
- Solidification terminates at around 607°C
- Al3Re is the first solid to form the liquid but it decomposes upon cooling.

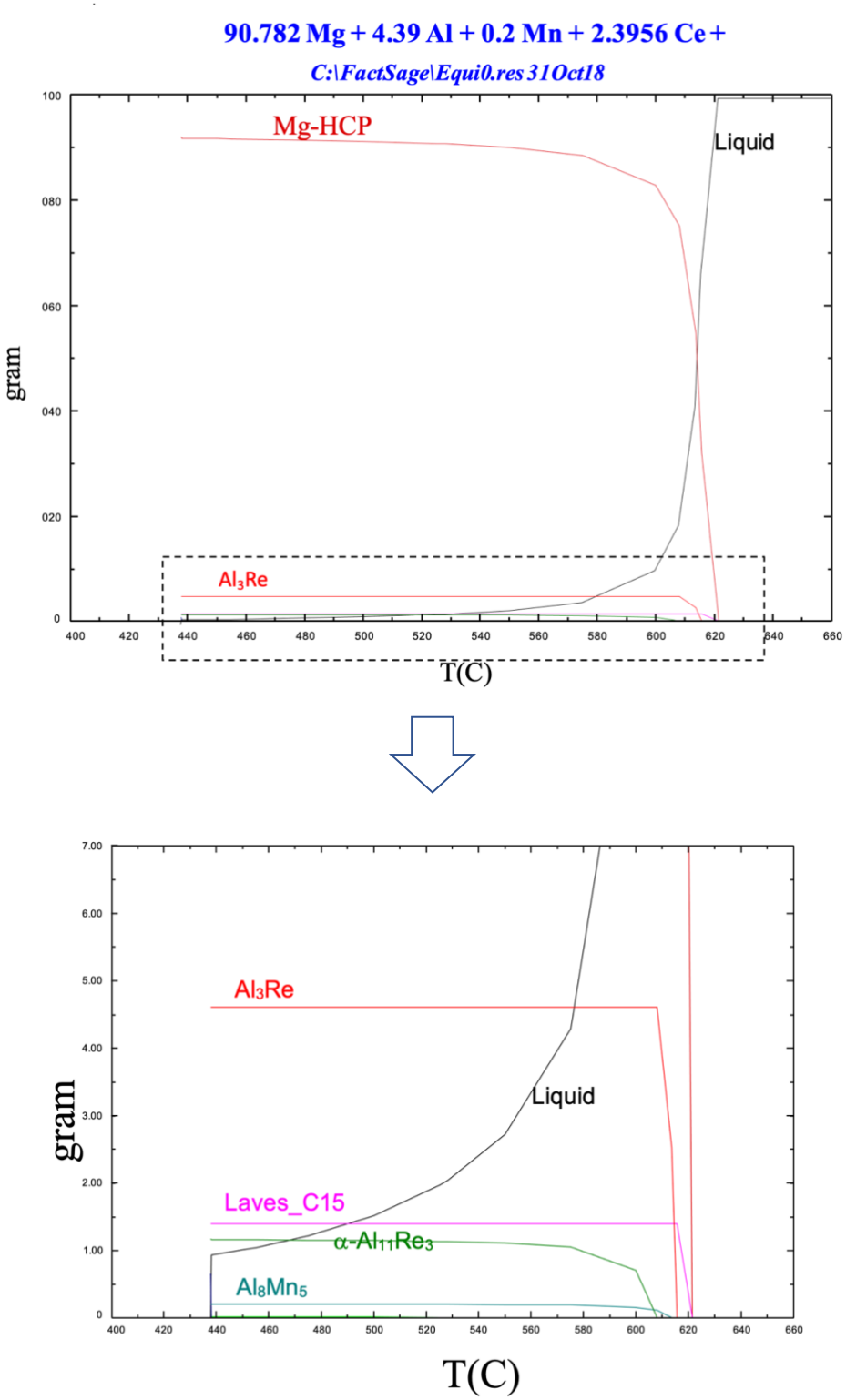

Scheil Cooling of AE44-4 – simulates very fast cooling close to what happens during die casting

Comments:

- In fast cooling, solidification terminates at lower temperature but Scheil simulation underestimates the final solidification point therefore calculations are terminated at 1wt% liquid. Even, we sometimes terminate at 2wt%
- More precipitates than slow cooling.
- Around 5g Al3Re, 1.5g Laves_C15, 1.2g α-$Al_{11}Re_3$, and 0.2g Al_8Mn_5
- Around 90g Mg solid solution is expected at room temperature; the rest is the above solid solution precipitates.

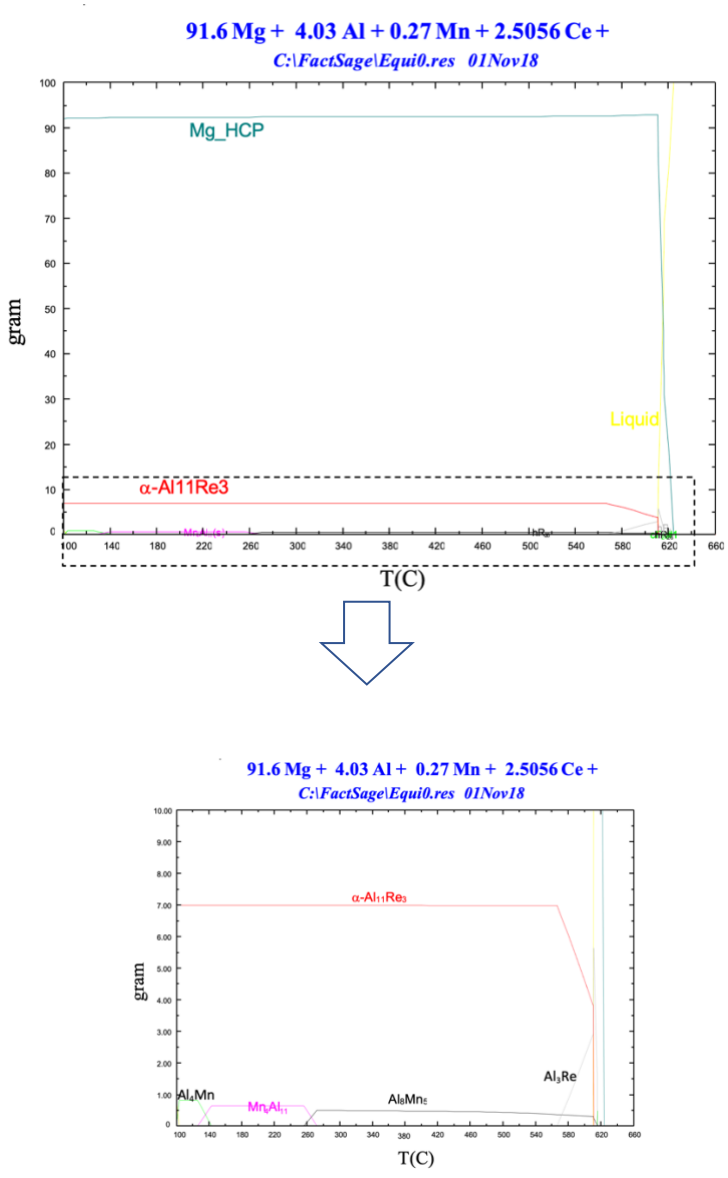

Equilibrium cooling of AE44-2

Comments:

- Unlike AE44-4, Al_3Re decomposes and Al-Mn intermetallic form at different temperature ranges to finally end with around 1g of Al_4Mn.

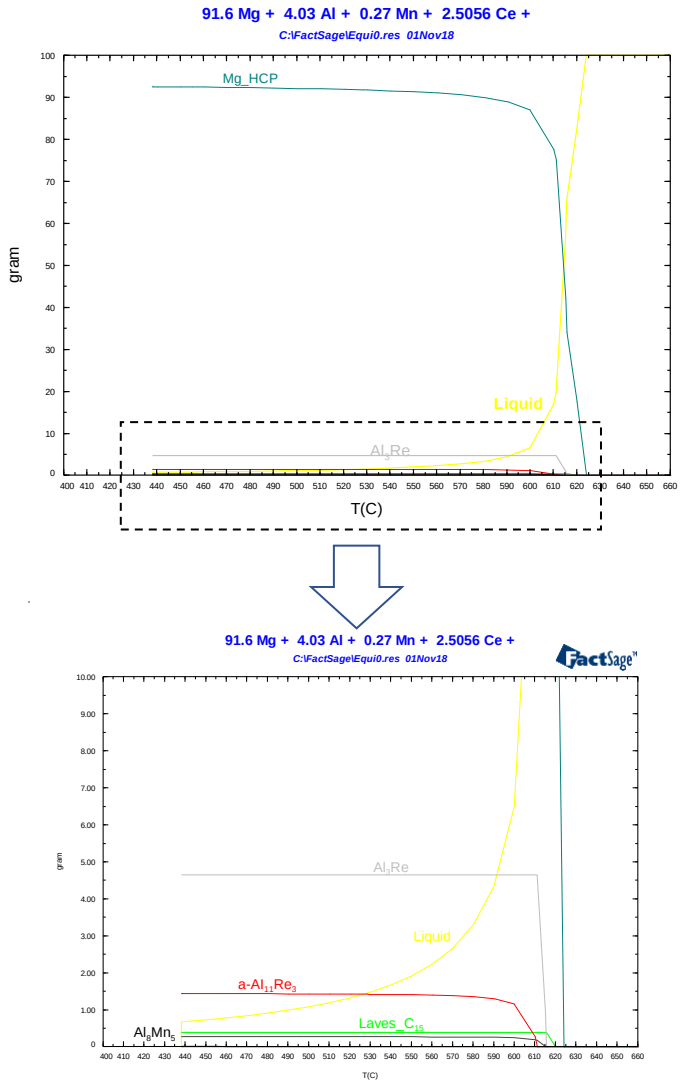

Scheil Cooling of AE44-2

Comment:

- Similar precipitate types to AE44-4 but different amounts.

Curriculum Vitae

Name:	Bolin Fu
Post-secondary Education and Degrees:	Hefei University of Technology Hefei, Anhui Province, China Bachelor of Engineering (2013-2017)
Honors and Awards:	Outstanding Graduate First-, second-, Third- class Scholarship Merit Student
Related Work Experience	Teaching Assistant University of Western Ontario (2019-2020)